Advances in near-field electron ptychography

By:

Shengbo You

Supervised By:

Dr Andrew Maiden, Prof John Rodenburg

and Dr Thomas Walther

A thesis submitted in partial fulfilment of the requirements for the degree of Doctor of Philosophy

The University of Sheffield

Faculty of Engineering

Department of Electronic and Electrical Engineering

21 September, 2023

Abstract

Over the past few years, ptychography has drawn considerable attention for its ability to recover high contrast and ultra-high resolution images without the need for high quality optics. In its conventional form, it is a type of scanned-probe microscopy, in which a convergent beam – the ptychographic probe – illuminates a small patch of a sample, and then scans through a grid of positions to cover a region of interest, recording diffraction patterns at each point in the grid. Near-field ptychography, originally proposed as a tool to image a larger field of view, was first demonstrated with X-ray and quickly extended to visible light and electron microscopy. In X-ray and visible light community, the near-field ptychography was well explored and combined with multislice and tomography to image three-dimensional samples.

Previously, near-field electron ptychography has been proved to be able to image a much larger field of view with fewer diffraction patterns. This thesis keeps exploring the performance of the near-field ptychography with electron microscopy. Our novel design of the amplitude diffuser together with the new experimental arrangement make better use of electron dose and reduce inelastic scattering. The variable magnifications are possible in this geometry, via appropriate adjustment of condenser and projection lens settings. Next, our setup is extended to image the magnetic sample in Lorentz TEM mode. Finally, we make the first attempt at achieving atomic resolution and imaging biological specimens under low voltage conditions using this technique.

Acknowledgements

I would like to express my gratitude to those people who have supported me throughout my academic studies.

I would like to express my thanks to my Prof. John Rodenburg. He has led me into the field of ptychography and supervised me with great patience. He has provided me with the opportunity to fulfil a long-held dream of mine to pursue my PhD study. I have enjoyed all of our conversions, in the office and in the pub.

I would also like to express my thanks to Dr Andrew Maiden. After John retired, he has given me tremendous help to finish my PhD study. He has entrusted me with the near-field electron ptychography and given me the opportunity to explore this exciting field.

I would like to thank my second supervisor, Dr Thomas Walther, for his kindness and understanding during the difficult time of my study.

I would also like to thank all of my collaborators, especially Penghan Lu and Prof. Rafal E. Dunin-Borkowski. They have been very supportive with the experiments and I have learned a lot from them.

I have met many excellent colleagues and friends in the offices, Dr Freddick Allars, Dr Yangyang Mu, Dr Zhuoqun Zhang, Dr Yiqian Zhang, Wenjie Mei, and Ziyang Hu as they have been very supportive throughout my PhD study.

Finally, I would like to thank my parents, Fengjun Wang and Hongtu You, who have always supported my academic endeavours. I am standing on their shoulders to see the world.

Table of Contents

List of acronyms

AEM Analytical Electron Microscopy

CFE Cold Field Emission

EDX Energy Dispersive X-ray spectroscopy

EELS Electron Energy Loss Spectroscopy

ePIE Extended Ptychographical Iterative Engine

FEG Field Emission Gun

TEM Transmission Electron Microscopy

MIP Mean Inner Potential

NA Numerical Aperture

PIE Ptychographical Iterative Engine

SAA Selective Area Aperture

SNR Signal-to-Noise Ratio

STEM Scanning Transmission Electron Microscopy

XED X-ray Energy-Dispersive Spectroscopy

List of Publications

Part of the work published in this thesis were previously presented as posters at conferences:

1. Shengbo You, 'Depth Resolution in Ptychography', *Microscience Microscopy Congress 2021* (July 2021), Virtual Conference.
2. Shengbo You, Penghan Lu, Thomas Schachinger, Andras Kovacs, Rafal E. Dunin-Borkowski, Andrew M. Maiden, 'Magnetic Phase imaging using Lorentz Near-field Electron Ptychography', *Microscopy Conference 2023* (February 2023), Darmstadt, Germany.
3. Shengbo You, Penghan Lu, Thomas Schachinger, Andras Kovacs, Rafal E. Dunin-Borkowski, Andrew M. Maiden, 'Magnetic Phase imaging using Lorentz Near-field Electron Ptychography', *RMS Microscopy of Semi-Conducting Materials 2023* (April 2023), Cambridge, UK.

Part of the work published in this thesis were previously presented as presentation at conferences:

1. Shengbo You, Penghan Lu, Thomas Schachinger, Andras Kovacs, Rafal E. Dunin-Borkowski, Andrew M. Maiden, 'Magnetic Phase imaging using Lorentz Near-field Electron Ptychography', *International Symposium on Computational Sensing 2023* (June 2023), Luxembourg, Luxembourg.
2. Shengbo You, Penghan Lu, Thomas Schachinger, Andras Kovacs, Rafal E. Dunin-Borkowski, Andrew M. Maiden, 'Magnetic Phase imaging using Lorentz Near-field Electron Ptychography', *Microscience Microscopy Congress 2023* (July 2023), Manchester, Manchester.

Part of the work published in this thesis are under review as the journal paper publication:

1. Shengbo You, Penghan Lu, Thomas Schachinger, Andras Kovacs, Rafal E. Dunin-Borkowski, Andrew M. Maiden, 'Magnetic Phase imaging using Lorentz Near-field Electron Ptychography', Applied Physics letter.

Chapter 1. Motivation

The attempt to image microscopic structures with smaller sizes has never stopped. Electrons, with the smallest wavelength among all the illumination sources, are considered as the front line. The modern Transmission Electron Microscope (TEM) with the aberration corrector has pushed the resolution well below 0.1 nm (Carter 2009). However, not all the materials can be directly imaged using the TEM. Many objects do not significantly absorb or scatter the electrons. These objects appear low image contrast or even transparent under TEM, such as cells in most biological materials.

One solution is to solve the phase problem. Since the detector in the TEM only records the intensity of the electron beam, the phase information is lost. Those objects with low contrast in the modulus map can be clearly imaged in the phase map. One of the most well-known methods to recover the phase information using TEM is called Lorentz Microscopy. This technique uses the classical Lorentz interaction between the magnetic field arising from the magnetic components of the specimen, and the electron beam that are perpendicular to it. The Lorentz interaction results in the deflection of electron beam direction, and the magnetic domain, together with the phase information can be recovered by quantitative analysis the deflected electrons using computational methods, such as electron holography. In Scanning Transmission Electron Microscopy (STEM), one method to solve the phase is called

Differential Phase Contrast (DPC). It measures the deflection of the electron beam caused by the field at each scan point. Then it maps the local electromagnetic field by using the computational method such as centre of mass.

Ptychography is another computational imaging method that can solve the phase problem. In its conventional form, it is a type of scanned-probe microscopy (Hoppe 1982, Bates and Rodenburg 1989, Pennycook, Lupini et al. 2015) in which a convergent electron beam – the ptychographic probe – illuminates a small patch of a sample, and then scans through a grid of positions to cover a region of interest, recording diffraction patterns at each point in the grid (Rodenburg and Faulkner 2004). The diffraction patterns are processed using iterative optimisation algorithms to reconstruct a complex-valued transmission function of the sample, whilst simultaneously recovering the probe wavefront (Guizar-Sicairos, Thurman and Fienup 2008, Thibault, Dierolf et al. 2008, Maiden and Rodenburg 2009, Wen, Yang et al. 2012, Hesse, Luke et al. 2015). This simple experimental process combined with relatively robust reconstruction algorithms has led to ptychography's uptake across a range of wavelength regimes, from visible light (Rodenburg, Hurst and Cullis 2007), to X-rays (Rodenburg, Hurst et al. 2007, Thibault, Dierolf et al. 2008), and using different probes such as electrons (Hüe, Rodenburg et al. 2010, Hüe, Rodenburg et al. 2011, Putkunz, D'Alfonso et al. 2012, D'alfonso, Morgan et al. 2014, Yang, Ercius et al. 2016, Yang, Rutte et al. 2016, Gao, Wang et al. 2017, Yang, MacLaren et al. 2017)

However, due to the use of a nearly-focused probe and the requirement for significant overlap of the probe illuminated area, covering a large field of view using ptychography requires the collection of many diffraction patterns, often numbering in the tens of thousands, which is time-consuming both in terms of data collection and data processing. Near-field electron ptychography overcomes this limitation by replacing the focused-probe electron beam with a full-field structured illumination and repositioning the detector so that it records near-field (Fresnel) rather than far-field (Fraunhofer) diffraction patterns.

Near-field ptychography was first demonstrated with X-rays (Stockmar, Cloetens et al. 2013) but has since been extended to visible light (McDermott and Maiden 2018) and electron microscopy (Maiden-, Sarahan et al. 2015) . In the X-ray community, near-field ptychography successfully retrieved the complex transfer function of both the sample and the illumination probe (Clare, Stockmar et al. 2015). The effect of a diffuser was tested in the same experiment.

With the diffuser, a piece of paper in this case, to structure the illumination probe, the signal-to-noise ratio (SNR) was significantly improved. This provided valuable information for our experiments in Chapter 3. In 2015, the same team combined near-field ptychography with model decomposition and imaged a sample as thick as 46 μm, a thickness not accessible by inline holography (Stockmar, Zanette et al. 2015). This experiment showed the potential of near-field ptychography in imaging thick samples. In the same year, near-field ptychography was combined with tomography to image three-dimensional micro-structure (Stockmar, Hubert et al. 2015). This new technique produced results of similar quality to the results from holotomography (Cloetens, Peters, et al. 1999), a well-explored technique for imaging three-dimensional structures.

In the visible-light community, near-field ptychography was first implemented using a laser beam to illuminate the sample (McDermott and Maiden 2018). Similar to the x-ray near-field ptychography, a piece of transparent adhesive tape functioned as a diffuser to structure the illumination. In this paper, three samples were used to test the performance of near-field ptychography. The experiments with the frog's red cell sample as a sample demonstrated that the number of diffraction patterns can be 4 and still reproduce reliable results. The glass microspheres experiment showed the potential of near-field ptychography in imaging thick samples. The singlet lens experiment proved that near-field ptychography had accurate phase reconstruction with excellent spatial frequency response. Near-field ptychography was then combined with Fourier ptychography with speckle illumination and achieved a 7-fold resolution gain (Zhang, Jiang et al. 2019). A low-cost 3D printed add-on implementing a rotation, or arc, scan pattern instead of the conventional raster scan pattern was tested on near-field ptychography (Zhang, Zhang and Maiden 2022). Different biological samples, blood cells and termite soldier samples demonstrated that this simple translation stage was capable of accurate phase reconstruction while retaining the merit of using fewer diffraction patterns. Near-field ptychography was combined with multi-slice using both laser and x-ray (Hu, Zhang et al. 2023). This combination shows the capability of recovering high-resolution phase images over a large field of view using few diffraction patterns, as well as a good degree of depth sensitivity.

From the successful experiments of near-field ptychography with visible light and X-ray, the advantages of near-field ptychography can be summarized. It can accurately recover the

phase information over a large field of view with fewer diffraction patterns. With a diffuser to structure the illumination, the quality of the results, especially the SNR, can be significantly improved. Benefiting the large field of view in each diffraction pattern, near-field ptychography showed remarkable capability of imaging thick specimens.

In the first implementations of near-field electron ptychography (Maiden, Sarahan et al. 2015), the sample was illuminated by a broad, roughly parallel illumination beam, and the microscope's selected area aperture (SAA) was used to choose a region of interest from the resulting bright field image, as shown in Fig 1.1 (Maiden, Sarahan et al. 2015).

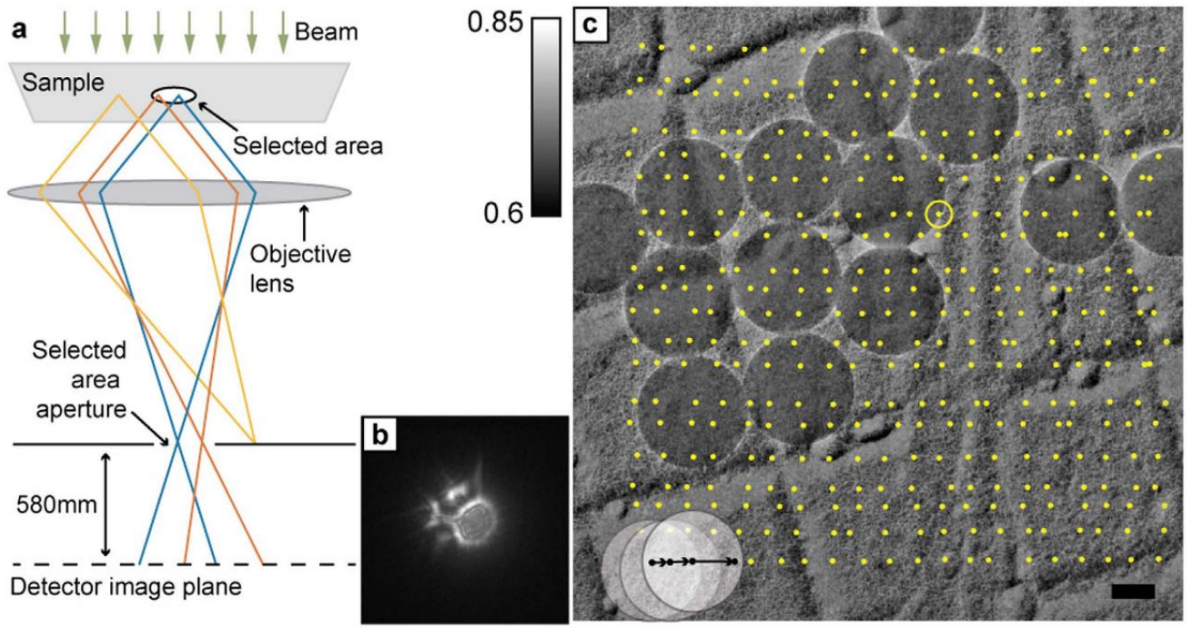

Fig 1.1. (a) is the experimental configuration of the first near-field electron ptychography. (b) is an example diffraction pattern. The sample was scanned in a raster fashion over the grid of 20 rows and 20 columns, indicated by the yellow dots in (c). The scale bar is 100 nm.

The SAA in this implementation acted like a virtual probe; it was as though the sample were illuminated by an electron beam shaped like the aperture, shrunk down by the magnification factor of the microscope objective lens. Before the near-field electron ptychography was proposed in this paper, imaging large field of view using TEM was mostly carried out by holography. Holography has the advantage of collecting the dataset using one exposure and a quick reconstruction algorithm to extract the phase image of the sample. However, it does require the electrostatic biprism mounted inside the TEM. And the preparation of the sample needs to be carefully proceeded so that it lies adjacent to a region of vacuum. Near-field

electron ptychography, on the other hand, does not require additional instrument accessory and is accessible by most of the TEM. And the region of vacuum is not required around the sample. By translating the specimen using a lateral shifting method, the total field of view of reconstructed area can be greatly extended. However, this design requires the Fresnel fringes from the edge of the SAA to structure the illumination. Hence, the field of view of each diffraction pattern is limited by the physical size of the SAA. To cover a large field of view hundreds of diffraction patterns are required.

This method was later improved by inserting an engineered phase plate (or diffuser) in the SAA (Allars, Lu et al. 2021) to better modulate the wavefront exiting the SAA, as shown in Fig 1.2 (Allars, Lu et al. 2021).

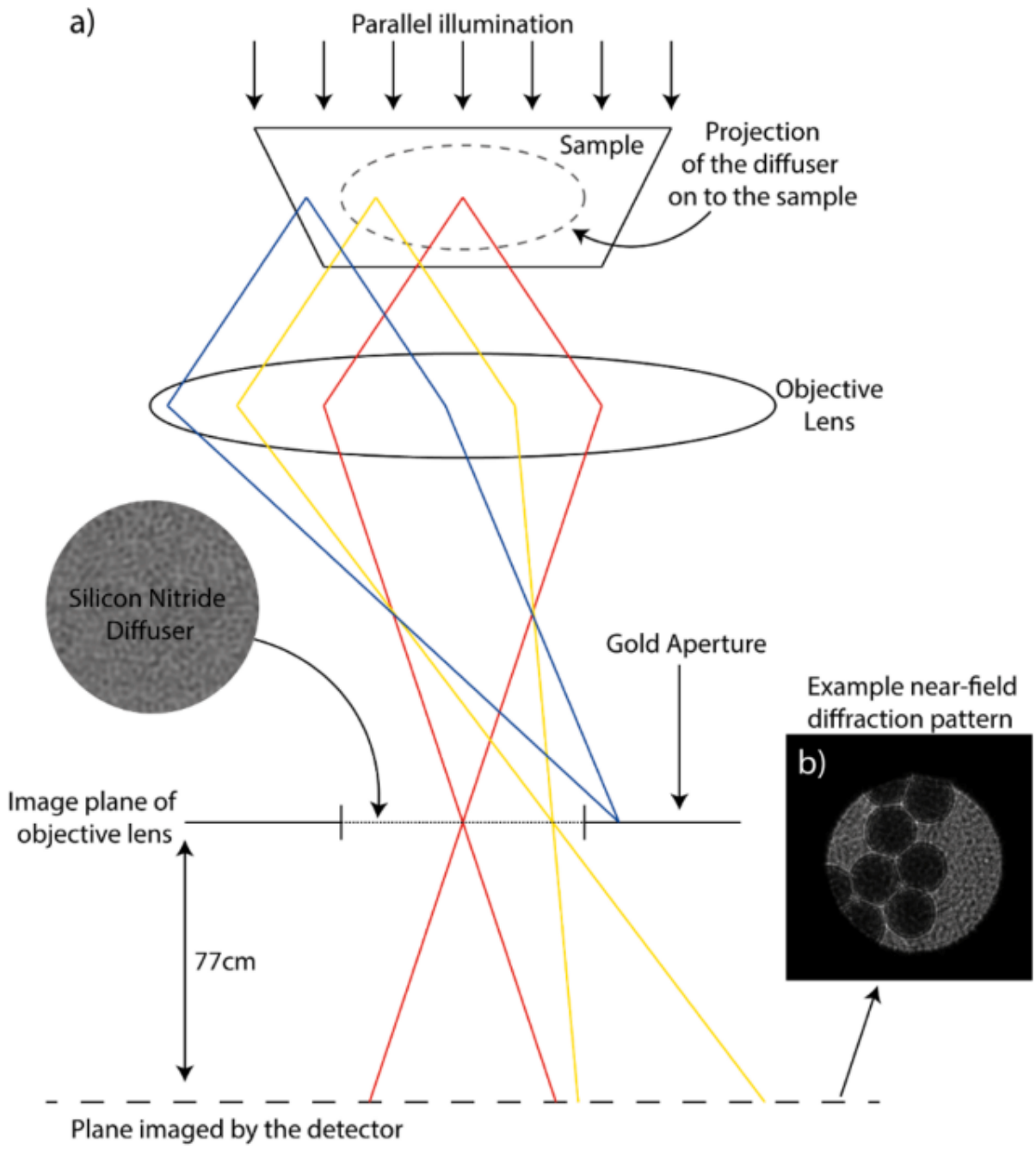

Fig 1.2. (a) is the experimental configuration of the second near-field electron ptychography. A Silicon Nitride phase diffuser is inserted at the SAA. (b) is an example diffraction pattern. The sample was scanned in a raster fashion similar to the one in Fig 1.1.

With the configuration in Fig 1.2, the phase diffuser as well as the aperture edge cause diffraction fringes in the recorded data, such that even very large apertures at shorter camera lengths produce data containing plenty of fringe structure, and each diffraction pattern can therefore cover a large field of view. Using this setup, megapixel phase images could be reconstructed from as few as nine diffraction patterns. With 1600 diffraction patterns, this

setup can recover the phase image of an area as large as 100μm², comparing to previous setup (Maiden, Sarahan et al. 2015) that using 400 diffraction patterns recovering an area of 2μm². However, the sample was constantly exposed to the electron beam, even in areas outside of the region masked by the SAA, and the phase plate introduced additional unwanted inelastic scatter, so this approach did not make optimal use of the dose, whilst changing the magnification of the setup to image at different resolutions involved changing the size of the SAA so that a full set of diffuser-equipped apertures were required for multi-scale imaging.

In visible light and X-ray experiments, the diffuser is usually a piece of transparent tape or paper. Both had the characteristic of adding structure to the phase of the illumination, while the effect on the modulus of the illumination was negligible. Inspired by this, an amplitude diffuser was designed and implemented. Such a diffuser was inserted at the condenser lens aperture so that the variable illumination sizes could be achieved by tuning the strength of the lenses. With this configuration, the electron beam only illuminates the region of interest, with the rest of the sample unexposed to the electrons, the electron dose efficiency is improved. This thesis explored the performance of this novel near-field ptychography design in conventional TEM mode, Lorentz mode, and limiting conditions.

This thesis is arranged as follows:

Chapter 2 explains the essential background knowledge, including electron propagation in free space and interaction with the sample, the working principle of the TEM, ptychography and the reconstruction algorithm.

Chapter 3 discusses the experimental condition of our near-field electron ptychography in the conventional TEM mode, the design of the amplitude diffuser, the workflow of the reconstruction process, the calculation of the parameters such as the defocus and magnification values, the results and analysis.

Chapter 4 presents the performance of near-field ptychography in the Lorentz mode. The initial experiment used the well-explored latex spheres as the sample. Then the magnetic sample was examined under the same experimental conditions. The challenge was to reproduce the scan positions. The problem and solution are discussed in detail.

Chapter 5 explores the limitations of near-field ptychography in the conventional TEM mode. The first attempt is to achieve the atomic resolution. The second attempt is to examine the biological sample, a slice of rat brain, under low acceleration voltage conditions.

Chapter 6 is the discussion and future work. Datasets that are not well-tuned is presented.

Chapter 2. Background

This chapter introduces the necessary background knowledge of electron microscopy. It is arranged as follows: the electron propagation in free space is discussed in subsection 2.1. The interaction between electron and object is introduced in subsection 2.2. The basics of Transmission Electron Microscopy (TEM), which is the most used electron microscopy in this thesis, is briefly discussed in subsection 2.3. The limitation of TEM is discussed in subsection 2.4. The computation imaging techniques that is used to retrieve the phase information from the TEM diffraction patterns, is discussed in 2.5 (holography) and 2.6 (ptychography).

2.1 Electron propagation in free space.

This section discussed different representations of electron propagation in free space.

2.1.1 Electron wave equation

Electrons show both wave and particle characteristics. Based on de Broglie's ideas of the wave-particle duality, one can relate the particle momentum p to its wavelength λ, using Plank's constant,

$$\lambda = \frac{h}{p} \tag{2.1}$$

When used in TEM, the electrons are accelerated through a voltage V, so that the electrons gain a kinetic energy eV. If the electrons are accelerated from rest, the kinetic energy is equal to

$$eV = \frac{m_0 v^2}{2} \tag{2.2}$$

where e is the electron charge, m_0 is the rest mass of the electron, and v is the electron velocity. The momentum p can also be represented as

$$p = m_0 v = \sqrt{2m_0 eV} \tag{2.3}$$

substitute the momentum into previous equations,

$$\lambda = \frac{h}{\sqrt{2m_0 eV}} \tag{2.4}$$

The inverse relationship between the wavelength and the accelerating voltage indicates that if the accelerating voltage increases, the wavelength decreases. However, the above equation is the non-relativistic electron wavelength. In other words, if the speed of the electrons is no longer significantly slow comparing to the speed of the light (typically when the speed of electron is greater than half of the speed of light, corresponding accelerating voltage > ~100keV), the relativistic effects should be considered, then the equation of the wavelength should be:

$$\lambda = \frac{h}{\sqrt{2m_0 eV\left(1+\frac{eV}{2m_0 c^2}\right)}} \tag{2.5}$$

2.1.2 Huygens-Fresnel principle

One of the most fundamental and easily-understood concepts in wave propagation is the Huygens-Fresnel principle. It states that every point on a wavefront is a new source of spherical waves, and the secondary wavelets emanating from different points mutually interfere. The next wavefront is the superposition of all previous wavelets (Goodman 2005).

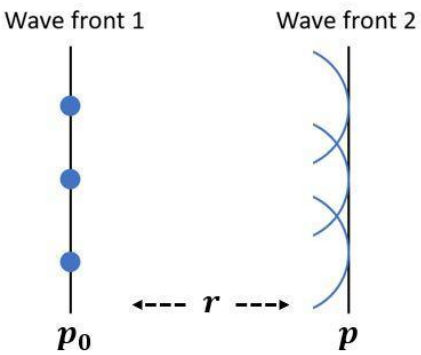

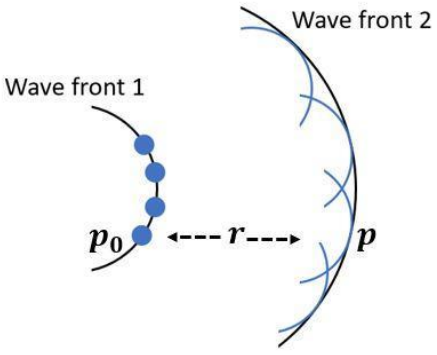

Figure 2.1. Explanation of the Huygens-Fresnel principle. Each point (blue point) on the first wavefront is a spherical wave source (blue circle). The left figure is the propagation of the plane wave, the right figure is the propagation of a spherical wave.

Consider a point source at p_0, having a complex amplitude u_0 and at distance r, another point p, then according to the Huygens-Fresnel principle, the magnitude at point p would be:

$$U(r) \propto \frac{u_0 e^{ikr}}{r} \tag{2.6}$$

where $k = \frac{2\pi}{\lambda}$ is the wavenumber, and λ is the wavelength of the point source. Note that the magnitude of the wave is inversely decreasing with the distance.

Consider a 2-dimensional plane (x, y), and the source distribution is defined by the function $U_1(x, y)$. At distance z, there is a second plane (u, v). As shown in figure 1.

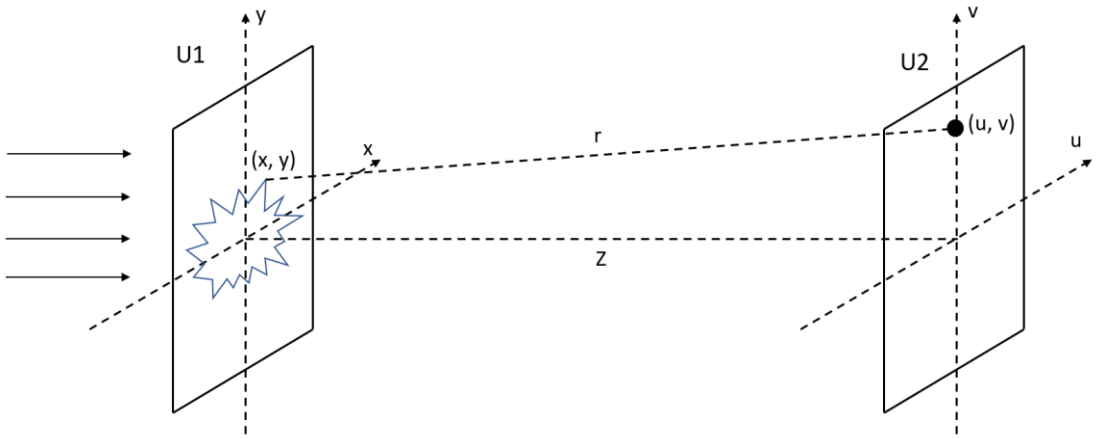

Figure 2.2. An illustration of wave propagation

According to the Huygens-Fresnel principle and the Rayleigh-Sommerfeld expression (Goodman 2005), the wave propagated to point (u, v) at the plane U_2 can be defined as the superposition of many wavelets, each scaled by the complex amplitude $U_1(x, y)$:

$$U_2(u, v) = \frac{1}{i\lambda} \iint U_1(x, y) \frac{e^{ikr}}{r} dxdy \tag{2.7}$$

$$r = \sqrt{z^2 + (u - x)^2 + (v - y)^2} \tag{2.8}$$

where r is the distance from a point at u_1 to the point at u_2.

The wave propagation can be further divided into two approximations according to the propagation distance, the Fresnel approximation and Fraunhofer approximation. These two

approximations can be distinguished by Fresnel number F. For an electron wave passing through an aperture and hit the screen, the Fresnel number is defined as:

$$F = \frac{a^2}{L\lambda} \tag{2.9}$$

where a is the radius of the aperture, L is the distance between the aperture and the screen, and λ is the wavelength.

2.1.3 Fresnel Approximation

Fresnel approximation can be used when Fresnel number $F \gg 1$, which is called the near field or Fresnel region. It is a simplified form of the Rayleigh-Sommerfeld expression. First, equation (2.8) can be approximated using Binomial theorem:

$$r = \sqrt{z^2 + (u-x)^2 + (v-y)^2} = z(1 + \frac{(u-x)^2+(v-y)^2}{z^2})^{\frac{1}{2}} \approx z + \frac{(u-x)^2+(v-y)^2}{2z} \tag{2.10}$$

and substitute equation (2.10) into equation (2.7), the Fresnel approximation can be defined as:

$$U_2(u,v) = \frac{e^{ikz}}{i\lambda z} \iint U_1(x,y) e^{\frac{ik}{2z}[(u-x)^2+(v-y)^2]} dxdy \tag{2.11}$$

2.1.4 Fraunhofer Approximation

The Fraunhofer approximation can be used when Fresnel number $F \gg 1$, which is called the far-field. The Fraunhofer approximation can be derived by expanding the Fresnel approximation:

$$U_2(u,v) = \frac{e^{ikz}}{i\lambda z} e^{\frac{ik}{2z}(u^2+v^2)} \iint U_1(x,y) e^{\frac{ik}{2z}(x^2+y^2)} e^{\frac{-ik}{z}(xu+yv)} dxdy \tag{2.12}$$

Since Fraunhofer approximation is considered in far-field, then the distance is

$$z \gg (x^2 + y^2) \tag{2.13}$$

then the Fraunhofer approximation can be further simplified to:

$$U_2(u,v) = \frac{e^{ikz}}{i\lambda z} e^{\frac{ik}{2z}(u^2+v^2)} \iint U_1(x,y) e^{\frac{-ik}{z}(xu+yv)} dxdy \tag{2.14}$$

which is a Fourier Transform with scaled reciprocal coordinate. Hence, the Fraunhofer approximation is carried out by applying Fourier Transform to the wave in simulation.

2.2 Electron scattering

Besides the free-space propagation, another important behaviour of electrons is the interaction with the specimens. The reason that TEM can be used to observe the specimen is that the electrons inside the TEM will interact with the specimen. More particularly, the electrons will be scattered by the atoms from the specimen. After the electrons pass through the specimen, the spatial distribution of the scattered electrons will be recorded by the detector. This spatial distribution of the electrons is called a diffraction pattern. By analysing the diffraction patterns of the specimen, the user can study the characteristics of the specimen.

In terms of the energy change during the scattering process, the electron scatter process can be divided into two categories: elastic scattering, and inelastic scattering. Elastic scattering refers to the scattering process that does not result in energy loss of the electrons; Inelastic scattering refers to the processes that result in a reasonable amount (with respect to the beam energy) of energy loss. Elastic scattering usually occurs at relatively low angles (1-10°). Although, when the electron beam interacts with the specimen, some electrons travel closely with the nuclei of the atoms, those electrons will be scattered into a much higher angle (>10°), or even back-scattered, in which the scattering process remains elastic scattering. Inelastic scattering occurs at very low angle (<1°) (Carter 2009).

The electrons that remain parallel to the incident beam (beam before interacting with the specimen) is called the direct beam. In TEM, the users are primarily interested in the direct beam and the electrons that do not deviate large angles, since those electrons form the diffraction pattern. Generally speaking, the more scattering events an electron experiences, the greater the scattering angle is, the more difficult to predict the behaviour of the electron, hence the more difficult to anticipate the characteristic of the specimen.

The simplest scattering process is single scattering, when an electron is only scattered once. If the electrons are scattered more than once, it can be considered as plural scattering, or multiple scattering (>20 times). The thicker the specimen is, the better chance that multiple scattering will occur, and the more difficult to analyse the specimen. Hence, while preparing the sample, people always prepare the sample into a thin slice.

During such interaction between electron beam and the specimen, the amplitude and phase of the electron beam change. These changes quantitatively describe the amplitude and phase information of the specimen model. The amplitude change can be directly viewed from the TEM, the phase shift, however, needs to be retrieved using computation imaging techniques, such as holography and ptychography, which are discussed in section 2.5 and 2.6.

In its simplest form, the phase difference of an electron beam after passing a thin film of specimen lying in the x-y plane can be described as (Midgley 2001):

$$\Delta\phi(x,y) = C_E V_0(x,y)t(x,y) \tag{2.15}$$

where $\Delta\phi(x,y)$ is the phase shift, V_0 is the mean inner potential (MIP), t is the thickness, and C_E is a wavelength-dependent constant given by:

$$C_E = \frac{2\pi e}{\lambda E}\left(\frac{E_0+E}{2E_0+E}\right) \tag{2.16}$$

where E is the energy and λ is the wavelength of the electron beam and E_0 is the rest mass energy of the electron. Equation (2.15) can only be applied to the specimen in absence of magnetic or electric fields. The MIP is a property of materials related to the surface dipole and defined as the volume average of the atomic electrostatic potentials in the specimen (Sun, Mao et al. 2018). MIP is an important and constant property for a given material and has been measured for many different materials (Sanchez and Ochando 1985, Cassidy, Dhar and Shintake 2017). With the recovered phase image and the known thickness of the specimen, the MIP can be calculated to assess the accuracy of the phase reconstruction.

For a specimen that contain the electric fields, the equation (2.15) is modified to:

$$\Delta\phi(x,y) = C_E \int V(x,y,z)dz \tag{2.17}$$

Where V is the electrostatic potential of the specimen. The integral in equation (2.17) is taken along the trajectory parallel to the beam direction z. This equation is used for describing the phase shift of the electron beam interacting with a charged specimen.

For a more complex specimen that contain the magnetic and electric fields, the equation (2.17) can be further modified to:

$$\Delta\phi(x,y) = C_E \int V(x,y,z)dz - \frac{e}{\hbar}\iint B(x,y).dS \tag{2.18}$$

where $\hbar = \frac{h}{2\pi}$ is the reduced Planck constant, B is the magnetic flux or induction, and S is the area mapped out by the electron beam. This equation can be used to describe the phase shift of the electron beam interacting with a magnetic specimen, such as the Mo-doped permalloy shown in Chapter 4.

2.3 Transmission Electron Microscopy

All of my research requires conducting experiments on the transmission electron microscope, either in the convention mode, Lorentz mode, or scanning transmission electron microscopy (STEM) mode. In this section, the reason to use TEM, and the components of the TEM are discussed.

2.3.1 What is Transmission Electron Microscopy

The TEM is an imaging instrument that reveals the detailed structure of the specimen by using high energy electrons transmitted through the specimen. The electrons inside the TEM interact with the specimen (mainly by scattering as mentioned in the previous section) and are then passed through lenses and collected by a detector. The extremely short wavelength of the electron beam in the TEM (see Section 2.1.1) means that its resolution capability far exceeds that of visible-light microscopy (VLM) or X-ray microscopy, and the strong electron interaction with the specimen, relative to photons, leads to high contrast material sensitivity. Hence, TEM has been widely used to study the internal structure of metals, alloys, semiconductors, and biological materials.

In 1925, a French physicist, Louis De Broglie, discovered that the electron has wave-like characteristics, and has a shorter wavelength than visible light (de Broglie 1925). According to Rayleigh criteria, the better resolution should be achieved if electrons can be used in microscope design. A few years later, in 1932, the prototype electron microscope was built by Ernst Ruska and Max Knoll (Brüche and Johannson 1932). Two years later, they developed the first electron microscope capable of achieving higher resolution than an optical microscope. In 1939, the Siemens and Halske in Germany built the first commercial electron microscope (Dominguez, Witherspoon et al. 2003). And the TEM became widely used from several facilities such as Hitachi, JEOL, Philips and RCA.

The TEM's ability of revealing highly magnified detail of the specimen relies on the highly accelerated electrons. According to equation 2.4, higher accelerating voltage leads to shorter wavelength. The resolution is defined as the minimum distance by which two points must be separated so that those objects can be distinguished from one another. The resolution is directly related to the wavelength. Other microscopy technology, such as VLM or X-ray microscopy, uses illumination sources which have much longer wavelength compared to electrons. Hence, the electron microscope can reach much higher resolution than other microscopy techniques. In a more scientific way, the classic Rayleigh criterion defines the minimum distance that can be resolved, δ, for VLM as

$$\delta = \frac{0.61\lambda}{\mu \, sin\beta} \tag{2.19}$$

where μ is the refractive index of the viewing medium, and β is the collection semi-angle. The visible light wavelength ranges between 380 to 700 nm, giving the best theoretical resolution of VLM as about 200nm (ignoring super-resolution fluorescence methods). For a typical TEM experiment with acceleration voltage of 80 kev and 20 mrad convergence semi-angle, the Rayleigh limit resolution is well below 1 nm. The combination of TEM and image processing techniques, such as ptychography, can even reach sub-angstrom resolution (Jiang, Chen et al. 2018). This powerful tool enables scientists to visualise the features in the crystal lattice, detect the defects and dislocations, as well as study the biological characteristic of virus.

Another advantage of TEM comes from the electrons being one type of ionizing radiation. Ionizing radiation is a form of energy that acts by removing electrons from atoms and molecules of materials. When the electron beam transfers energy to the inner-shell electrons from the atoms inside the specimen, a wide range of secondary signals are produced. These signals include secondary electrons, characteristic X-ray, visible light, etc. Most of these signals can be detected and analysed in different types of TEM, such as analytical electron microscopy (AEM). AEM uses X-ray energy-dispersive spectrometry (XEDS), Energy Dispersive X-ray spectroscopy (EDX), and Electron Energy Loss Spectroscopy (EELS) to reveal chemical information of the specimen such as elemental composition, bonding state, and band structure.

Among all the different types of TEM, scanning transmission electron microscopy (STEM) is particularly important for ptychography. In the conventional TEM mode, an unfocused electron beam illuminates the specimen. In the STEM mode, however, the condenser lens and objective lens focus the electron beam into a fine spot. This focused fine spot illuminates one position of the sample at a time and scans through the region of interest. The diffraction patterns from each position are recorded and integrated to form the image of the sample. A typical STEM is a conventional TEM equipped with scanning coils and necessary circuitry, allowing the operator to switch between STEM mode and conventional TEM mode. In the STEM mode, the resolution limit is determined by the electron beam convergence angle. STEM mode is commonly used in far-field ptychography. All the near-field electron ptychography experiments in this thesis, however, are conducted under the conventional TEM mode.

2.3.2 Components of TEM

The TEM is an extremely advanced equipment often costing millions of pounds. However, the ability to accurately characterise a broad range of specimens with such high spatial resolution is beyond any other form of microscopy. In this section, the components of the TEM are discussed.

Electron source:

The electron source, usually called the electron gun, generates an electron beam to transmit through the sample. To produce a well-defined, stable, and powerful electron beam, two types of electron gun are available: the thermionic emission gun and field emission gun.

Thermionic emission guns are used in most of the modern TEM. The thermionic emission gun works by heating up the gun to a certain temperature such that the electrons gain sufficient energy to escape the surface. The Richardson's law can be used to represent the physics of the thermionic emission:

$$J = AT^2 e^{-\frac{\Phi}{kT}} \tag{2.20}$$

where J is the current density of the emitted electron beam, A is the Richardson's constant for a given material, T is the operating temperature, k is the Boltzmann's constant, Φ is the

work function of the material in units of electron volts. According to the equation, the temperature needs to be high enough such that the energy is larger than the work function Φ to generate temperature. However, when the thermal energy reaches a few eV, most materials either melt or vaporise. Hence, the solution is to use a material with either high melting point or low work function Φ. The modern TEM uses lanthanum hexaboride (LaB_6) as the thermionic source, which has a melting point of 2480 K and Φ being 2.4 eV.

Another type of electron gun is the field emission gun (FEG). A FEG generates more monochromatic electrons but is more expensive than thermionic sources. Due to its ability to generate brighter and better spatial coherent beams, the FEG is currently expanding in the TEM community. The microscopes used in my research are all equipped with an FEG. FEG creates electrons by applying an electric field between the gun and an anode.

The working environment of FEG should be free of contaminants and oxide. Hence, the FEG usually operating in an ultra-high vacuum condition ($< 10^{-9}$ Pa). Under this condition, the FEG can be operated at ambient temperature, and this process is called 'cold' FE or CFE. Alternatively, the FEG can operate at poorer vacuum by heating up the tip, which is called 'thermal' FE or TFE.

There are three terms to assess the performance of the electron gun: brightness, coherence, and stability. Brightness, similar to the term in our daily life, is defined as the current density per unit solid angle. FEGs have higher brightness than thermionic emission guns at the same accelerating voltage. Brightness is important in STEM, in which the illumination probe has a small convergence angle. The brightness increases linearly with increasing the accelerating voltage. The higher the brightness, the more electrons pass through the specimen, so the more information is acquired about the specimen. However, the electrons could also damage the sample. So, a compromised value should be met. Another important term is coherence, more specifically, temporal coherence and spatial coherence. Coherence describes how well the electron waves are in phase with each other.

Temporal coherence λ_c is defined as:

$$\lambda_c = \frac{vh}{\Delta E} \tag{2.21}$$

where v is the electron velocity, ΔE is the energy spread of the beam and h is the Planck's constant. A coherent electron beam requires that the electrons have the same energy. From equation 2.4, same frequency means the accelerating voltage should stay constant, or in other words, the energy spread should be exceptionally small.

Spatial coherence directly relates to the spot size of the point source. If the electron beam is generated from a single point, then this beam is considered as fully spatial coherent. However, this is never the case, as all the electron sources have finite physical size. The FEG has a smaller spot size compared to the thermionic emission gun, so FEG has better spatial coherence. Coherence affects the resolution of the reconstructed images in my work. In STEM, it also affects the focal size of the beam. To improve the coherence, an operator can choose a lower accelerating voltage, smaller spot size and a smaller illumination aperture. But the brightness will be sacrificed. The last term to assess the performance of the electron sources is stability. It describes the variation of the beam current. The thermionic sources and TFE are generally more stable, with a $< \pm 1\%/hr$ drift in the current, than the CFE. For CFE, better stability requires better vacuum condition. Hence, depending on the purpose of the experiment, brightness, coherency, and stability should be considered together to choose the spot size, accelerating voltage etc.

Vacuum System:

As mentioned previously, electrons are strongly scattered by atoms, which includes atoms in the air. A vacuum system is therefore necessary to keep the electron beam free of unexpected scattering events. Another important reason to use the vacuum system is to keep the specimen free of contamination, including hydrocarbons and water vapor.

A modern TEM uses vacuum pumps to create the vacuum system, and the airlock system to preserve the condition. The TEM is kept permanently under vacuum condition except for repair or service. Hence, when the specimen is inserted, the specimen is placed in a special specimen holder. The specimen holder is firstly cryo-pumped to a matching condition with the vacuum system of the TEM, and then inserted into the TEM stage. The TEM stage is capable of tilting, rotating, heating, and cooling the specimen for different studies. However, the stage also introduces vibration, drift and contamination to the specimen and degrade the

analysis. In my research, the stage drift is an unavoidable constraint, and we contribute a lot of effort to correct this.

Lenses and apertures

Electron lenses are magnetic equivalents of glass lenses in VLM. They consist of a coil of copper wire wrapped around the soft iron pole piece. The current runs through the copper wire and forms an electromagnetic field, which shapes the electron beam. The magnetic field strength can be controlled by changing the strength of current through the coil. The electron lenses are used to:

- Take all the rays emanating from one point and recreate a point in an image with certain magnification.
- Focus parallel rays to a point in the focal plane of the lens.

Since the coil heats up when the current runs through it, a water-cooling system is required to preserve the vacuum system inside the TEM.

However, a major limit of the electron lens is that it suffers severe spherical and chromatic aberration, which will be discussed in the following section in detail. Although modern technology has been able to overcome this limitation, aberration correction TEM are expensive. For most TEM, apertures are inserted only allowing through the ray nearest to the optic axis, since those are least affected by the aberration. There are many types of apertures located in the image and back focal plane of various lenses. Unfortunately, even with all the above-mentioned measures, all TEM still suffer from aberrations, and this will directly degrade the performance of the TEM, mainly the resolution. One aperture that will be important in my work is in the objective lens image plane and can select the area of interest to project onto the detector (select area aperture).

The lenses in TEM can be divided into three categories: condenser lenses, the objective lens, and projector lenses. The condenser lenses are located at the top of the TEM and used to form the illumination onto the specimen. The condenser lenses and the electron source together are called the illumination system. The first two condenser lenses (C1 and C2) are adjusted to illuminate the specimen with a parallel beam with designed size. C1 collects the electrons from the gun and forms an image of the gun at the C1 crossover, as shown in Figure

2.4. C2 is weakened and under focus (the crossover occurs after the image plane) to form a near-parallel illumination on the specimen, as shown in Figure 2.4 a. A more practical way to form the parallel illumination is to use the upper objective lens, which is also called C3 lens, as shown in Figure 2.4 b. The difference is that the C2 lens is focused and forms image of the electron gun at the front focal plane. Then a parallel beam is formed by the upper objective lens. This is the standard way to form parallel illumination on most of the TEM.

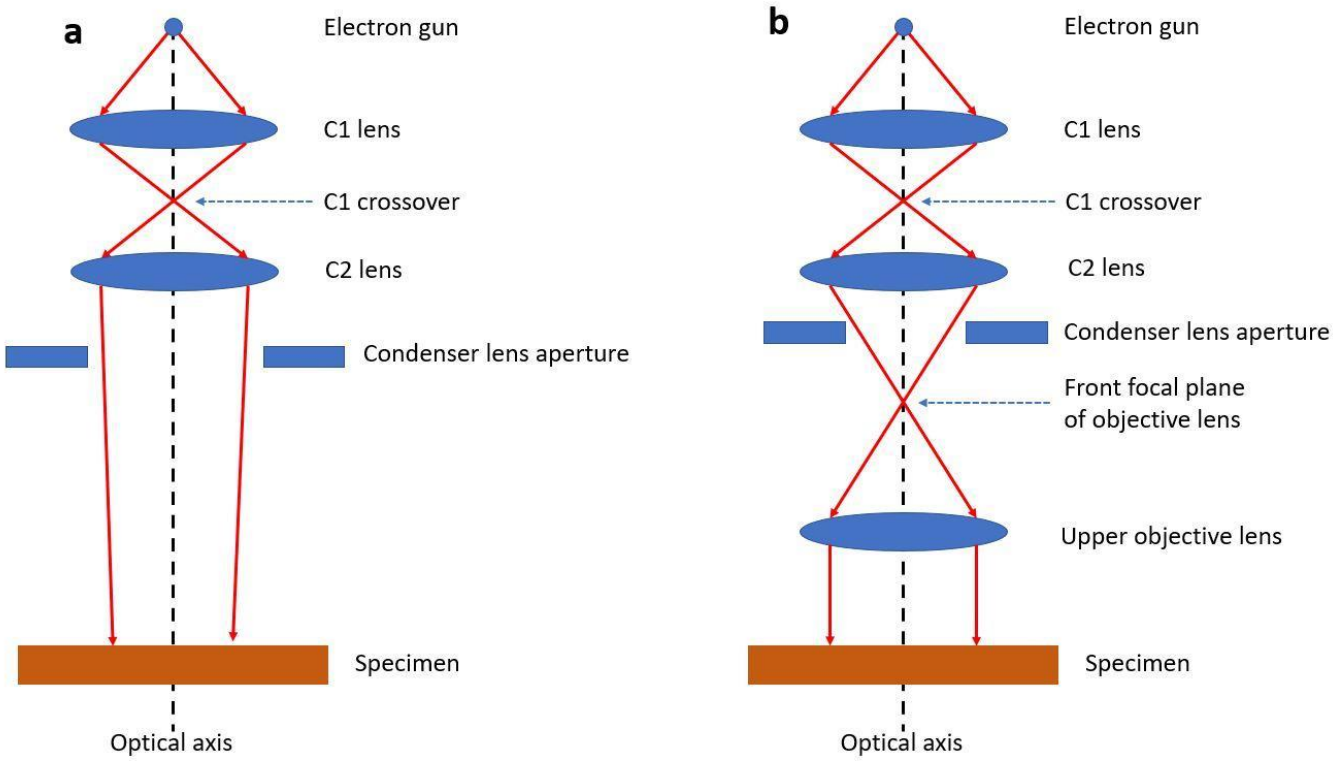

Figure 2.4 Methods to form parallel illumination in TEM. (a) using C1 and underfocused C2 lens. (b) C1 and C2 form the image of the gun at front focal plane and upper objective lens create the parallel illumination onto the specimen

The condenser lens aperture is located between C2 lens and C3 lens. Generally, it is used to block the electrons that are far away from the optical axis and reduce the aberration. In my research, it is also used to mask the parallel illumination and form a non-uniform probe.

The objective lens has the greatest magnifying power of the lenses in TEM. It produces the first image of the specimen at the back focal plane. The specimen is placed between the upper and lower pole pieces of the objective lens. However, some of my research uses magnetic samples, the magnetic field created by the objective lens will interact with the magnetic field

from the specimen. In this case, the Lorentz mode is used where the objective lens is turned off to preserve the intrinsic magnetic characteristic of the specimen.

The projector lenses are located below the objective lens. They propagate and magnify the images of the sample to the detector.

Detector

Detector is the device located at the bottom of the TEM that collects and records the spatial distribution of the electrons. Most modern TEM are equipped with Charge-Coupled Device (CCD) detectors. CCDs are metal-insulator-silicon devices that store charge generated by electrons. It consists of many closely-located units, which are called pixels. Each pixel is an individual capacitor electrically isolated from each other. Pixels accumulate the collect charge and produce a readout value. All the pixels readout together formed a diffraction pattern.

2.4 Limitation of TEM

In the previous section, an electron microscope is compared with a visible light microscope. Over 300 years of development of visible light microscopes, the perfect glass can be fabricated. Electron lenses, on the other hand, are far from perfect. These imperfections limit the resolution of the final result. Three major defects of the electron lens are spherical aberration, chromatic aberration, and astigmatism. In this section, the cause of these defects and the compensation measurement are discussed in detail.

2.4.1 Spherical aberration

Spherical aberration, denoted as Cs, occurs due to the different parts of one electron lens bend the electron beam by various degrees. For electron lenses in TEM, the further off the axis the electron is, the more strongly it is bent back toward the axis, as shown in Figure 2.5. As a result, a point is imaged as a blurred disk. The disk has high intensity at the centre, the

surrounding has decreasing intensity. This effect will degrade the detail of the specimen, and lead to worse resolution.

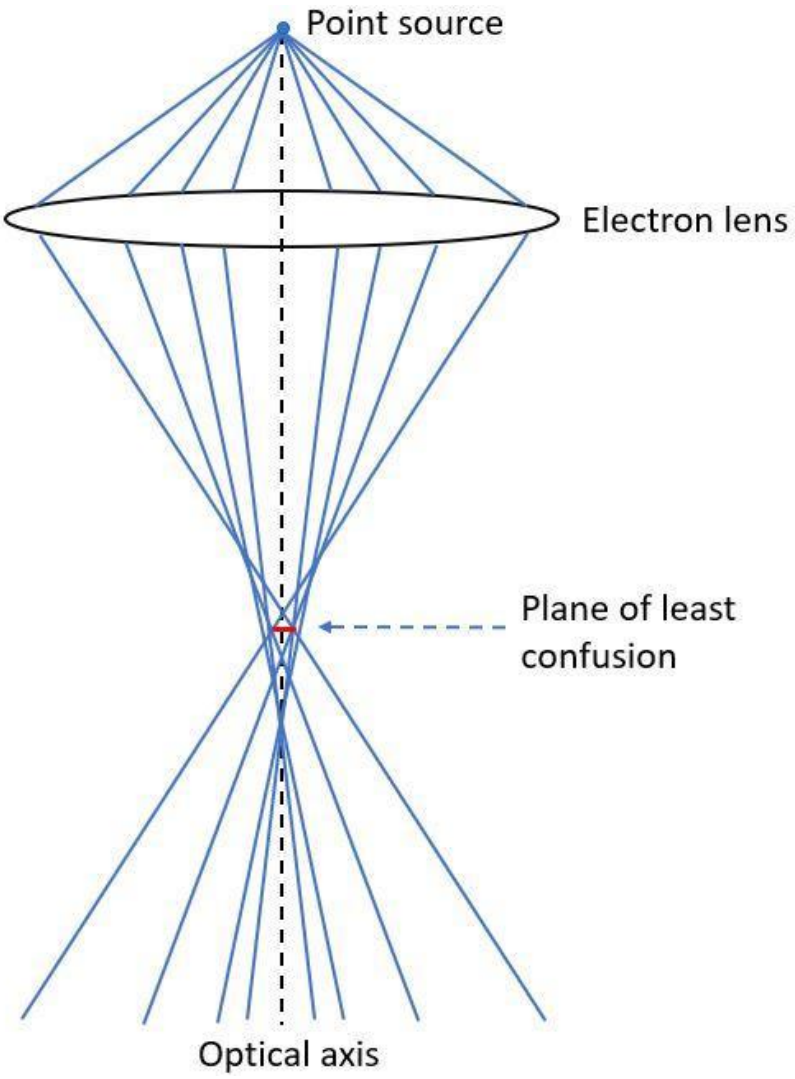

Figure 2.5 Spherical aberration in the lens causes the electron beam to be bent by different degrees. The rays further away from the optical axis are more distorted. The point source is imaged as a disk at the plane of least confusion.

The term Cs, called spherical aberration coefficient, is used to describe how much the rays are distorted. Cs is a constant for a given electron lens. One simple way to correct the spherical aberration, as mentioned previously, is to place an aperture to block the rays that are far away from the optical axis. One more precise method to compensate for Cs is to use a diverging lens which spreads out the off-axis beams such that they re-converge to a point rather than a disk. In modern TEM, this is achieved by a set of complex and computer-

controlled quadrupoles and hexapoles or octupoles. However, these measures will significantly increase the price of TEM.

2.4.2 Chromatic aberration

Chromatic aberration occurs due to the fact that the electron beams are not monochromatic. In other words, the electrons have different energies. The modern electron source is generally stable and has relatively small power fluctuation. Hence, the energy spread may vary from ~ 0.3 eV (cold FEG) to ~ 1 eV (LaB_6). However, after the electron beam passes through the specimen, inelastic scattering unavoidably happens and causes the electron loss of energy. The objective lens bends electrons of lower energy more strongly thus electrons from a point of the object once again form a blurred disk. The radius r_{chr} of this disk can be calculated as

$$r_{chr} = C_c \frac{\Delta E}{E_0} \beta \tag{2.22}$$

where C_c is the chromatic aberration coefficient, ΔE is the energy loss of the electrons, E_0 is the original beam energy, and β is the angle of collection of the lens. Chromatic aberration gets worse as the specimen gets thicker. Hence, it is important to keep the specimen thin. Unfortunately, most of the specimens are not thick enough to ignore the chromatic aberration effect from the exit wave. Energy filtering is a popular method to compensate for this.

2.4.3 Astigmatism

Astigmatism occurs due to the electrons facing a non-uniform magnetic field as they pass through the electromagnetic lens. This is mainly because the pole piece is not manufactured perfectly cylindrically symmetrical. The soft iron may also be inhomogeneities, which cause local variation in magnetic field. The aperture around the lens may disturb the magnetic field if not precisely centred. Furthermore, if the aperture is not perfectly clean, the contamination could charge up and distort the magnetic field. The astigmatism can be described as

$$r_{ast} = \beta \Delta f \tag{2.23}$$

where Δf is the maximum difference in focus induced by astigmatism. As a result, the reconstructed image would appear stretched in a certain direction. Astigmatism, unlike

previous defects, can be easily corrected using stigmators, which are small octupoles that introduce a compensating field to balance the inhomogeneities (Carter, William, 2009). The stigmators are placed in both the illumination system and objective lens.

2.5 Holography

Electron holography was originally proposed as a method of correcting the lens aberration (Midgley 2001). This technique relies on the formation of interference patterns in the TEM. It is developed from earlier experiments in electron interferometry (Jönsson 1961, Merli, Missiroli and Pozzi 1976, Tonomura, Endo et al. 1989). The first implementation of holography is an in-line holography (Gabor 1949). In this setup, a parallel beam of light was used to illuminate the specimen and collected by photographic screen. However, Gabor did not successfully reconstruct the specimen due to the twin image problem. This problem was tackled by using the off-axis mode (Leith and Upatnieks 1962). The modern off-axis electron holography has the geometry as in Fig 2.6.

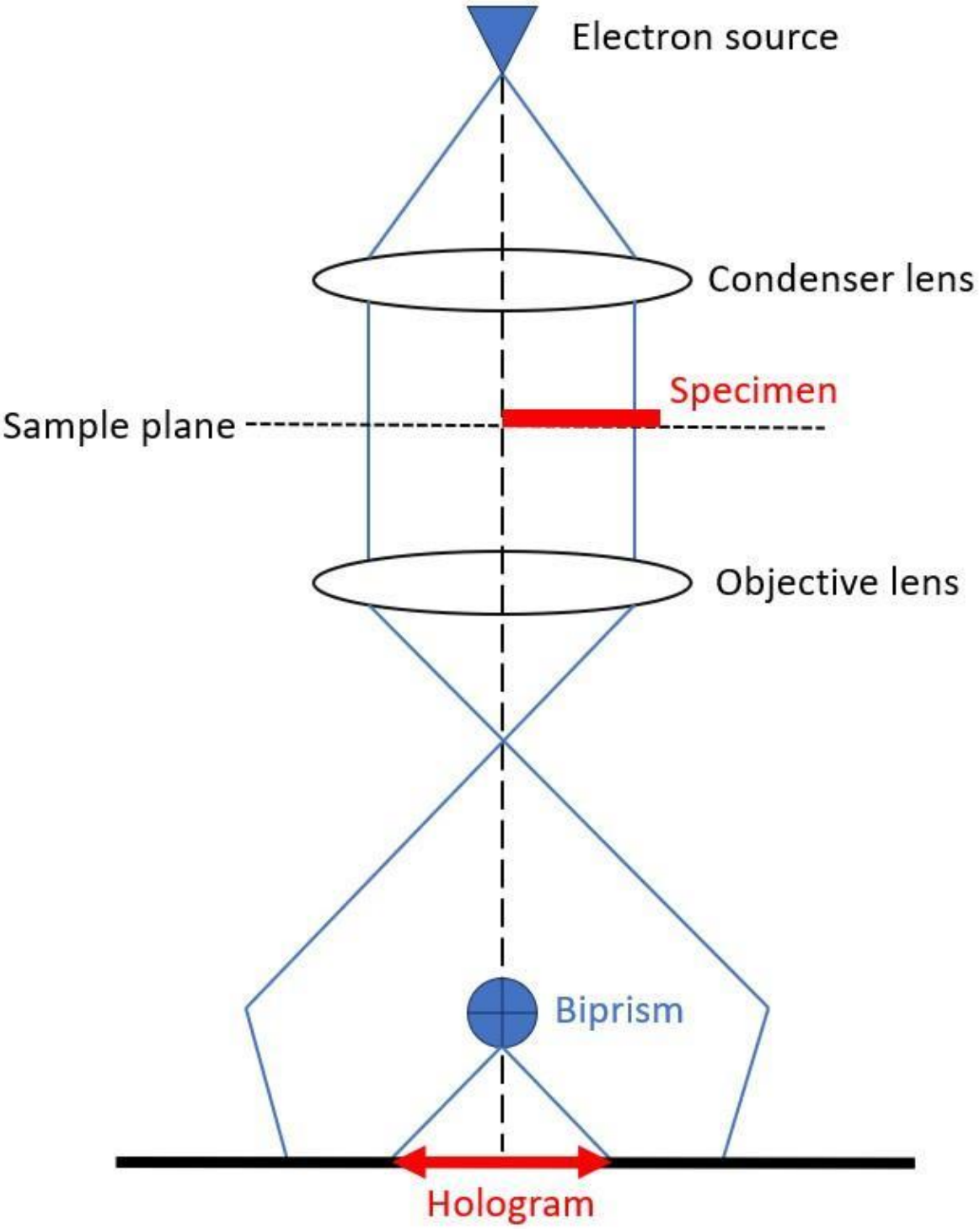

Fig 2.6. The electron microscope geometry for the TEM mode of off-axis electron holography.

The specimen is positioned such that it only occupies half the field of view. A voltage is applied to the electrostatic biprism. The biprism separates the electron beam and creates a reference wave. The reference wave passes through the vacuum and does not contain the information of the specimen. This reference wave interacts with the electron wave that passes through

the specimen at the detector. These two waves overlap and create an interference fringe pattern at the detector. The phase information of the specimen is contained inside the hologram. The reconstruction of the phase information is quick and easy. The hologram is Fourier transformed and one of the sidebands (an intensity peak at the Fourier domain) is cutout. The cutout sideband is then centred and back-propagated to form the modulus and phase images of the specimen. The ability to recover the phase information of the specimen made it a powerful tool in the electron community (Lichte and Lehmann 2007, McCartney and Smith 2007). As the phase shift is sensitive to local variations in magnetic and electrostatic potential, this technique was also used to image the magnetic structure, such as domain wall (Junginger, Kläui et al. 2007) and individual magnetic nanostructures (Bromwich, Kasama et al. 2006). In this thesis, we use near-field electron ptychography to image the magnetic features of Mo-doped permalloy, which is prepared by Dr Thomas Schachinger from Tu Wien. To assess the accuracy of our reconstruction, the same specimen was also imaged using off-axis holography, and the results are compared, details in Chapter 4.

2.6 Ptychography

Ptychography, which uses an inverse computation algorithm to reconstruct specimens, is an advanced image processing technology. It is a powerful tool to retrieve the phase information from the diffraction patterns collected using TEM. This subsection first introduces the basic concept of ptychography in 2.5.1. And the algorithm of ptychography, ePIE, is discussed in 2.5.2.

2.6.1 The basic concept of ptychography

In 2012, it is shown for the first time, that it is possible to recover both modulus and phase at atomic resolution, over an unlimited field of view using low energy (30 keV) electrons (Humphry, et al. 2012), and it is also shown that with further development, the resolution could reach a sub-atomic scale. Apart from the ability of recovering the phase information, another great potential of ptychography is to improve the resolution. In 2018, a group in Cornell University achieved an equivalent resolution 0.39 Å, using electron ptychography, for which conventional imaging methods reach only 0.98 Å at the same accelerating voltage and imaging conditions (Jiang, Chen et al. 2018).

The idea of ptychography was originally proposed by Hegerl and Hoppe as a solution to the crystallographic specimen using scanning transmission electron microscope (STEM) in around 1970 (Hoppe 1969, Hegerl and Hoppe 1972, Hoppe 1982, van Benthem, Lupini et al. 2006). And the technique was extended to a non-crystallographic specimen by Rodenburg in 1989 (Bates and Rodenburg 1989). However, due to the large size of the dataset and limited computer technology at that time, the idea was not further developed. In the last 20 years, improved algorithms such as ptychographical iterative engine (PIE) (Rodenburg and Faulkner 2004) and extended ptychographical iterative engine (ePIE) (Maiden and Rodenburg 2009) were designed and ptychography was widely developed since then.

The modern ptychography works as illustrated in Figure 2.6.

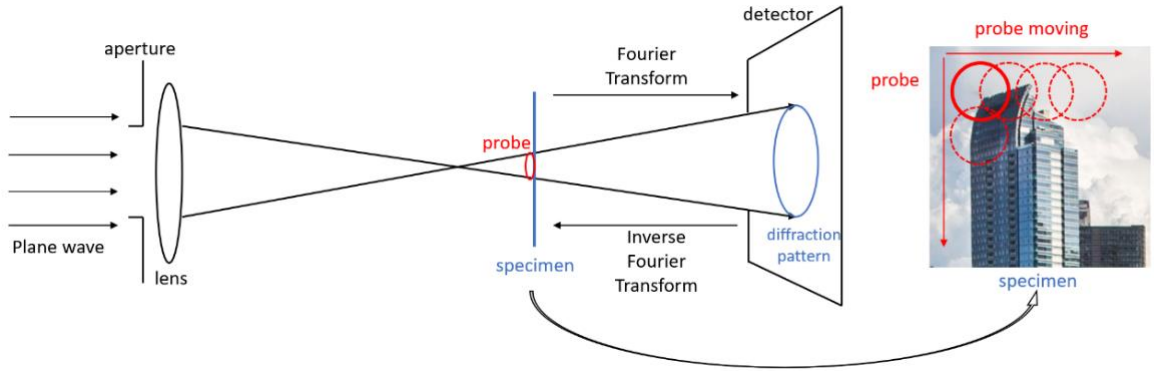

Figure 2.6. An illustration of how ptychography works in the scanning transmission electron microscope (STEM).

The whole process can be divided into two parts, collection and reconstruction. For collection, a converged illumination wave goes through the specimen, which is in real space, and the exit wave is Fourier Transformed (assuming the detector is placed in the far-field) and recorded at a detector, which is in "reciprocal space". Note that only intensity is recorded, and this distribution of intensity is called a diffraction pattern. Then move the probe to a new position, which has overlap with the previous probe illuminated area, hence introduce the redundancy into data, and do the whole process again. In the end, a set of diffraction patterns are generated and stored for reconstruction.

For reconstruction, simulate the same process but initially with an arbitrary specimen transmission function. When the exit wave arrives at the detector, replace the intensity from the arbitrary specimen transmission function with the stored diffraction pattern from the

same position, in this way, the information from a real specimen is fed into the simulation, and the wave is 'corrected' by the real data. This is also called the reciprocal space constraint, which means the modulus of the wavefront must be equal to the square root of the intensity of the recorded data. Apply the inverse Fourier Transform on the 'corrected' wave and update the specimen transfer function, which represents the modulus and phase information of the specimen, using real space constraint. Real-space constraint means that the modulus and phase information of the object and probe are constant in every probe position. The update process is applied to all diffraction patterns with their corresponding scan positions. After updating all the scan positions, repeat the update of the whole specimen transfer function many times, hence 'iterative', and in the end, both modulus and phase of the specimen transfer function can be reconstructed. The schematic representation is shown below:

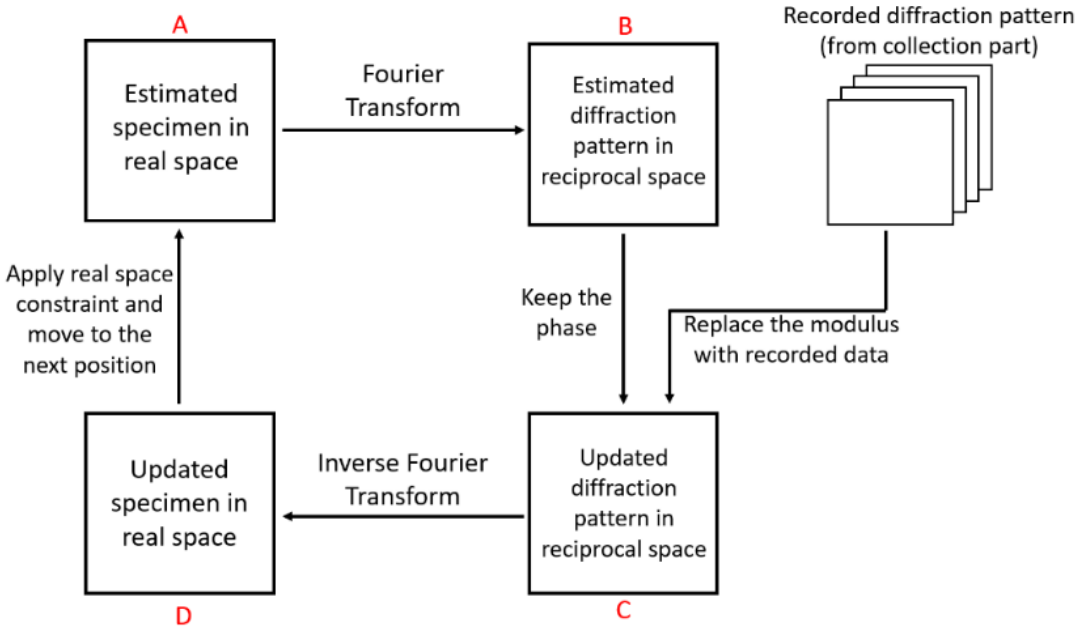

Figure 2.7. Schematic representation of ptychography. From B to C, reciprocal space constraint is applied, from D to A, real space constraint is applied.

Ptychography has many advantages. Firstly, it does not require a high-quality lens, which can be very expensive or impossible to make (as in electron and X-ray microscopy). The lens in this setup is merely used to form a convergence illumination. Secondly, it can get a much higher resolution reconstruction result than traditional optic technology. In 2018, a group at Cornell University has achieved a record-breaking 0.39 ångströms resolution (Jiang, Chen et al. 2018). Thirdly, it can very efficiently solve the image phase problem. The detector only

records the intensity of the exit wave, but the phase part of the complex coefficient is lost, which is called an image phase problem. At the end of ptychography reconstruction, both modulus and phase of the specimen transfer function are presented. This allows transparent objects to be seen clearly. Also, in the application of biology, it means the cells do not need to be stained or labelled.

2.6.2 ePIE

ePIE is one of the most widely used reconstruction algorithms. All the experimental data was reconstructed using ePIE. To use ePIE, the initial guess for the probe needs to be reasonable, in other words, the aperture size and defocus etc should be a reasonable guess about the real one. And the initial guess for the specimen transfer function can be arbitrary, which usually starts with a completely transparent object. The steps in the algorithm are as follows:

Step 1: start with simulating a candidate estimate of the probe P, interacting with the estimate of the specimen transfer function O, resulting in the exit wave Ψ.

$$\psi_j(x) = P_n(x - x_j)O_n(x) \tag{2.24}$$

Assuming this is n-th iteration, at position vector x, considering the specimen is 2D. The vector x_j denotes the relative position change between the probe and specimen. The interacting process is modelled using multiplication, called multiplicative approximation (Rodenburg and Faulkner 2004).

Step 2: propagate the exit wave to the detector using Fourier Transform to form the diffraction pattern, u is the position vector in reciprocal space.

$$\Psi_j(u) = F[\psi_j(x)] \tag{2.25}$$

Step 3: Replace the modulus of the diffraction pattern with the experimental data $I_j(u)$

$$\Psi_j{}'(u) = I_j(u)\frac{\Psi_j(u)}{|\Psi_j(u)|} \tag{2.26}$$

Step 4: propagate the corrected diffraction pattern back to real space

$$\psi_j{}'(x) = F^{-1}[\Psi_j{}'(u)] \tag{2.27}$$

Step 5: update both probe and specimen estimates according to:

$$O_{n+1}(x) = O_n(x) + \alpha \frac{{P_n}^*(x-x_j)}{max|P_n(x-x_j)|^2}(\psi_j{}'(x) - \psi_j(x)) \quad (2.28)$$

$$P_{n+1}(x) = P_n(x) + \beta \frac{{O_n}^*(x-x_j)}{max|O_n(x-x_j)|^2}(\psi_j{}'(x) - \psi_j(x)) \quad (2.29)$$

The term α and β represent the update step-size, which determines the feedback of the update. A higher value of α and β increase the importance of the update, both are usually set 1. The max function is used to have a weight function about the update. This function makes the update function highlight the area that is strongly illuminated.

The algorithm will go through all the positions and move onto the next iteration. After the defined iterations are finished, both the probe and the specimen will be reconstructed.

2.7 Fourier Ring correlation

After the reconstruction finished, one of the most important steps is to determine the resolution of the reconstructed result images. One method is to measure the minimal resolvable distance between two independent structures, also known as Rayleigh/Abbe resolution definition. Although this method is intuitive and robust, it does require the more manual work and prone to subjective bias. Another metho, which is fully automatic and less prone to subjective bias, is called Fourier Ring Correlation (FRC). (Van Heel, et al. 1982, Saxton, Baumeister. 1982). It measures the degree of correlation of two independent images at different spatial frequency. Then it measures the resolution by analysing the effective cut-off frequency. The cut-off frequency is the frequency that the correlation curve drops below a certain threshold. At low spatial frequency part, the FRC histogram is close to unity, indicating high degree of correlation. As the frequency gets higher, the degree of correlation between two images also decreases. For the frequency component higher than the cut-off frequency, the non-correlated, or independent, noise dominates the correlation curve. In our work, the two independent images are form by producing two independent reconstructions, each using half of the collected datasets. And the threshold method is half-bit criteria, which means the threshold is defined at the correlation coefficient reaches half of the pixels. Other criteria, such as fixed 1/7, was also tested and gave the similar results.

Chapter 3. Near-field electron ptychography in conventional TEM mode.

As discussed in Chapter 1, previous near-field electron ptychography uses either the SAA itself or a phase diffuser located in the SAA to modulate the electron beam. With these methods, the sample was constantly exposed to the electron beam, even in areas outside of the region masked by the SAA, and the phase plate introduced additional unwanted inelastic scatter, so this approach did not make optimal use of dose, whilst changing the magnification of the setup to image at different resolutions involved changing the size of the SAA so that a full set of diffuser-equipped apertures were required for multi-scale imaging (Allars, Lu et al. 2021).

In this chapter, a new experimental arrangement is proposed to overcome these limitations, in which a novel amplitude diffuser is located in the condenser aperture rather than the SAA. The experimental configuration is discussed in section 3.1. The design of the amplitude diffuser is explained in section 3.2. The experiment design is demonstrated in section 3.3. The reconstruction process, problems raised during the reconstruction process and its solution are in section 3.4. Finally, the results of our analysis are placed in section 3.5.

3.1 Experimental arrangement

The experimental configuration of the new method is shown in Fig 3.1a. A 50-μm diameter amplitude diffuser, shown in Fig3.1b, is inserted at the condenser lens aperture. The

microscope operates in the conventional brightfield TEM mode, so that a roughly parallel beam, structured by the amplitude diffuser, illuminates a region of interest on the sample. The exit wave after the sample then passes through the objective and projector lenses and is collected by a detector placed at a slight defocus. An example diffraction pattern is shown in Fig 3.1c. The sample is translated by the sample holder's motorised stage in a raster fashion.

The previous phase diffuser was an etched-thickness design. The diffuser structures the electron beam by adding spatially varying phase delays depending on the thickness. However, additional inelastic scattering is inevitably introduced during this process. The amplitude diffuser, shown in Fig 3.1b, is a 'hollow' design. The black lines are thin sections of the silicon nitride (SiN) substrate, while the white areas are empty (vacuum). The electron beam either passes freely through the vacuum or is completely blocked by the diffuser (black lines). In this case, the illumination is structured without introducing additional inelastic scattering.

Another difference between this design and the previous one is the electron do se efficiency. In the previous configuration, the sample is constantly exposed to the electron beam, but only a fraction of the dose passes through the SAA and reaches the detector. In our configuration, without using the SAA to choose the region of interest, the entire dose is transmitted to the detector and nearly all the electrons passing through the sample contribute to the diffraction pattern (inelastic scatter from the sample does still introduce a background signal). Hence, the electron efficiency is improved, and the beam damage to the sample is reduced.

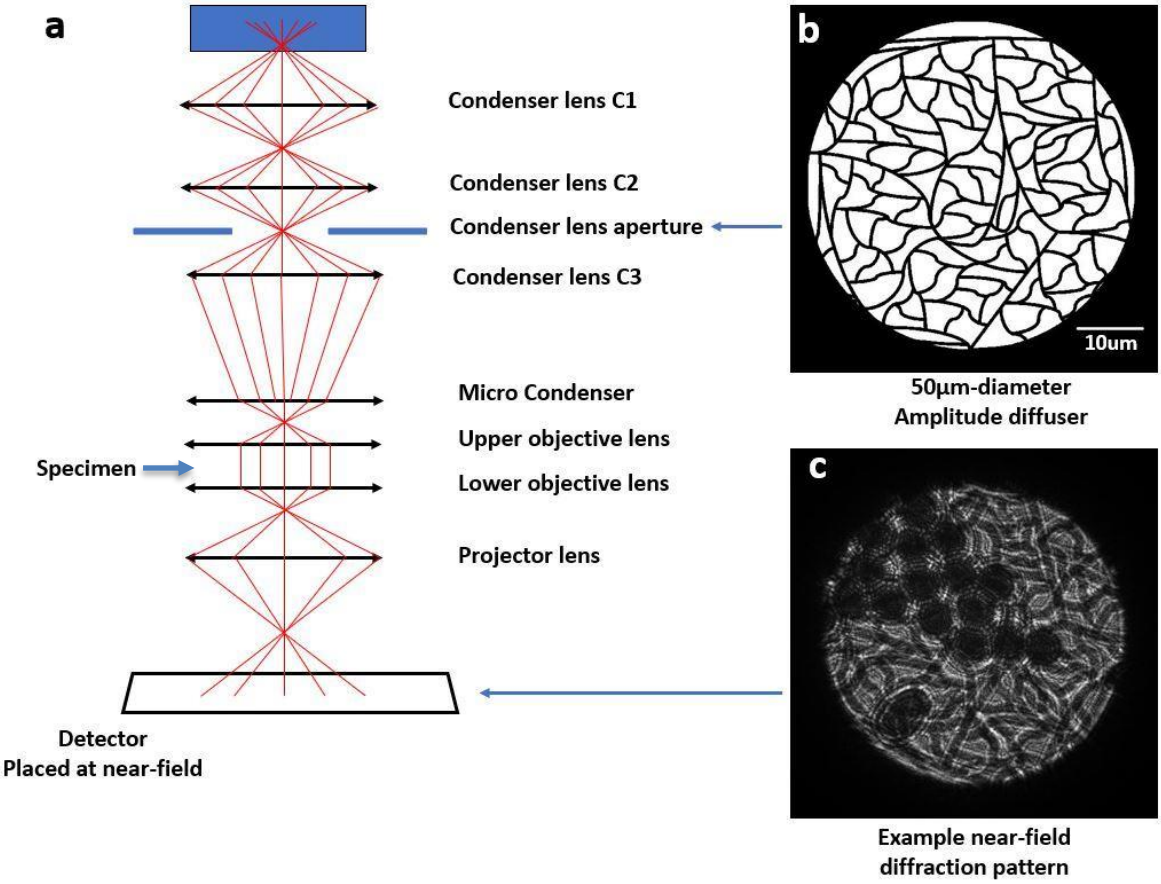

Fig 3.1. (a) The experiment setup of near-field electron ptychography. A parallel illumination probe, including features projected from the amplitude diffuser, propagates through a small area of the sample. (b) The amplitude diffuser is inserted at the condenser lens aperture. The scale bar is 10 µm (c) An example near-field diffraction pattern with latex spheres as the sample.

A further important difference in this configuration, compared to the previous design, is the capability of using various illumination sizes and magnifications without changing the diffuser. Since the amplitude diffuser is placed at the condenser lens aperture, the size of structured illumination can be easily changed by tuning the strength of the C3 and the objective lenses.

3.2 Design of the amplitude diffuser.

The design purpose of the amplitude diffuser is to mask the illumination profile with the Fresnel fringes from the SiN bars. To ensure the propagation-generated Fresnel fringes can cover the entire illumination within the near-field propagation distance. The adjacent SiN

structure should be placed within a reasonable distance to guarantee the surrounded blank areas are fully covered by the fringes. An SEM image of an initial design is shown in Fig 3.2.

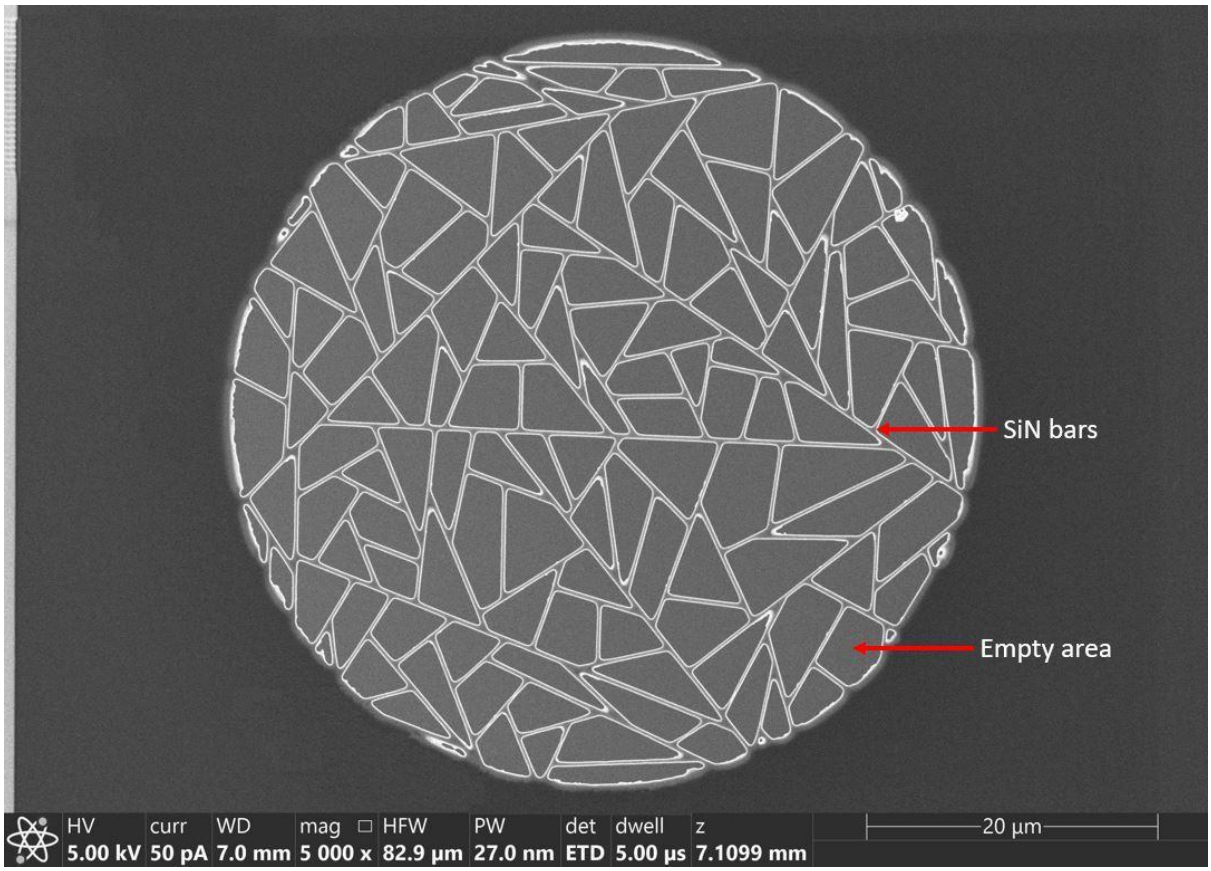

Fig 3.2. The initial amplitude diffuser design was viewed under SEM. The diameter of this diffuser is 50µm.

In this design, the straight lines separate the diffuser into areas with different shapes. The blank areas are designed to be irregular shapes so that the fringes have a sufficient spatial frequency. The size of each area is set to be small enough that the fringes can cover the centre point of each area after a certain propagation distance. A larger line width of each SiN bar will block more electrons, meaning fewer electrons reach the sample. A thin SiN bar, on the other hand, will make the diffuser more fragile and increase the difficulty of the fabrication process. The compromised value is set to be 350 nm for this 50 µm-diameter design. To further improve the spatial frequency of the SiN bars, a similar design with curved lines rather than straight lines was designed and fabricated. To compare the spatial frequency of these two designs, the Fourier Transform is performed on both amplitude diffusers. The results are shown in Fig 3.3.

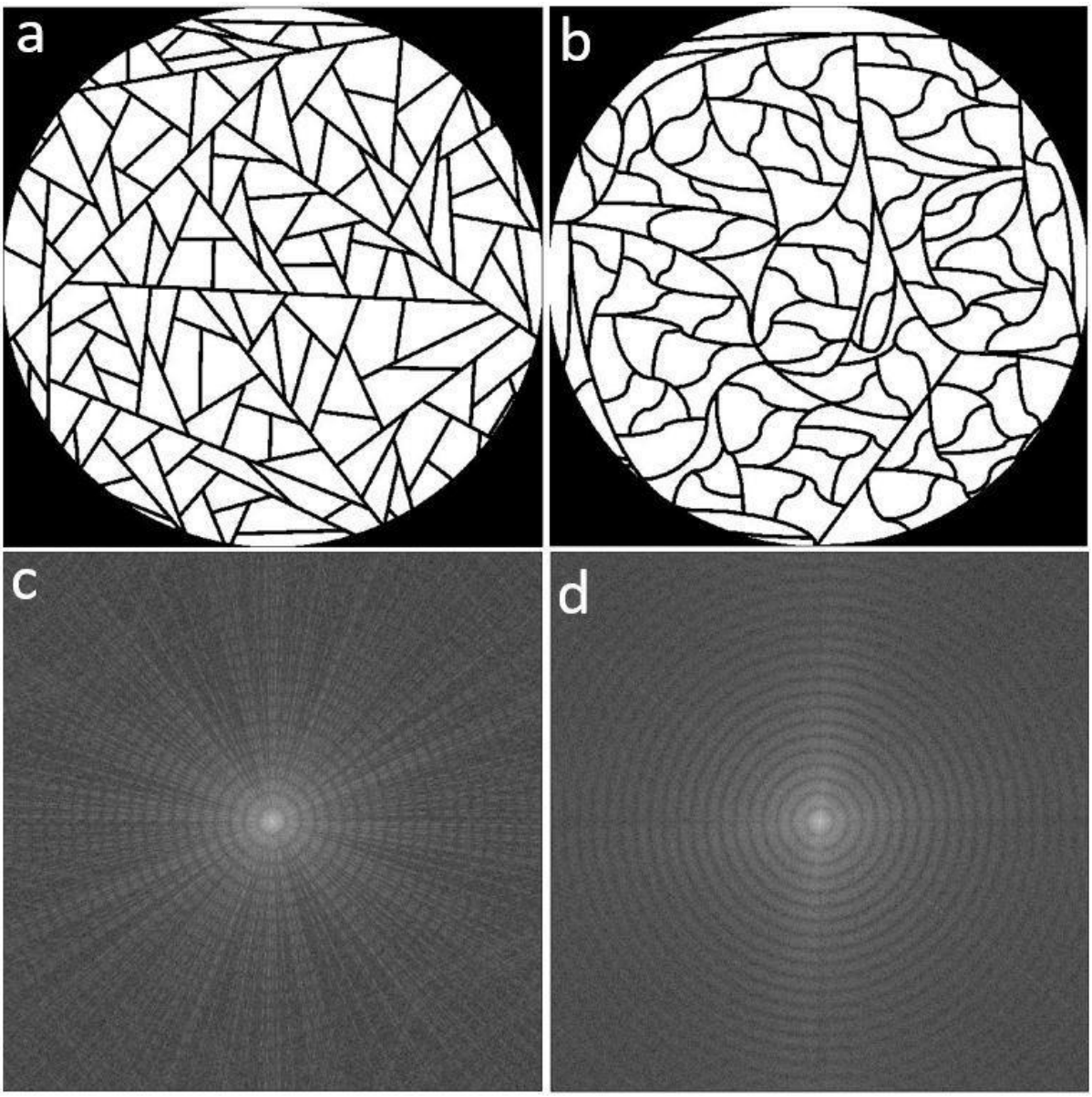

Fig 3.3. (a) and (b) are the straight-line design and curved-line design of the amplitude diffusers respectively. (c) and (d) are the Fourier Transform of the amplitude diffusers. The Fourier Transform of the curved-line design (d) has a more comprehensive spatial frequency.

The initial amplitude diffuser patterns are generated using drawing tools. The drawings of diffuser patterns are then converted into a bitmap for fabrication. To mail the line width to 350 nm , each amplitude diffuser pattern is drawn with 4 different widths, shown in Fig 3.4. The bitmap milling process began with the 1000 nm line width pattern to shape the inner structures. And then polished the line edge with 700 nm and 500 nm, eventually reaching the 350nm designed line width. The detailed fabrication process is beyond the scope of this

research, which is carried out by Dr Andras Kovacs from Ernst Ruska-Centre for Microscopy and Spectroscopy with Electrons and Peter Grünberg Institute, Germany.

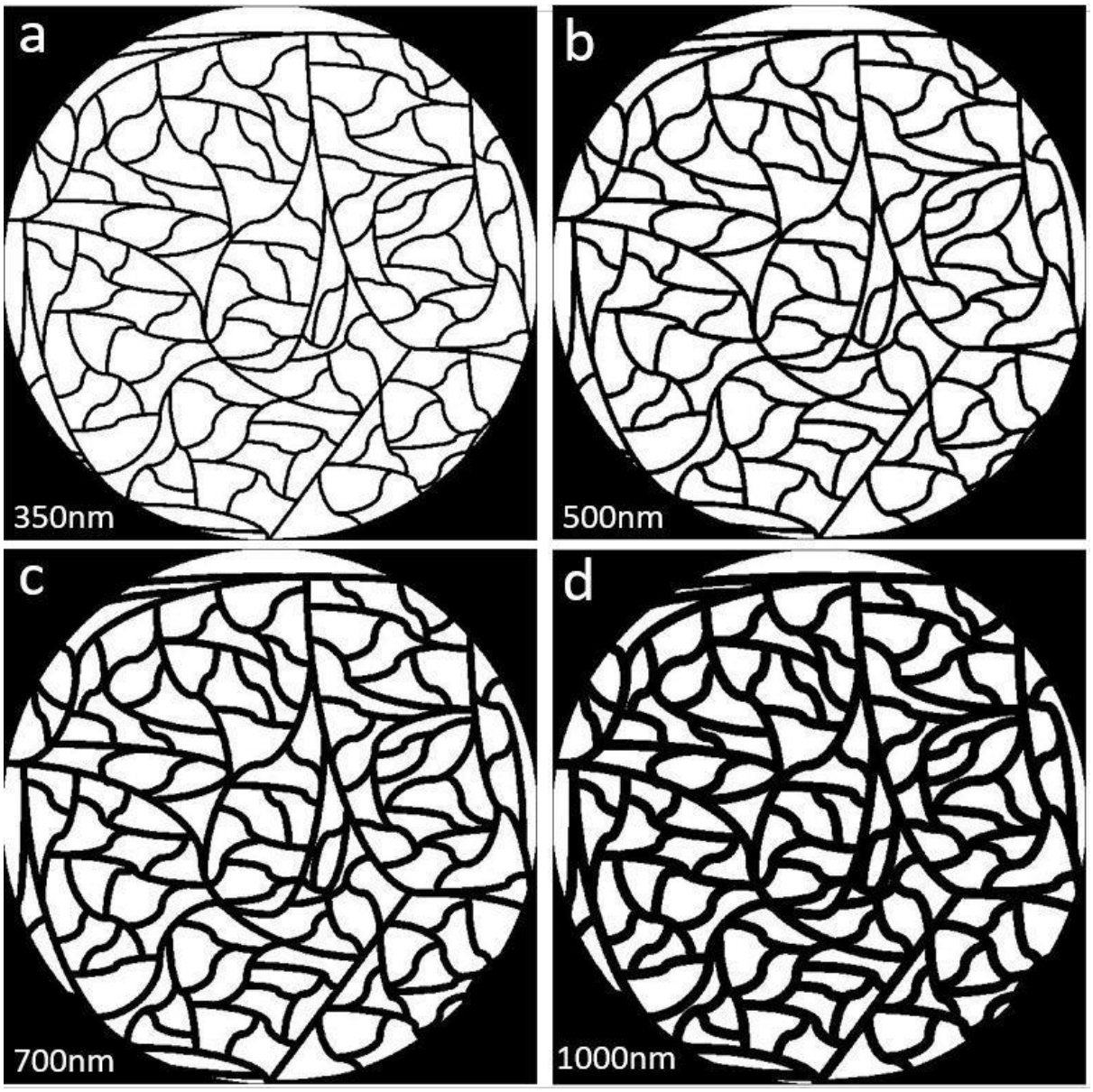

Fig 3.4. Random curved line amplitude diffuser patterns with different line widths. The line widths of (a) to (d) are 350 nm, 500 nm, 700 nm and 1000 nm.

3.3 The experimental design.

The experimental configuration discussed in session 3.1 is implemented on the C_s-corrected Titan HOLO electron microscope at Ernst-Ruska Centre, Forschungszentrum Juelich GmbH, Germany. The microscope was operated at 300 keV, corresponding to a wavelength of 1.97

picometers, with spot size 3 under the conventional brightfield TEM mode. The sample was translated using the stepper motor stages on the sample holder, programmed via Digital Micrograph scripts.

The camera length was 2.95 m, the largest camera length available for this microscope. The objective and projector lenses are tuned such that the detector is equivalently placed at a near-field position. The detector is a Gatan K2 detector (model number 1000) with 3840 × 3712 pixels on a 5 µm pitch. A central 2048 × 2048 pixel region of each diffraction pattern was cut from the full frame data.

To demonstrate the capability of using variable illumination sizes with the same diffuser, one diffuser is used to construct three different illumination profiles, with sizes being 2 µm, 1 µm and 0.5 µm. The stage moves in a raster fashion with 10 steps in each direction, 100 scans in total. The step sizes are 10% or 20% of the corresponding illumination probe sizes. The exposure time is 0.1 seconds. Under K2 linear mode, 20 images are taken within one minute. The total collection time for such 100 scans is approximately 5 minutes.

We used as a test sample a 463 nm gold-shadowed carbon diffraction grating replica populated with polystyrene spheres 263 nm in diameter. The known size and shape of the polystyrene spheres and the known grid spacing of the carbon replica help us assess the accuracy of our reconstructions.

3.4 The reconstruction process.

In this section, the reconstruction process is discussed in detail. An overview of the reconstruction process, together with a flow chart is introduced. The rest of this section is divided into a few subsections. Subsection 3.4.1 focuses on the initialization stage of the reconstruction process, including reading and calculating experimental parameters. Subsection 3.4.2 explains the reason for not using the scan position grid from the TEM, and how a cross-correlation method can be used instead to reproduce the scan positions. Subsection 3.4.3 discusses how to assess the accuracy of the magnification and defocus of the reconstructed images, and the procedure for tuning those. Subsection 3.4.4 discusses the outcome of the other reconstruction parameters not tuned to be optimal.

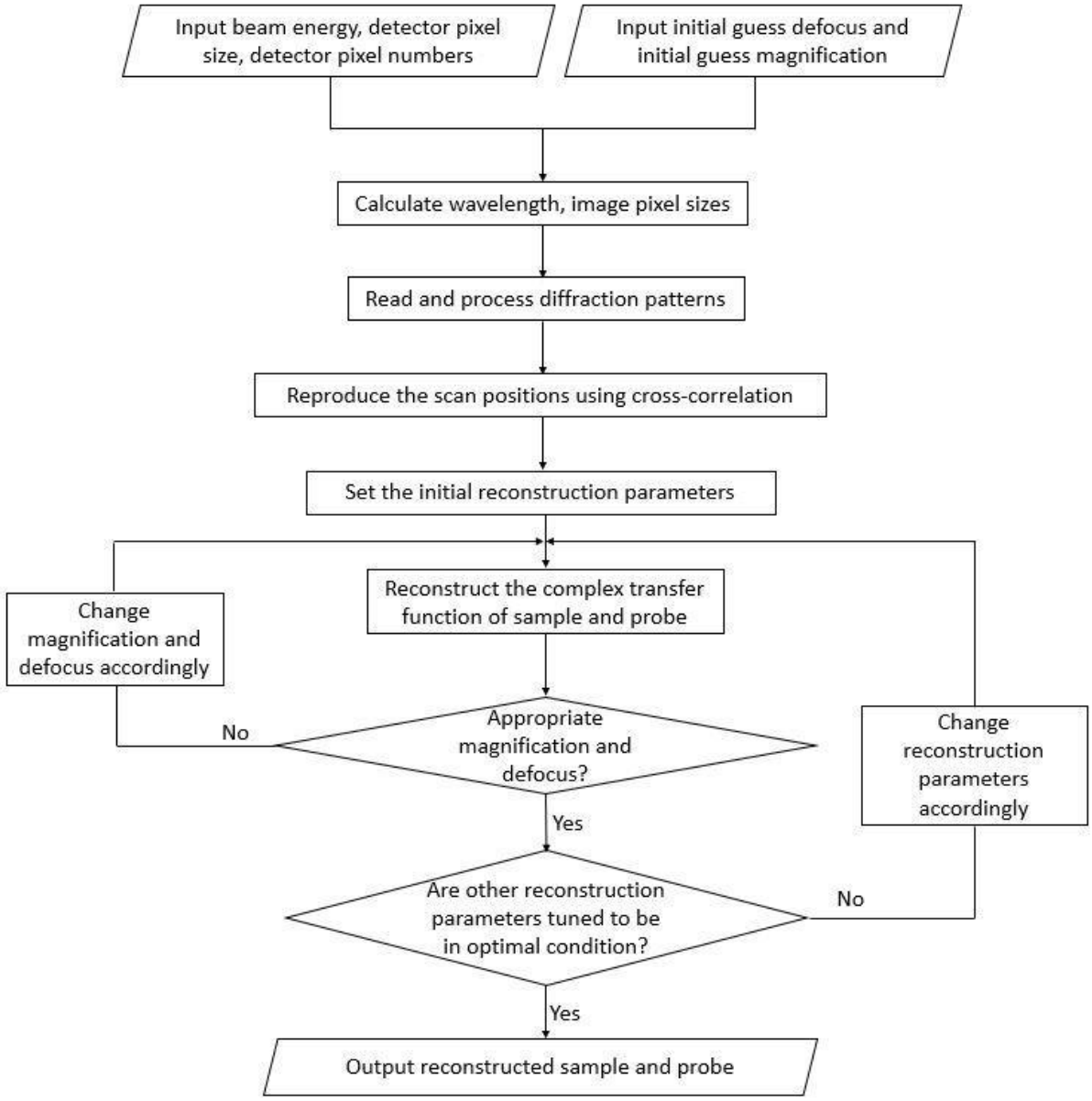

Fig 3.5. The simplified flow chart of the reconstruction process. The flow chart is carried out in MATLAB. The detail of each block is explained in the text.

The reconstruction process works as follows:

- Load the recorded experimental parameters, including beam energy, camera information, initial guess of defocus and magnification.
- Calculate the essential parameters, such as wavelength, and image pixel sizes, using loaded parameters from the previous step.
- Translate the diffraction patterns from the original Digital Micrograph images into MATLAB files.

- Define the reconstruction parameters, such as the number of iterations, etc.
- Using the modified ePIE reconstruction algorithm as explained in Chapter 2.
- Analyse the reconstructed results and adjust parameters, mainly the initial guess of defocus magnification and pedestal.
- Output the optimal results.

3.4.1 Calculation of the initial experimental parameters

Most of the experimental parameters are recorded during the data collection process. This includes electron beam energy, spot size, camera length, exposure time, scan position grid and scan step sizes. Information about the diffraction pattern can be found on the datasheet of the detector, mainly detector pixel numbers and detector pixel size. The detector used in our experiment is a K2 direct detection camera (model number 1000) with 3840 x 3712 pixels. To save storage space and have a quicker reconstruction process, each diffraction pattern is cut out to be a 2048 x 2048 pixels area with the bright field disk in the middle.

Other essential parameters, such as wavelength, image pixel sizes, defocus and sample-to-camera magnification, are calculated using the recorded parameters. In our experiment, the beam electron beam energy is 300 keV, which means the relativistic effects should be considered. Hence, the wavelength can be calculated using equation 2.5 in Chapter 2.

The image pixel sizes can be calculated using detector pixel sizes and sample-to-camera magnification, as shown in equation 3.1.

$$d_{xy} = \frac{D_{xy}}{Mag} \tag{3.1}$$

d_{xy} is the image pixel size in meters. D_{xy} is the detector pixel's physical size in meters. Mag is the sample-to-camera magnification. This equation can be understood as the pixels on the detector are shrunk down by a factor equal to the magnification. With near-field ptychography, the diffraction patterns are captured at a virtual image plane placed closely downstream of the sample. Such a particular downstream distance is equal to the defocus value. However, such defocus value cannot be precisely determined during the collection process. It has to be tuned by evaluating the reconstructed results, detail explained in sub-section 3.4.3.

The sample-to-camera magnification can be calculated by viewing the diffraction pattern. As shown in Fig 3.6.

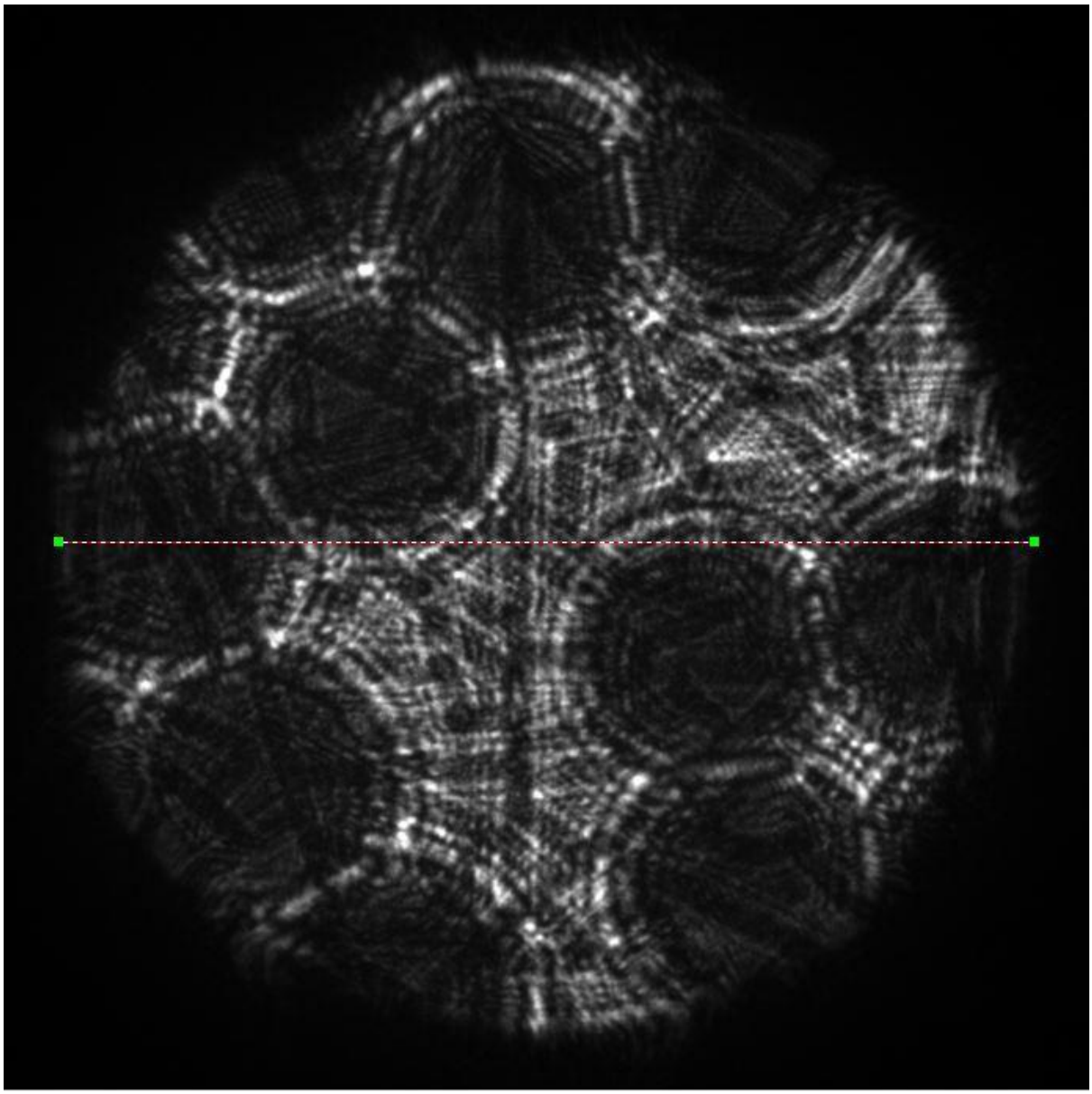

Fig 3.6. An example diffraction pattern. The dotted line measures the diameter of the bright field disk is 1841 pixels.

The physical size of the bright field disk can be calculated by the known detector pixel size multiplied by its diameter in pixels. The size of the illumination profile that produces such a diffraction pattern is recorded during the collection process. Hence, the sample-to-camera magnification can be calculated by the physical size of the bright field disk divided by the physical size of the illumination profile. However, such value is only precisely accurate providing:

- The illumination profile is carefully calibrated.
- The centre of the bright field disk is found.
- The edge of the bright field disk is identified.

All three conditions are subject to human error, especially the third condition due to the decaying edge of the bright field disk. Hence, the calculated magnification can only be considered as a reasonable initial estimate, accurate to perhaps +/- 10%. Fortunately, this is close enough for initial reconstructions to produce reasonable images from which fine-tuning can be carried out.

3.4.2 Reproducing the scan position grid.

As mentioned in previous sections, the sample is translated by lateral shifting the sample stage in a raster scan fashion. This scan position grid is recorded by the TEM, shown in Fig 3.7.

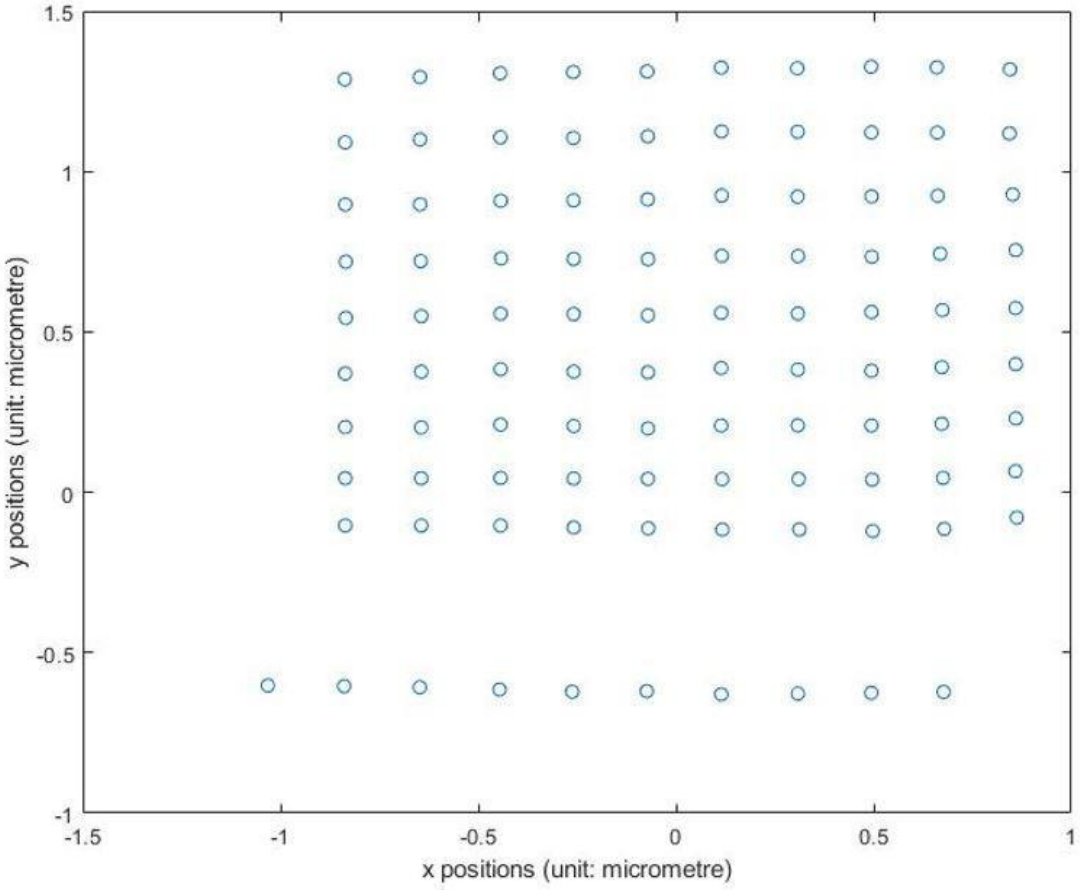

Fig 3.7. The recorded scan positions. The scan step size is 200 nm . The recorded positions are shown on a real physical scale.

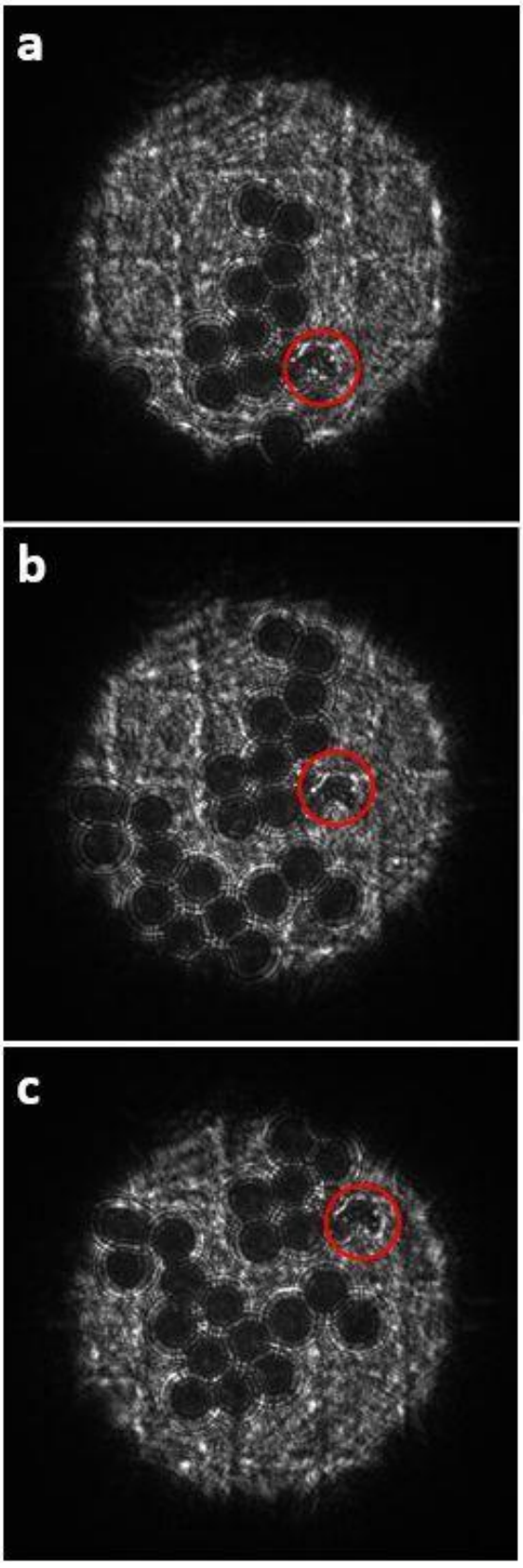

Fig 3.8. Three diffraction patterns from the same scan column from the same dataset as in Fig 3.7. (a), (b), and (c) are the second, fifth, and seventh scans in the same column. The red circles highlight the same feature.

However, after a careful inspection of the diffraction patterns, the TEM recorded position grid does not accurately describe the actual scan in two aspects:

1. TEM recorded position grid shows the illumination probe scans in horizontal and vertical directions. However, the features are moving in an incline direction, neither horizontal nor vertical, in the diffraction patterns, shown in Fig 3.8. This is due to the rotation introduced by the objective and projection lenses.
2. TEM recorded positions grid shows the scan step sizes are a near-constant value, 200 nm in Fig 3.7. After manually measuring the same feature moving trajectory, however, the first few step sizes in each scan column are much less than 200 nm , due to sample drift and stage hysteresis.

To demonstrate the first problem, three diffraction patterns from the same scan column are shown in Fig 3.8. The moving trajectory of a certain feature, highlighted with the red circle, is measured to be 13 degrees rotated from the vertical axis. Such rotation degree, however, is not shown in the TEM recorded scan position grid. This problem can easily be fixed by rotating the recorded position grid.

The variable step sizes problem, on the other hand, is difficult to correct. Due to the lack of distinguishable reference points, the accurate scan step sizes cannot be precisely determined. The extra workload makes the recorded position from the TEM not suitable for such large datasets. An alternative approach using cross-correlation to reproduce the scan positions is used instead. The procedure of the cross correlation is summarised in Fig 3.9

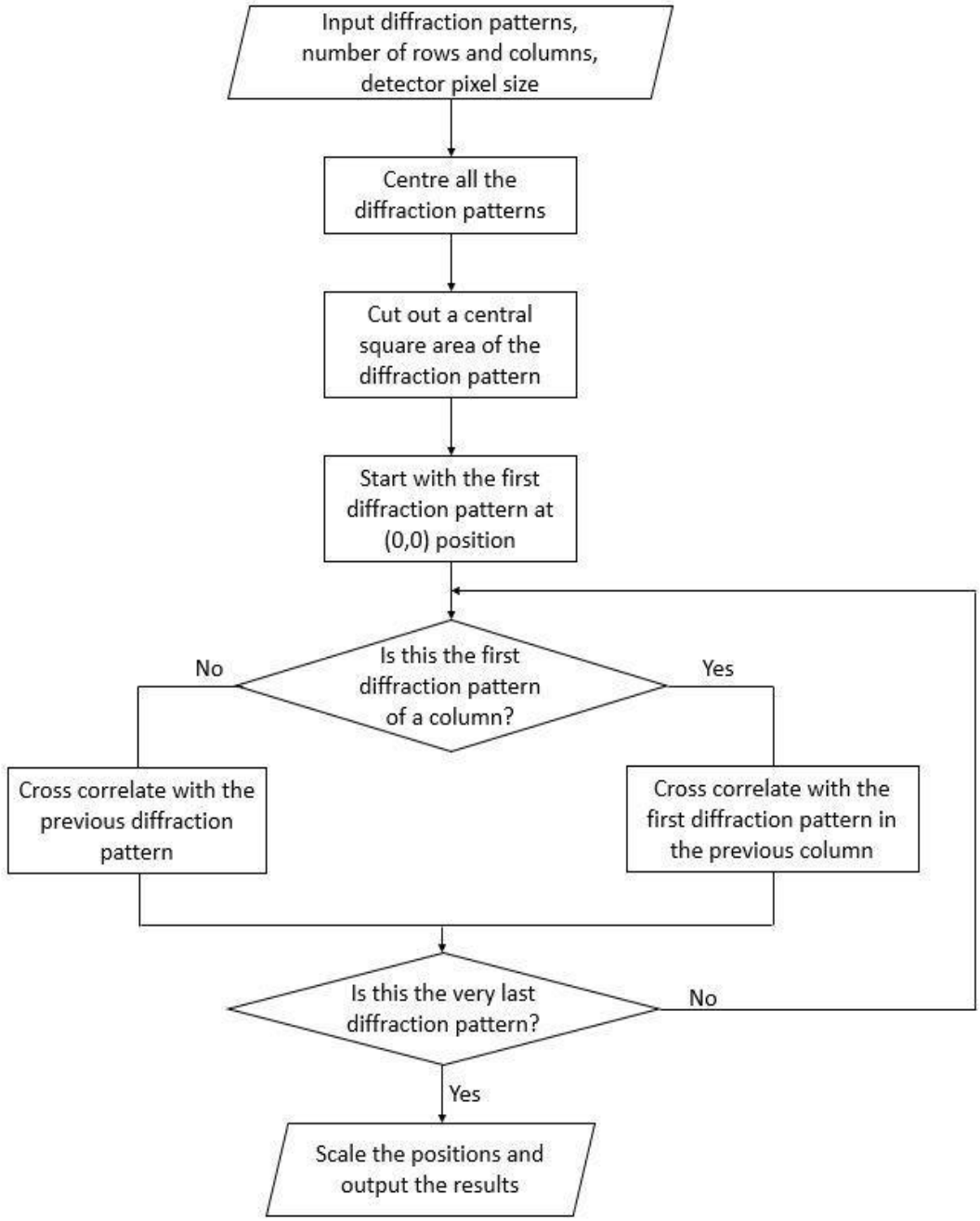

Fig 3.9. The flow chart of cross correlation to reproduce the scan position grid. Note that the very first diffraction pattern is positioned at (0,0). The cross correlation starts with the second diffraction in the first column.

As mentioned in the previous section, the data collection time for 100 diffraction patterns is around 5 minutes – due mainly to the movement and settling time of the stepper motor stage. During this long collection process, a small drift of the bright field disk is observed. Such a drifting effect has a more significant impact on the data under Lorentz mode TEM, which is discussed in Chapter 4, hence the impact and the solution of the drifting effect are explained

in the next chapter. After such drift is corrected, the central square area of the diffraction patterns is cut out to be used for cross correlation. The square area only contains the bright field disk information, avoiding the edges of the bright field disk is considered as a reference feature and used in the cross-correlation.

After the initialization process is finished, the algorithm loops through the diffraction patterns and performs cross correlation as described in Fig 3.9. Since the number of rows and columns are loaded into the algorithm at the first step, the algorithm can identify the first diffraction pattern in each column and cross correlate it with the appropriate diffraction pattern. The unit of positions produced by the cross correlation is pixels. Such units are translated into real physical size using the known camera pixel size.

To analyse the positions reproduced from the cross correlation and the effect of position errors, two reconstructions are performed. One uses the cross correlation positions, and the other uses the TEM recorded positions. All the other parameters, both experimental and reconstruction parameters, are the same. However, the original TEM recorded positions, shown in Fig 3.7, are unable to produce any reasonable images. The missing rotation is added to the recorded positions, shown in Fig 3.10b. The variable step size problem is not fixed, note the regular scan grid.

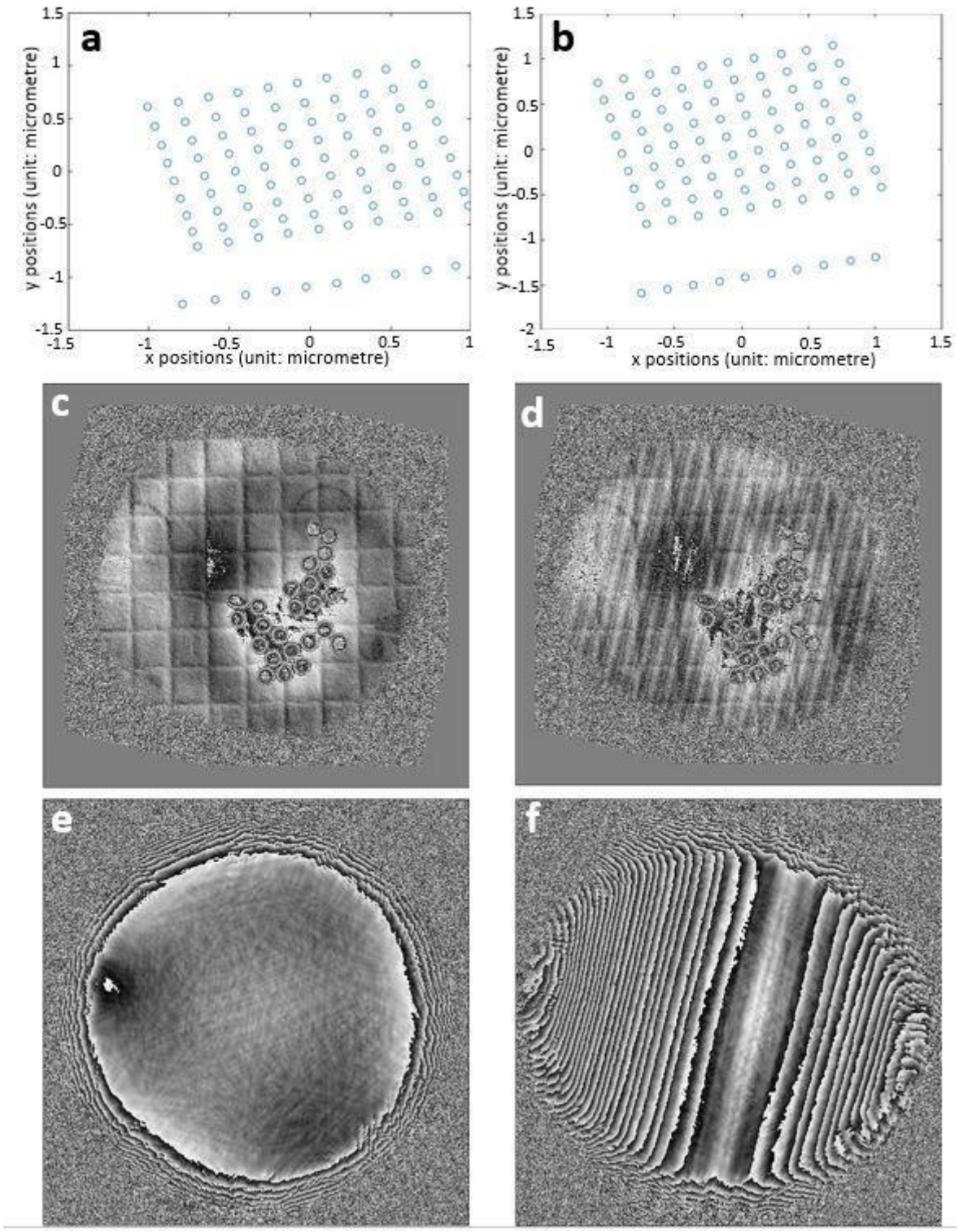

Fig 3.10. The comparison of reconstructed phase images using position from cross correlation (a) and TEM recorded position (b). (c) and (e) is the reconstructed phase images of the sample and probe using cross correlation position. (d) and (f) is the same as (c) and (f) but using TEM recorded position

Fig 3.10 shows the reconstruction results using positions from cross correlation and TEM recorded positions. The experimental and reconstruction parameters used in those two reconstructions are the same. However, at the early stage of the tuning process, those parameters are not in optimal condition.

The recorded positions have regular step sizes, while the first few steps in each column from the cross correlation positions are less than the designed 200 nm . However, the step sizes become more regular as the scan proceeds. The reconstructed sample and probe phase images using recorded positions show significant aberration. The only different condition is the variable step size, the significant difference in terms of result quality in Fig 3.10 proves such varying step size effects to be genuine.

3.4.3 Evaluate the magnification and defocus.

The most time-consuming step in the reconstruction process is to find the correct defocus and sample to camera magnification. As mentioned in the previous section, the initial values of those two parameters are merely a reasonable guess and precise values are currently found using a trial-and-error method. This procedure can be summarised as follows:

1. Find a reasonable value for defocus with the initial magnification guess.
2. Calculate the size of the latex sphere and waffle grid in the reconstruction.
3. Adjust the magnification according to the latex sphere size and waffle grid size.
4. After the magnification is correct, tune the defocus and get the best in-focus images.

Since the initial value of defocus value is a rough guess, in some cases, such value does not produce a clear image of the latex sphere. The blurred images with highly defocused latex spheres make it difficult to evaluate the accuracy of the magnification value. Hence, it is essential to tune the reasonable value. Fig 3.11 can be used as an example for this step.

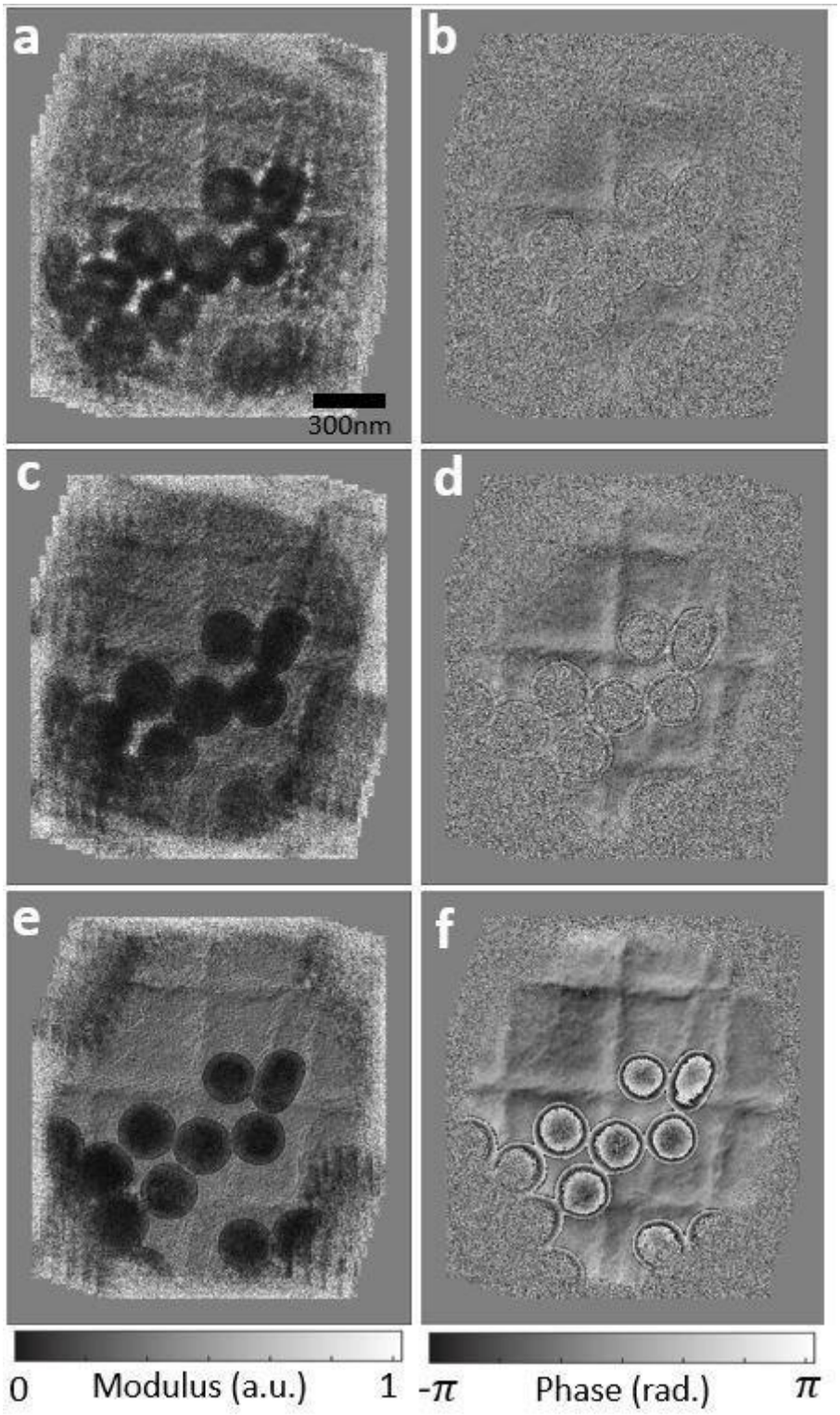

Fig 3.11. Reconstructed sample modulus and phase images with three different defocus. (a), (c), and (e) are the sample modulus images with defocus being 220 µm, 330 µm, and 420 µm. (b), (d), and (f) are the corresponding phase images. The illumination probe is 1 µm-diameter.

Fig 3.11 shows the significant impact of defocus on the reconstruction quality. The initial guess of the defocus value is around 200 µm. However, the reconstructed images are of poor quality, as shown in Fig 3.11, (a) and (b). The latex spheres can be barely recognised, and the waffle grid, which is the gold-shadowed carbon background, is completely masked by the defect. The measured latex sphere size from such images is highly doubtable to be used. With the defocus being 330 µm, as shown in Fig 3.11, (c) and (d), both the latex sphere and waffle grid can be recognised. However, the Fresnel fringes around the latex sphere indicate the defocus is still not correct. And the actual latex sphere sizes are difficult to determine, due to such fringes. With the correct defocus, shown in Fig 3.11 (e) and (f), the latex spheres are in focus with the edges being sharp. The waffle grid can be recognised. The measured sizes in such conditions are reliable and can be compared to their designed sizes. The comparison between the measured and designed sizes will determine whether the current magnification is correct.

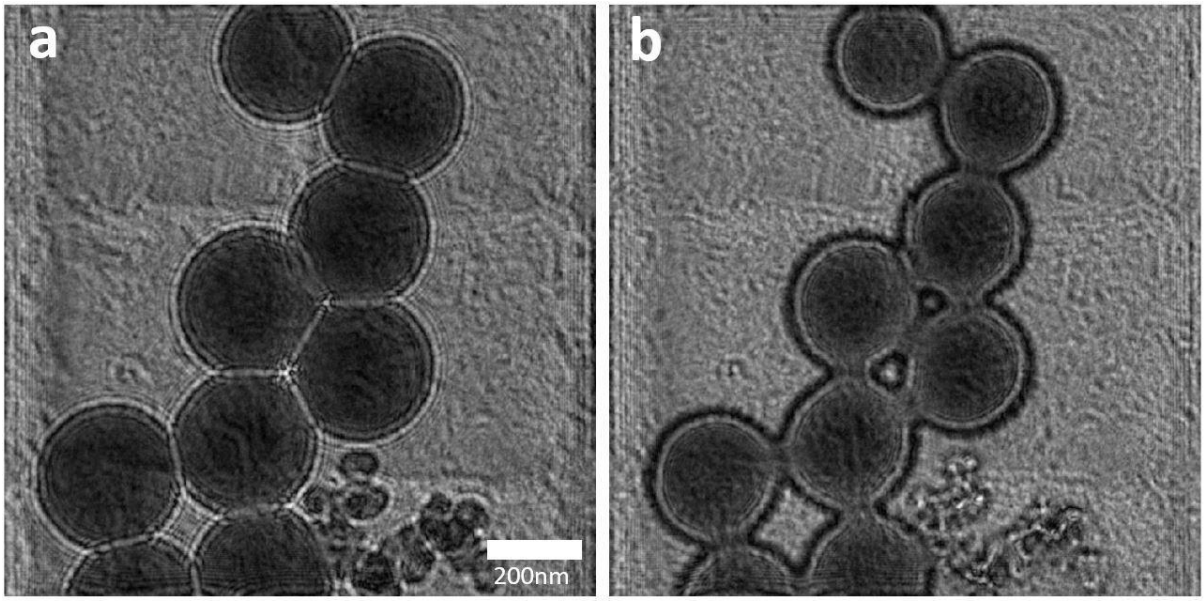

Fig 3.12. Two images indicate whether to increase or decrease the defocus.

While tuning the defocus value, knowing whether to increase or decrease the defocus is important, as this can prevent tuning the value in the wrong direction and wasting time. Fig 3.12 (a) has Fresnel fringes wrapping around the latex sphere, similar to Fig 3.11 (c), indicating the correct defocus value is larger than the current value. Fig 3.12 (b) has black rings wrapping around the latex sphere, indicating the correct defocus value is smaller than the current value.

However, it is difficult to determine how much smaller or larger to tune. Such differences can only be determined by trial-and-error method, as it is subject to magnification.

After the correct defocus value is found with the initial magnification. The magnification is evaluated by measuring the size of the latex sphere and waffle grid. As mentioned in previous sections, the diameters of the latex sphere and waffle grid are 263 nm and 463 nm respectively. After some test tunes, it is found that if the measured sizes are larger than such value, then the magnification should be tuned down, and vice versa.

However, the problem is that this patch of the sample is not perfectly built. The latex spheres have variable sizes, as shown in Fig 3.13. The waffle grid background, on the other hand, is much more constant in size. However, the edge of such a grid cannot be precisely determined. Hence, an average of the latex sphere sizes, and the size of the waffle grid as a second reference are used to evaluate the magnification, as shown in Fig 3.13.

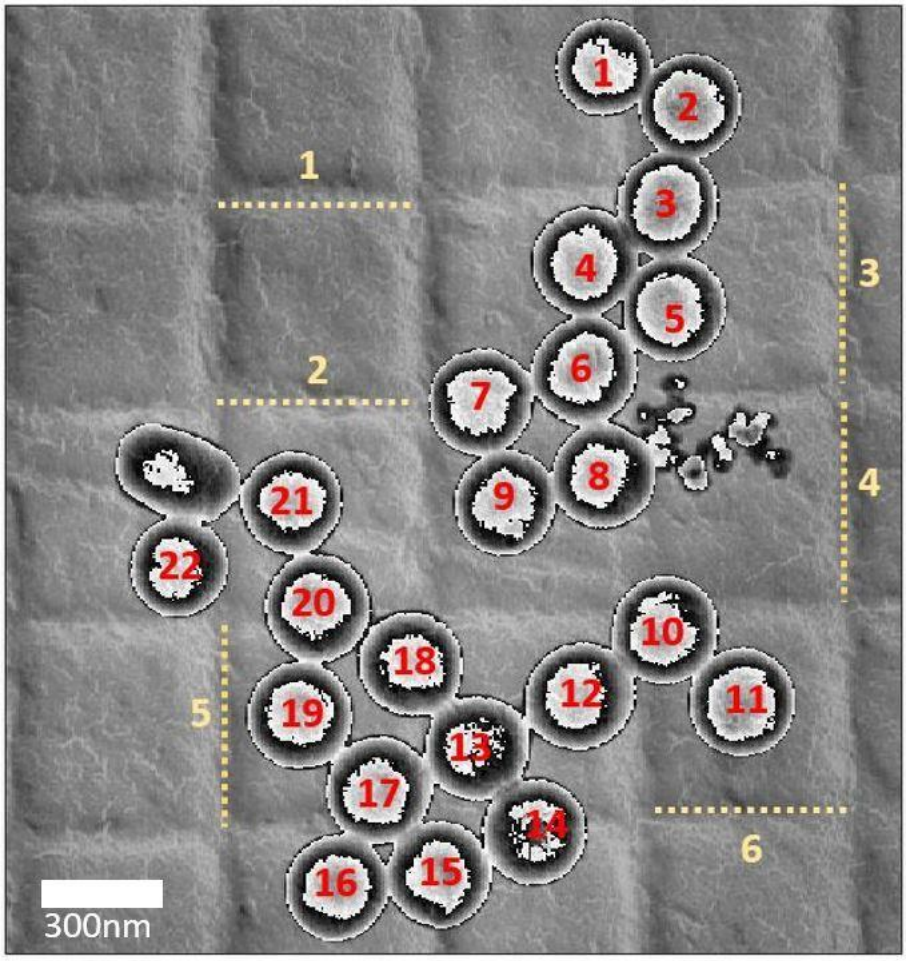

Fig 3.13. The phase reconstruction of the latex sphere sample. The latex spheres and the waffle grid are used to evaluate the magnification.

Latex spheres number	Latex sphere sizes Unit: nm	Waffle grid number	Waffle grid sizes Unit: nm
1	252	1	465
2	258	2	462
3	265	3	472
4	265	4	460
5	262	5	463
6	261	6	465
7	255		
8	259		
9	255		
10	255		
11	255		
12	265		
13	261		
14	262		
15	261		
16	261		
17	260		
18	263		
19	265		
20	265		
21	256		
22	252		

Table 3.1. The diameter of the latex spheres and the waffle grids, from Fig 3.12.

The average diameter of the latex spheres shown in Fig 3.13 is 259.68 nm, close to the designed 263 nm. The measured waffle grid diameters are close to the designed value of 463 nm.

After the magnification is tuned to be a reasonable value, similar to Fig 3.13, the defocus needs to be recalibrated. Fortunately, the previous defocus value with initial magnification guess is not far away from the correct value, providing the magnification has not been significantly changed. But adjustments need to be made. This step follows the same procedure as the previous defocus value tuning.

3.4.4 Reconstruction parameters tuning .

After the defocus and magnification values are determined, the next step is to find the most suitable reconstruction parameters. These parameters include the number of iterations, object and probe update starting point, and background noise threshold. Those parameters are tuned based on one criterion, to make sure the reconstruction converges to the solution of the complex transfer function of both object and probe (Maiden and Rodenburg 2009).

The number of iterations is set to 500. Most of the datasets converge before 150 iterations. Benefiting from the improved spatial frequency spectrum, the datasets using the diffuser with the random curved-line design converge quicker than the ones with the straight-line design.

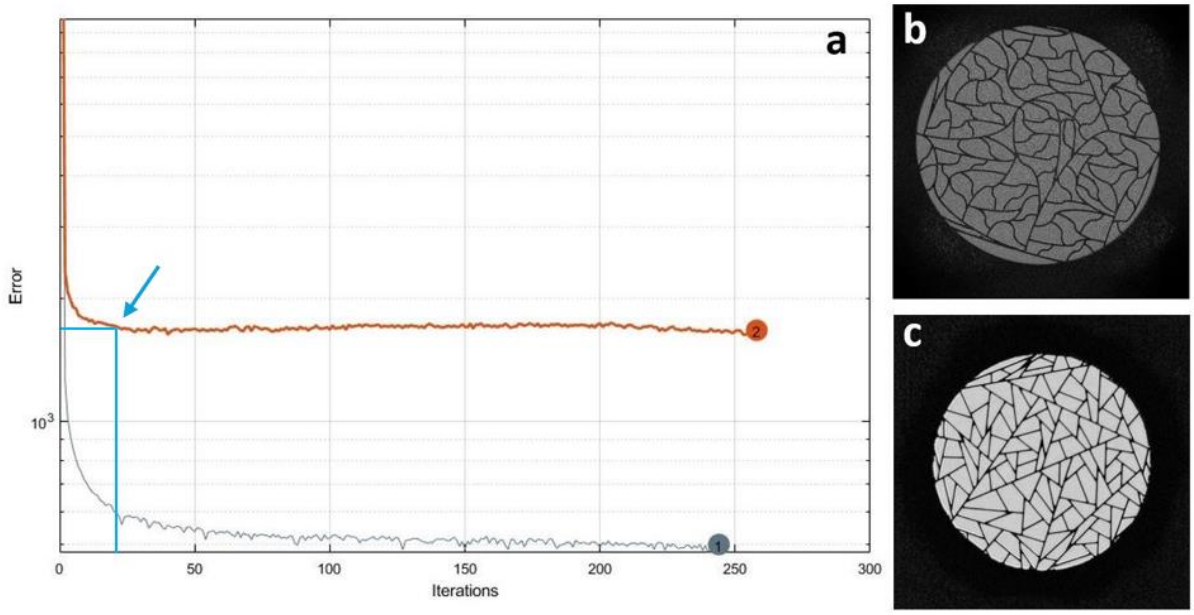

Fig 3.14. Reconstruction speed comparison. Both datasets use 1 µm illumination probe, with 200 nm step sizes. Dataset 1 uses the diffuser with the straight-line design, shown in (c). Dataset 2 uses the diffuser with the curved-line design, shown in (b). When reconstruction process with curve-line design reached local minimum (indicated by the blue arrow), the one with straight-line design was still converging.

Fig 3.14 (a) shows the error plot of two reconstructions. The error plot measures the difference between the modelled diffraction pattern with the recorded diffraction pattern. It is commonly used as a tool to indicate whether the reconstruction has converged (Maiden and Rodenburg, 2009). Two datasets, 1 and 2 from Fig 3.14 (a), have the same experimental parameters, including illumination size, step size, number of diffraction patterns, etc. The difference is that dataset 1 uses the amplitude diffuser with the straight-line design, shown in Fig 3.14 (c), while dataset 2 uses the one with the curved-line design, shown in Fig 3.14 (b). As mentioned in section 3.2, the curved-line design improves the spatial frequency of the Fresnel fringes. As a result, datasets with such a diffuser design are easier to reconstruct.

The object and probe update starting point is an option function that holds the object or the probe as the initial guess and updates those after certain iterations. With datasets in this chapter, which are easy to reconstruct, this option function is not used. However, at the early stage of reconstructing the magnetic sample, this function is used to form a reasonable initial image of the sample with a constant probe, details of which are discussed in the next chapter.

One important step before the reconstruction is to remove the background noise. The threshold method (Hou, Wang et al. 2018) is implemented. With this method, a constant value of intensity, or a pedestal, is removed from the recorded datasets. The critical part is to estimate the noise level, or the amount of intensity to be removed from the diffraction pattern.

First, an average diffraction pattern using all the diffraction patterns is calculated. Then, a background area is cut out to analyse the noise level. In our cases, a 100 x 100 pixels corner area of the average diffraction pattern is used, shown in Fig 3.15 (b). To quantitatively analyse the noise level, an area from the bright field disk of the same size is cut out, as shown in Fig 3.15 (c).

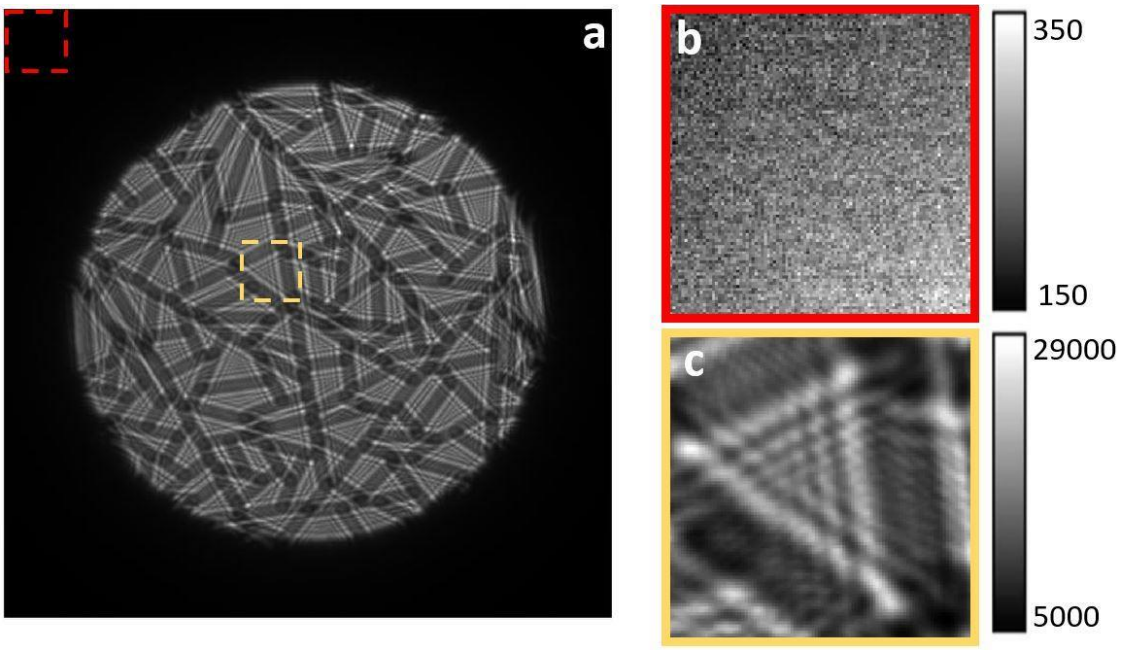

Fig 3.15. (a) an example of the average diffraction pattern. The corner at the top left area, highlighted by the red square, is used to analyse the background noise, shown in (b). A bright field area, highlighted by the yellow square, is cut out and compared with the intensity of the background area, shown in (c).

As shown in Fig 3.15, the intensity of the background area ranges from 150 to 350, while the intensity of the bright field disk area ranges from 5000 to 29000. Even though the noise has much less intensity than the bright field disk, the removed intensity, or the pedestal, cannot be the maximum noise level. A large pedestal will result in an uneven background image. A small pedestal does produce a uniform background. But it gives a bad signal-to-noise ratio. Detail shown in Fig 3.16.

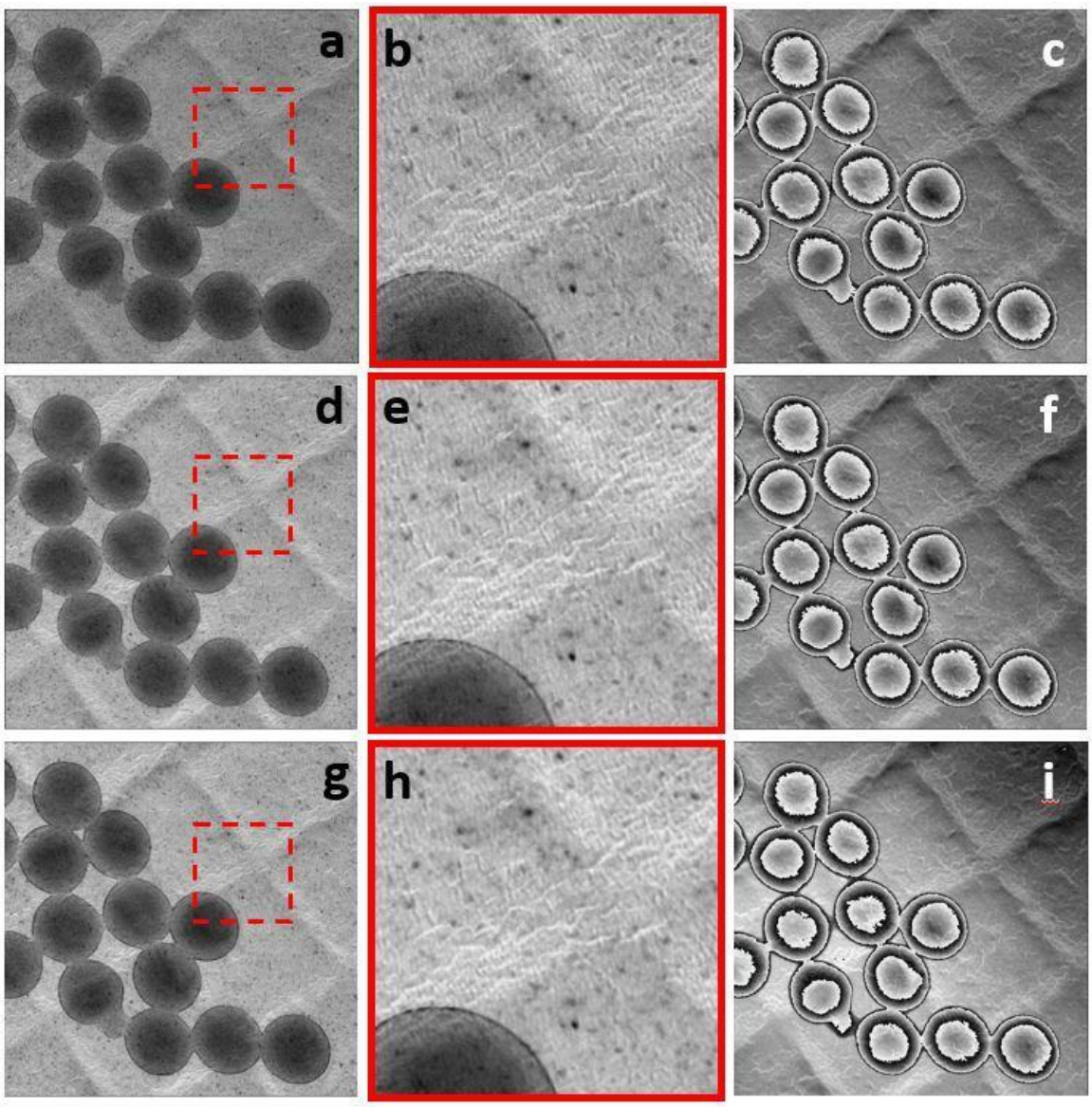

Fig 3.16. Reconstructed sample images with different pedestal levels. The first column shows the modulus images. The second column shows the enlarged modulus detail, from the red square highlighted area in the first column. The third column shows the phase images. The first row has a pedestal level being 60. The second row has a pedestal level being 190. The third row has a pedestal level being 350.

As shown in Fig 3.16 (b), (e) and (h), the noise of the reconstructed images significantly decreases with the increasing pedestal level. However, Fig 3.16 (c), (f) and (i) shows that the background of the reconstructed phase images contains low spatial frequency artefacts, especially around the polystyrene spheres; we are currently uncertain as to the source of this effect, hence, a compromise value needs to be found for each dataset that minimises both noise and the low spatial frequency phase effect.

3.5 Reconstruction results.

This section shows the final reconstructed sample and probe images after following the tuning and optimisation steps detailed above. As mentioned, two designs of amplitude diffusers are used. Each diffuser is used to conduct three different illumination-size experiments. And each illumination size experiment uses two step sizes, 10% and 20% of corresponding illumination sizes. A total of 12 results are presented in this section.

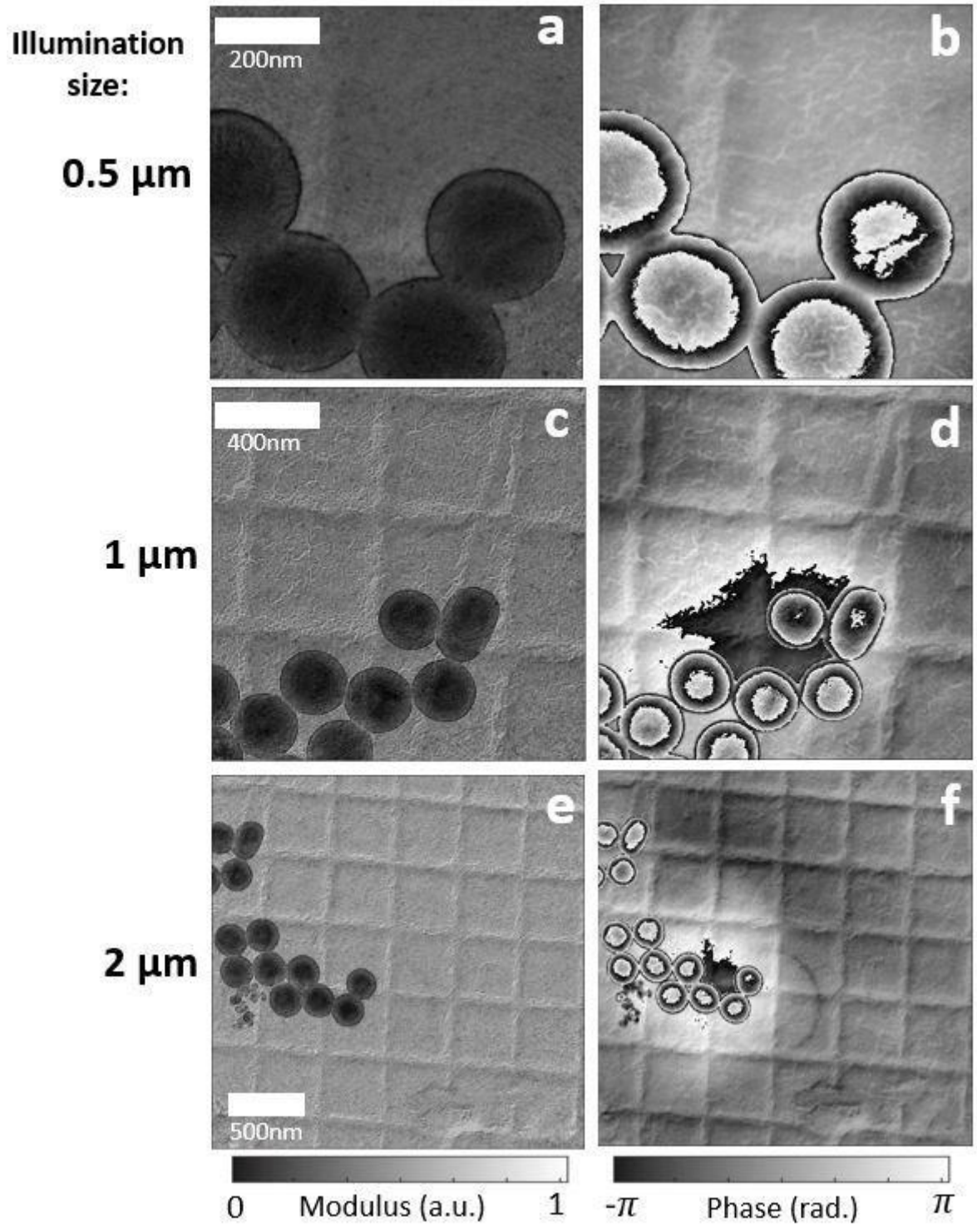

Fig 3.17. ***Sample*** *transfer function reconstruction results. The amplitude diffuser has the* ***straight-line*** *design. The left column is modulus images, and the right column is phase images. The step sizes are* ***10%*** *of the corresponding illumination sizes.*

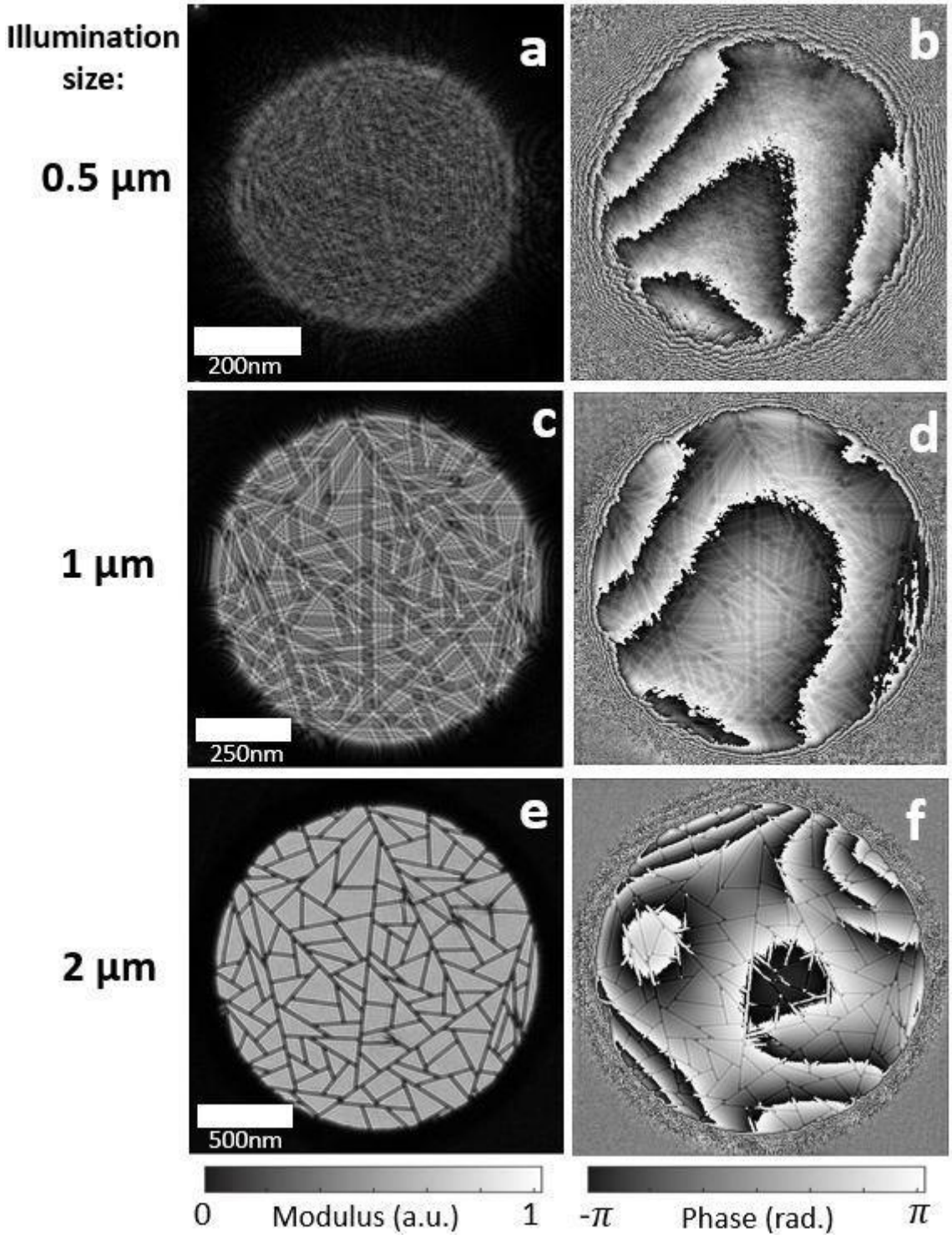

Fig 3.18. ***Probe*** *transfer function reconstruction results. The experimental parameters of this dataset are the same as the results shown in Fig 3.17. The amplitude diffuser has the* ***straight-line*** *design. The left column is modulus images, and the right column is phase images. The step sizes are* ***10%*** *of the corresponding illumination sizes.*

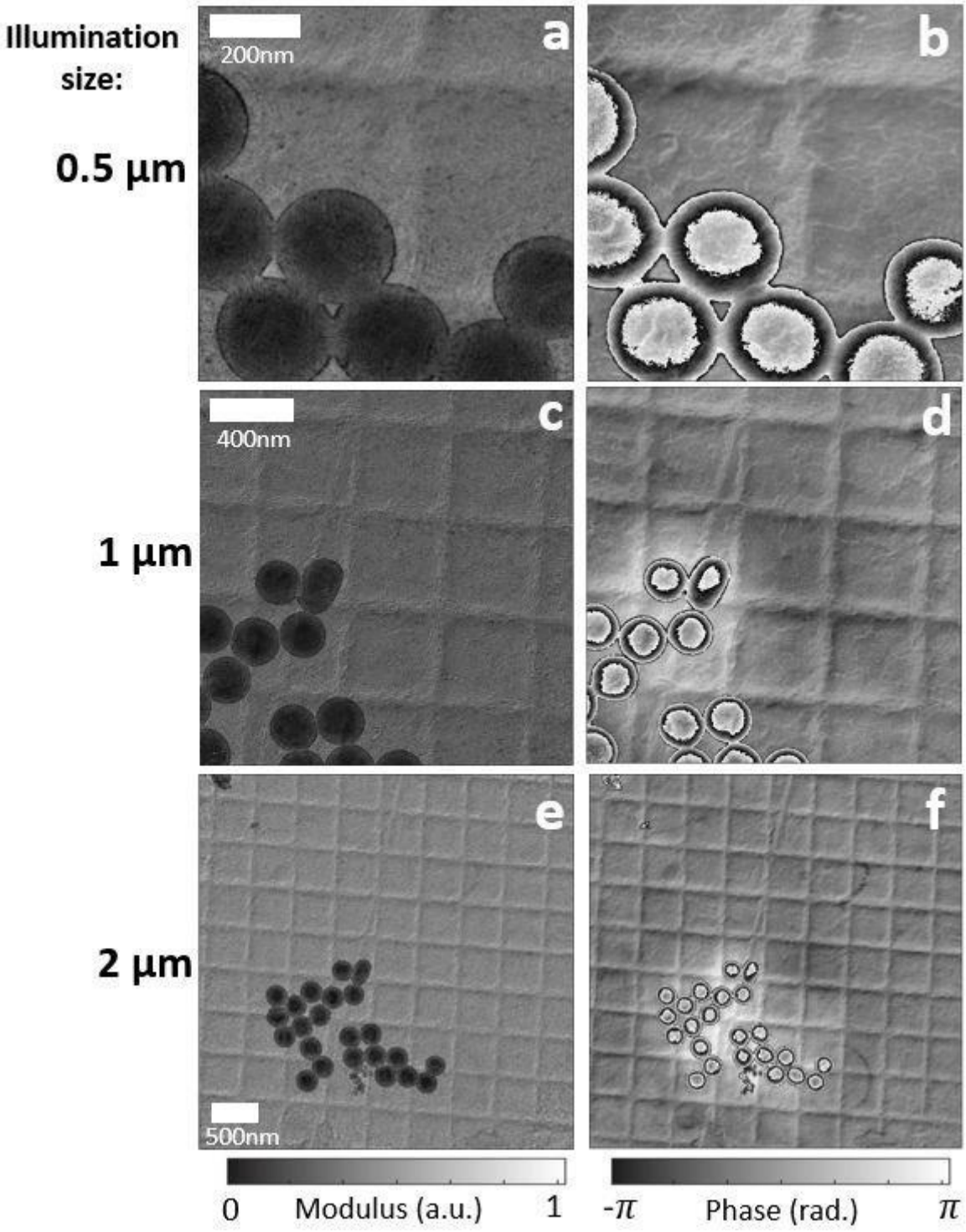

Fig 3.19. ***Sample*** *transfer function reconstruction results. The amplitude diffuser has the* ***straight-line*** *design. The left column is modulus images, and the right column is phase images. The step sizes are* ***20%*** *of the corresponding illumination sizes.*

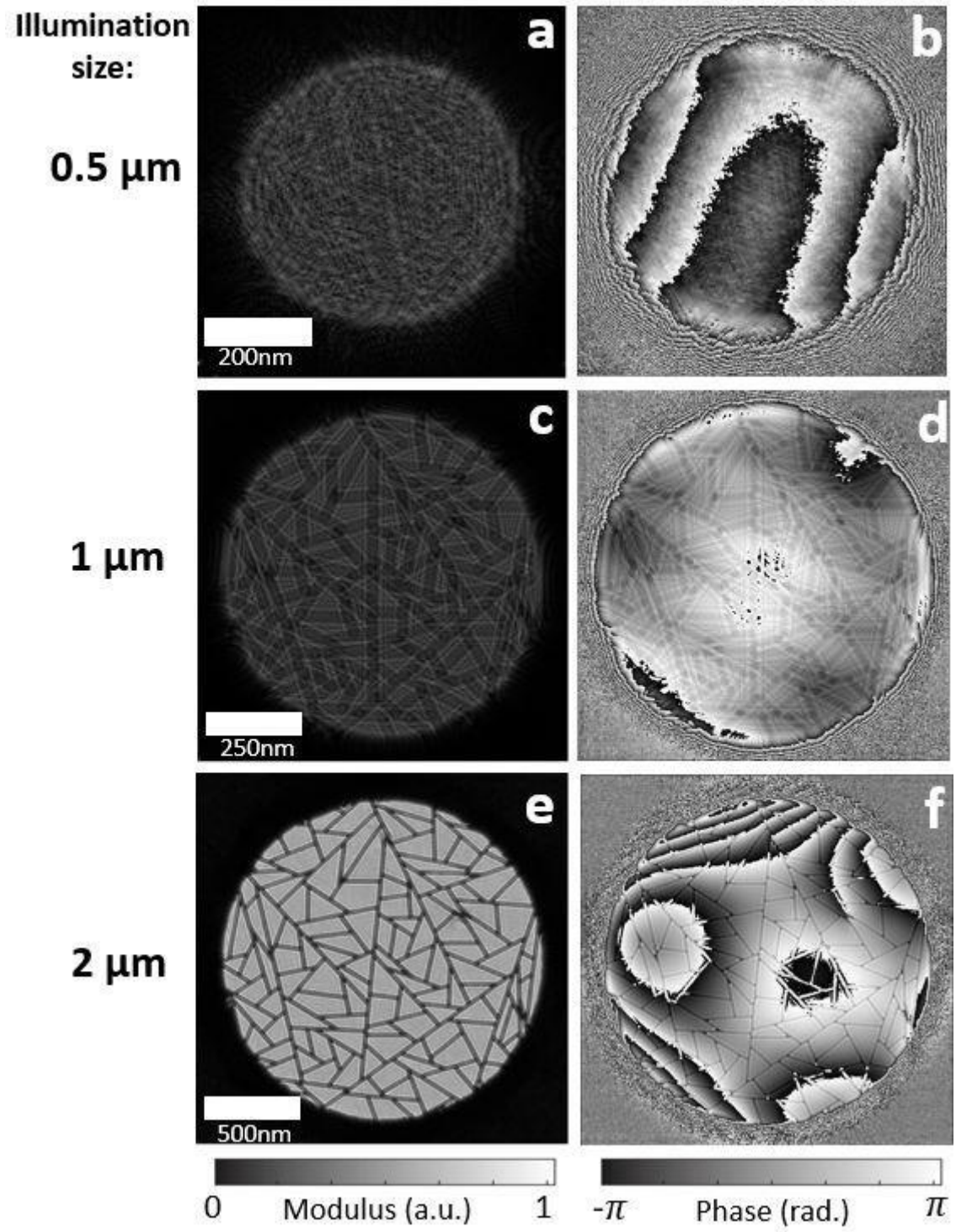

Fig 3.20. ***Probe*** *transfer function reconstruction results. The experimental parameters of this dataset are the same as the results shown in Fig 3.19. The amplitude diffuser has the* ***straight-line*** *design. The left column is modulus images, and the right column is phase images. The step sizes are* ***20%*** *of the corresponding illumination sizes.*

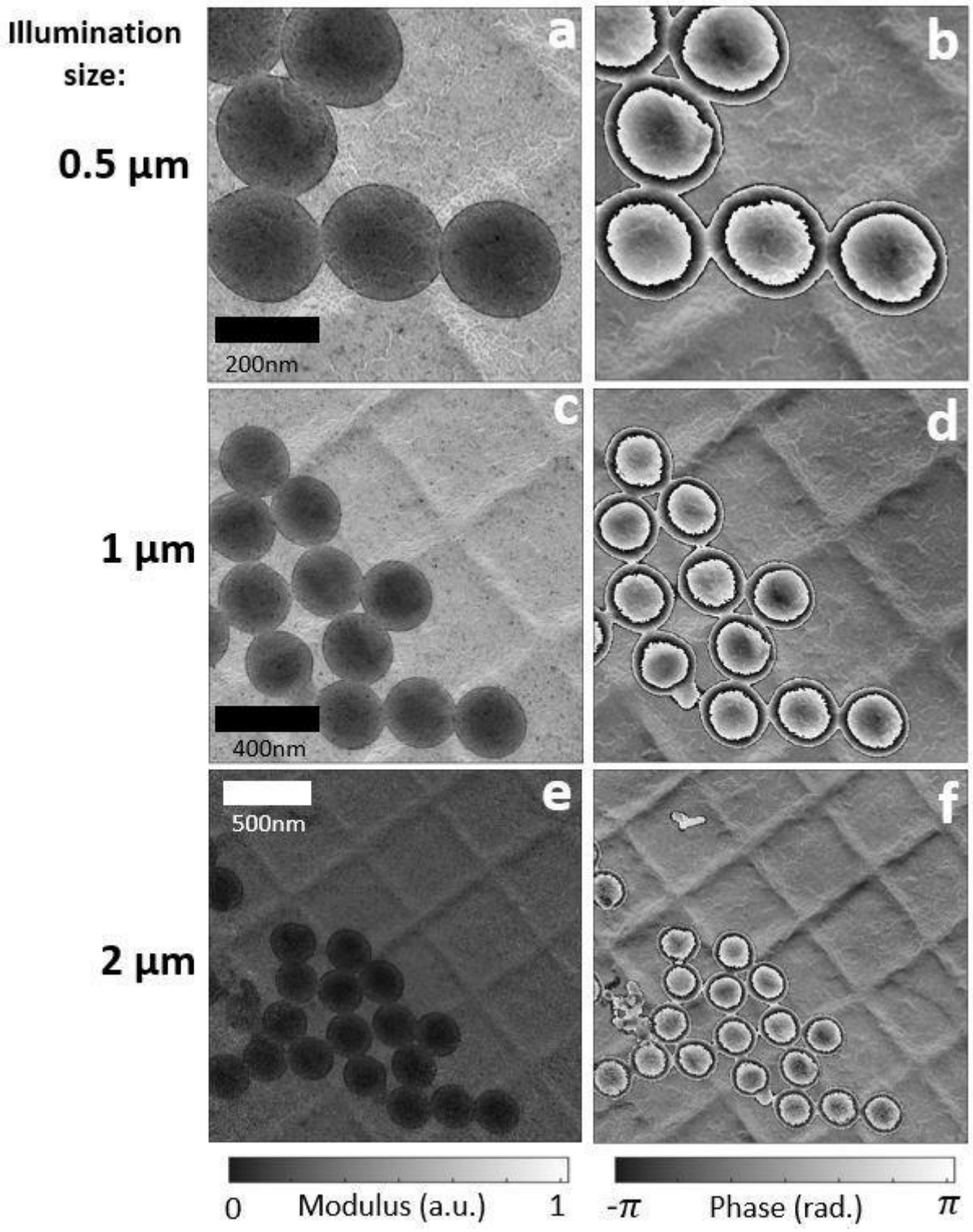

Fig 3.21. ***Sample*** *transfer function reconstruction results. The amplitude diffuser has the* ***curved-line*** *design. The left column is modulus images, and the right column is phase images. The step sizes are* ***10%*** *of the corresponding illumination sizes.*

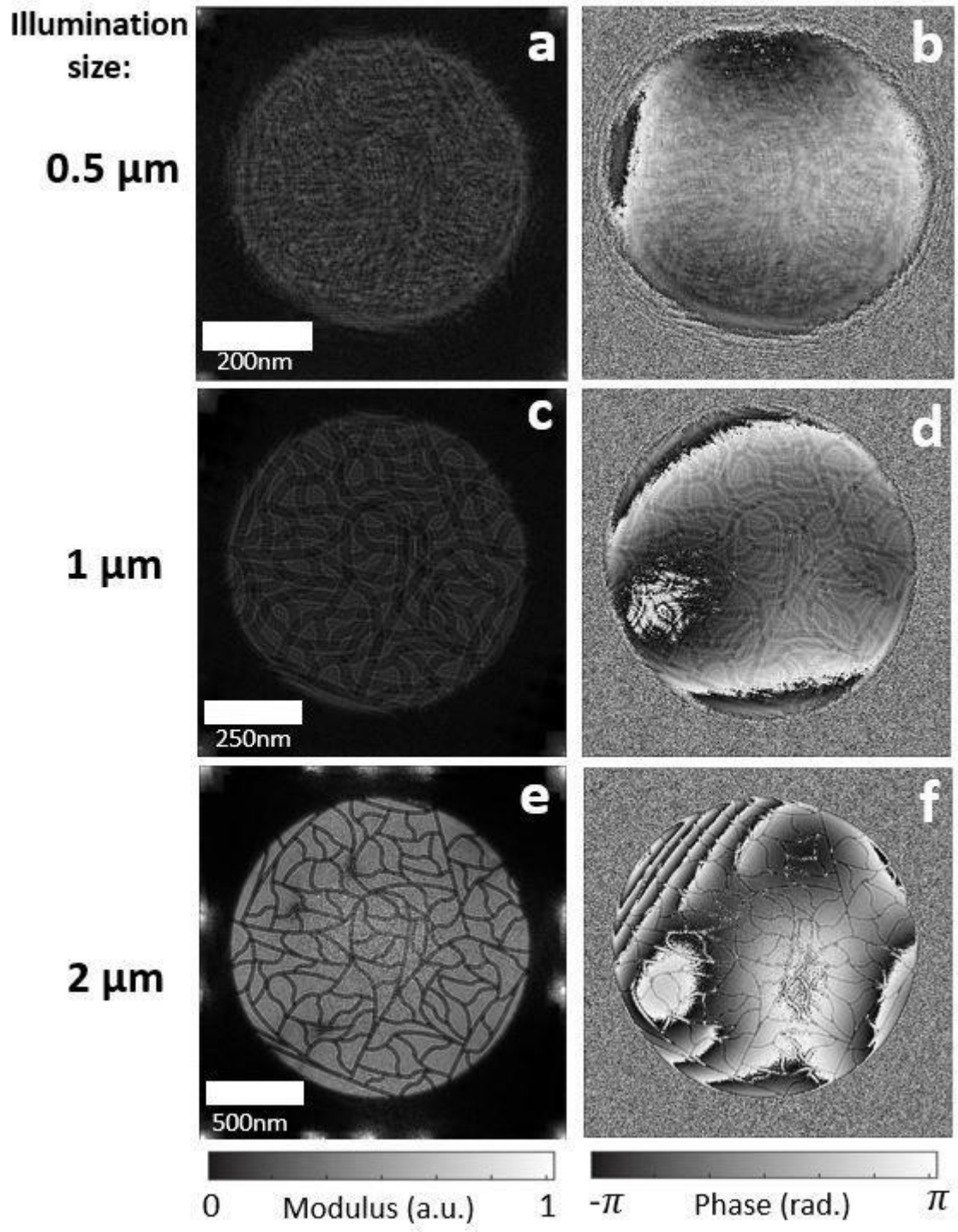

Fig 3.22. ***Probe*** *transfer function reconstruction results. The experimental parameters of this dataset are the same as the results shown in Fig 3.21. The amplitude diffuser has the* ***curved-line*** *design. The left column is modulus images, and the right column is phase images. The step sizes are* ***10%*** *of the corresponding illumination sizes.*

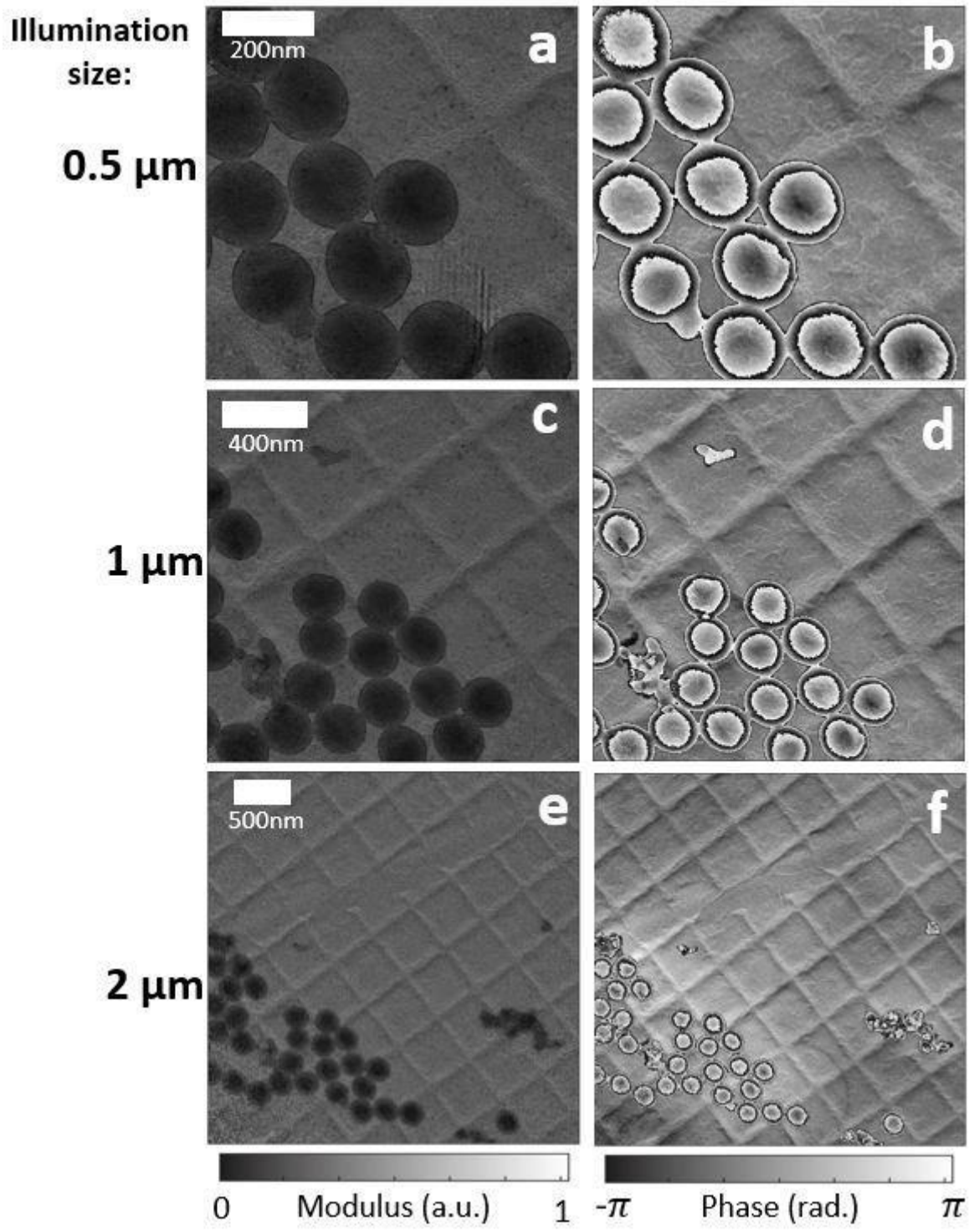

Fig 3.23. ***Sample*** *transfer function reconstruction results. The amplitude diffuser has the* ***curved-line*** *design. The left column is modulus images, and the right column is phase images. The step sizes are* ***20%*** *of the corresponding illumination sizes.*

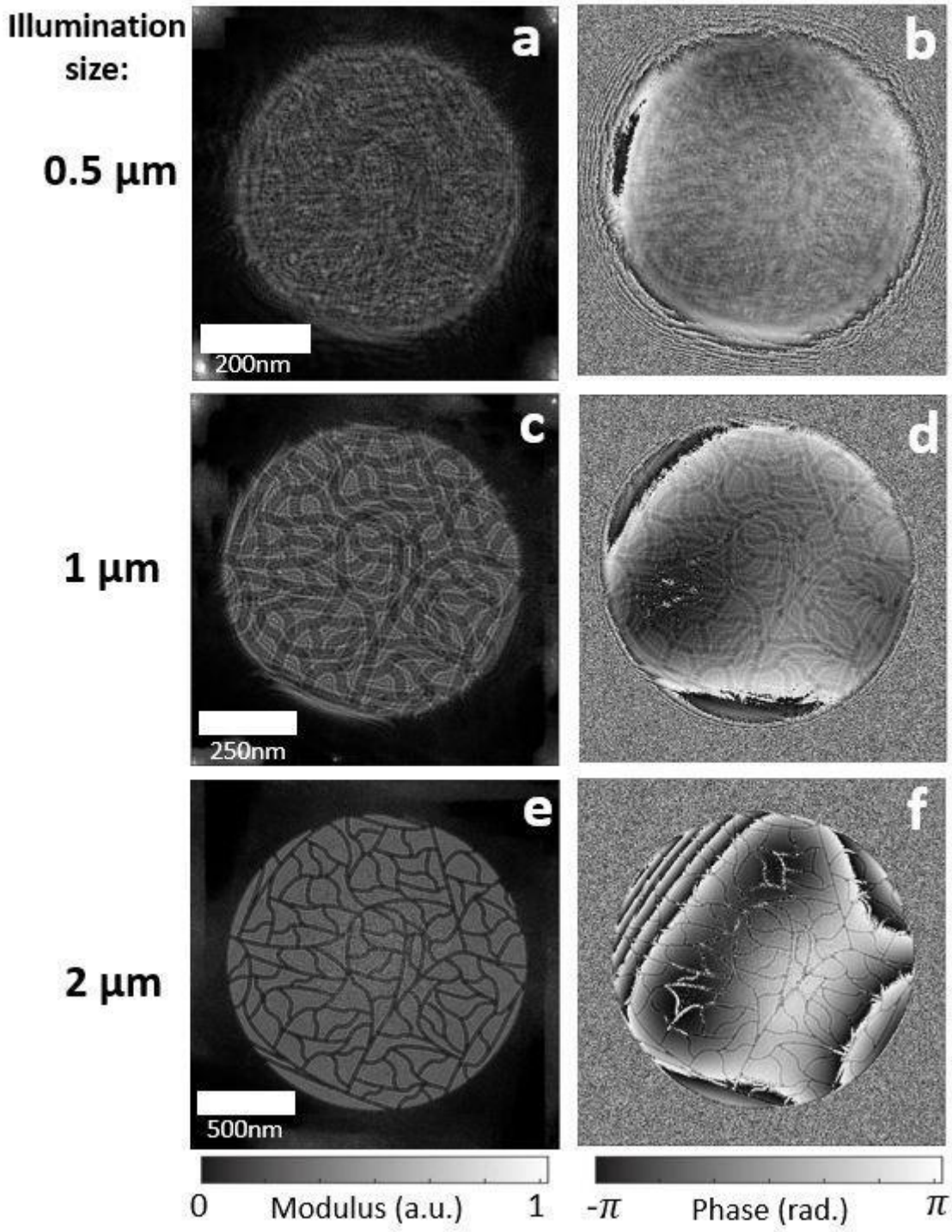

Fig 3.24. ***Probe*** *transfer function reconstruction results. The experimental parameters of this dataset are the same as the results shown in Fig 3.23. The amplitude diffuser has the* ***curved-line*** *design. The left column is modulus images, and the right column is phase images. The step sizes are* ***20%*** *of the corresponding illumination sizes.*

3.6 Discussion and Conclusion

This chapter demonstrates the proof of principle experiments that with the amplitude diffuser inserted at the condenser lens aperture to structure the illumination probe, the near-field electron ptychography is capable of recovering the complex transfer function of both sample and probe with variable illumination sizes. A Fourier Ring Correlation (FRC) (Van Heel, et al. 1982, Saxton, Baumeister, 1982) was used to assess the resolution of our results. To do this, the diffraction patterns from each experiment were split into two subsets (the odd and even patterns) and two independent reconstructions were generated. The FRC was calculated from the 600 × 600 pixels central area of the two resulting phase images. The half-bit threshold was used as a resolution measure, an example is shown in Fig 3.25.

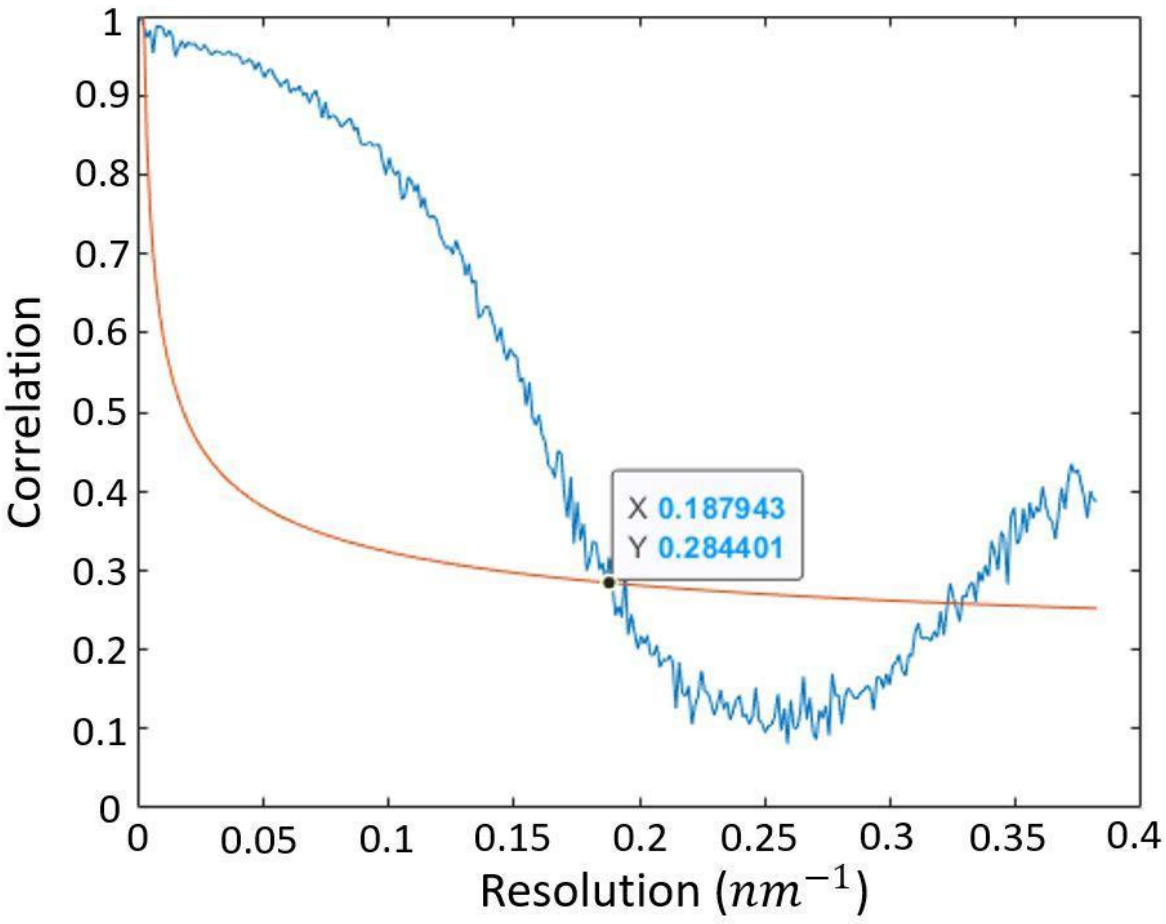

Fig 3.25. An example FRC, the half-bit threshold intersects the FRC curve at a frequency of $0.1879nm^{-1}$, corresponding to a resolution of 5.32nm.

Fig 3.25 is the FRC results with the curved-line design amplitude diffuser, illumination size being 1 µm and step sizes being 10% of illumination size. The resolution in our experiments is mostly affected by the illumination sizes. The step size and the design pattern of the amplitude diffuser (straight-line design or curved-line design) do not have a significant impact on the resolution. The resolution of datasets with illumination sizes of 0.5 µm, 1 µm, and 2 µm are around 3nm, 5nm and 10 nm respectively. Our new configuration does not significantly improve the resolution compared to the previous phase diffuser near-field ptychography (Allars, Lu et al. 2021).

Looking into the details of our results, the first problem is the phase wrap in the reconstructed phase map of the sample and probe, in Fig 3.17 and Fig 3.18. The area that has these phase wraps were scanned again in another datasets, and the reconstructed results in the second datasets do not have the same phase wraps, in Fig 3.19. Hence, it can be concluded that the appearance of these phase wraps is due to the reconstruction parameters are not tuned to be in optimal state. I suspect that one of the reasons for such artifacts is that the diffraction patterns drifting problem is not completely corrected. The result shown in Fig 3.17 is the first dataset that we reconstructed. The drifting problem is not properly corrected. As the diffraction patterns are centred repeatedly, the phase wraps in the reconstructed phase map disappear. This can be proved by carefully centring the diffraction patterns in those three datasets and repeating the reconstruction again. However, due to the limited remaining time of my PhD period, I do not have time to prove this idea.

As for the reconstructed probes, those with different illumination sizes are in different defocus states. This is due to the fact that the illumination probes with different sizes are produced using the same amplitude diffuser (50µm diameter). The condenser lenses and upper objective lens are tuned to be in different strengths so that the parallel illumination from a fixed aperture will be projected onto the specimen with different sizes. In the process, the magnification and defocus value are different according to the assigned illumination size. Hence, the reconstructed probes are also in different magnified and defocus states.

Another artefact is that phase images of the probe also have significant phase wraps, especially the 2µm-illumination sizes datasets. The possible reason for this artefact is that the reconstruction assumes the illumination is in an aberration-free condition.

Chapter 4. Near-field electron ptychography in Lorentz TEM mode

Chapter 3 discussed the implementation of near-field electron ptychography in the conventional TEM mode. By moving the diffuser from the SAA to the condenser lens aperture, there is no longer a requirement for the objective lens to form an image of the specimen at the SAA plane. This opens up the possibility of implementing this design in Lorentz TEM mode, where the objective lens is turned off.

Lorentz mode is commonly used to examine magnetic samples. Magnetic samples require a field-free environment so that the intrinsic magnetic feature of the sample is not affected by the magnetic field from the objective lens. The combination of Lorentz mode with far-field ptychography has been explored (Chen, Turgut et al. 2022), as discussed in Chapter 1. In that paper, with the objective lens being turned off, far-field ptychography can produce the results reaching a sub-nanometre resolution. The resolution from near-field ptychography is estimated to be 10 nm. However, our method holds the merits of imaging a large field of view with far fewer diffraction patterns.

This chapter is arranged as follows. Most of the configurations, including the amplitude diffusers, are the same as the previous conventional TEM experiment, but the small differences in experimental conditions are discussed in section 4.1. In terms of the reconstruction process, the procedure and algorithm are the same as the previous reconstruction. However, the cross-correlation step requires modification to reproduce the

scan position grid, as mentioned in the previous chapter. Such modification, together with other tailored functions for magnetic sample reconstruction, is discussed in section 4.2. The results and analysis are shown in section 4.3.

4.1. Experimental configuration

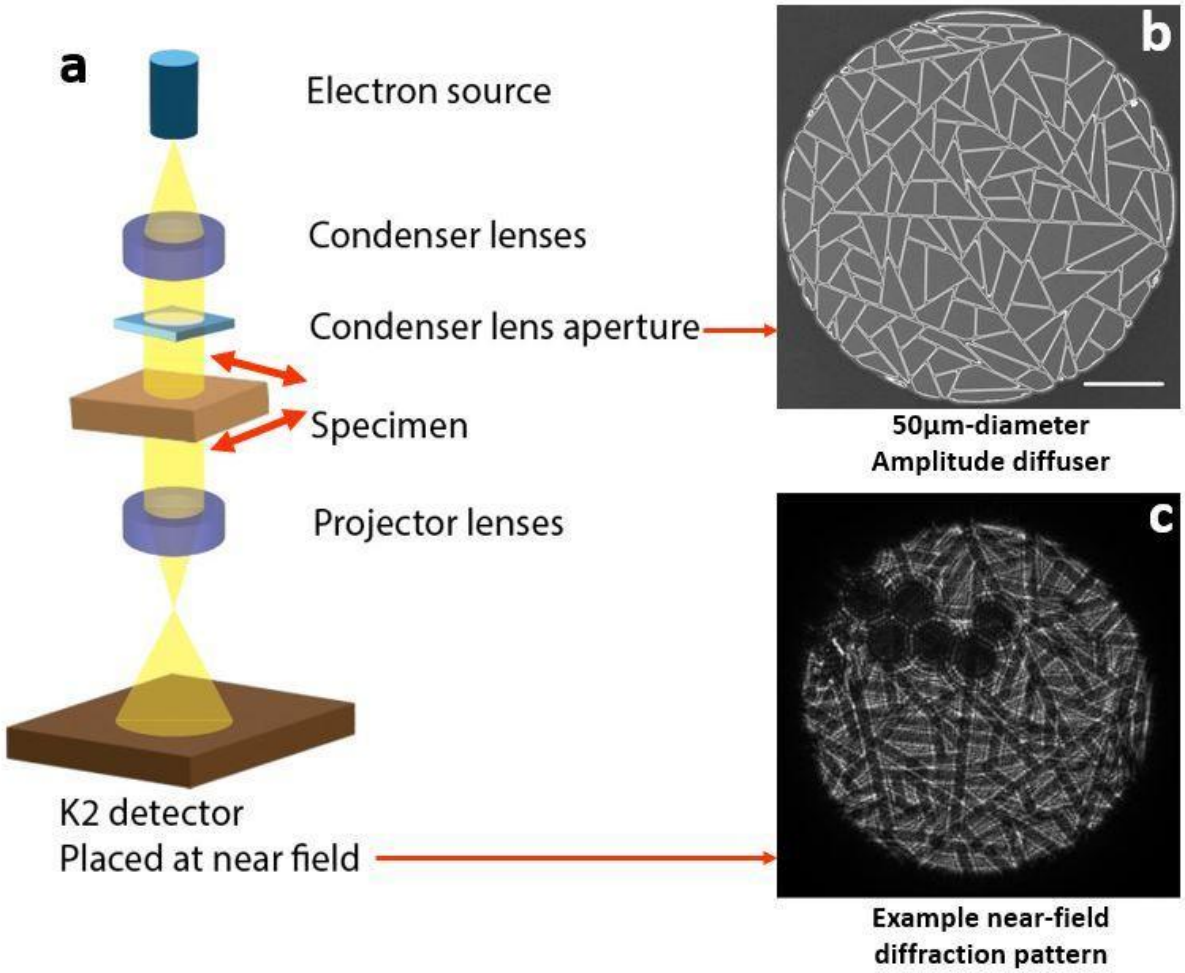

Fig 4.1. (a) The experiment setup of near-field electron Lorentz ptychography. The objective lenses are turned off. A parallel illumination probe, including features projected from the amplitude diffuser, propagates through a small area of the sample. The spatial translation of the sample is indicated by the red arrow. (b) The amplitude diffuser is inserted at the condenser lens aperture. The scale bar is 10 µm (c) An example near-field diffraction pattern with latex spheres as the sample.

The experiment setup is shown in Fig 4.1. Our design is implemented on the Cs-corrected Titan HOLO electron microscope at Ernst-Ruska Centre, Forschungszentrum Juelich GmbH, Germany, the same TEM used for conventional mode experiments in Chapter 3. The microscope was operated at 300 keV with spot size 3, in Lorentz mode with the objective lens

turned off for a field-free sample environment. The HOLO microscope is equipped with two electron biprisms optimised for flexible fringe field of view off-axis electron holography measurements and a Gatan K2 detector (model number 1000) with 3840×3712 pixels on a 5 µm pitch. The sample was translated using the stepper motor stages on the sample holder, programmed via Digital Micrograph scripts. Each dataset is cut out to be 2048 × 2048 pixels with the diffraction pattern in the middle. The exposures were 0.1 s with latex sphere and Mo-doped permalloy samples. Under the K2 linear mode, each set with 100 diffraction patterns took 5 minutes to collect.

Two experiments were designed. Initial experiments used, as a test sample, a 463 nm gold-shadowed carbon diffraction grating replica populated with polystyrene spheres 263 nm in diameter, as in previous papers (Maiden, Sarahan et al. 2015, Allars, Lu et al. 2021). With these tests, the ability to tune the illumination size and magnification was demonstrated. Next, phase imaging of a Mo-doped permalloy magnetic sample was attempted, with results then compared to off-axis electron holography on the same microscope.

For the initial experiments, the microscope condenser lenses were tuned such that out-of-focus images of the amplitude diffuser and condenser aperture were projected onto the carbon replica sample with diameters of 1 µm and 2 µm. The microscope projection lenses were adjusted to a defocus of 952 µm and a magnification of 3562 for the 2 µm experiment, and a defocus of 982 µm and a magnification of 7632 for the 1 µm experiment. The resulting diffraction patterns are exemplified by Figure 1c. The sample was scanned in a raster fashion through a grid of 10 × 10 positions with a step size of 20% of the corresponding illumination diameter.

For the magnetic sample experiments, the illumination profiles were chosen to be 2 µm so that the resulting images show the full view of the samples. The step sizes were 10% of the illumination diameter for the Mo-doped permalloy experiment.

4.2 The reconstruction process.

In terms of the reconstruction process, the Lorentz mode datasets are treated with the same procedure as the conventional mode datasets, shown in Fig 3.4. The difference is the scan position reproduction is discussed in section 4.2.1. To compare the ptychography results with

the holography results, the ptychography results are processed after the reconstruction, discussed in section 4.2.2.

4.2.1 Lorentz mode datasets scan position reproduction.

There are two reasons that the original cross-correlation failed to reproduce the scan positions of the magnetic sample. The first is the image contrast of such diffraction patterns is rapidly changing, as shown in Fig 4.2.

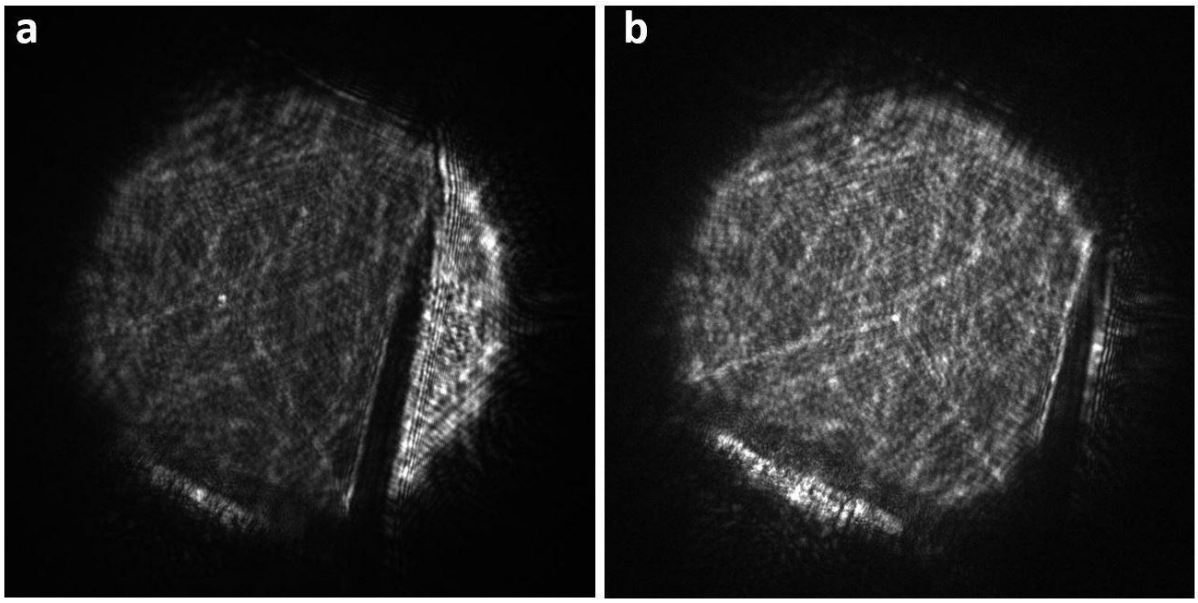

Fig 4.2. Two example diffraction patterns with the sample Mo-doped permalloy. (a) show permalloy (dark area) and vacuum (bright area). (b) is completely occupied by the permalloy. (a) and (b) are on the same scan row.

In the previous sample, the carbon substrate surrounds the latex sphere. The magnetic sample, however, is surrounded by a vacuum. The bright field disk is either completely occupied by the large-scale sample (Fig 4.2 b) or by imaging the sample with a vacuum in the same frame (Fig 4.2 a). Such two states are constantly switching, resulting in the same feature having inconsistent image contrast in different diffraction patterns. For example, the same area of the permalloy appears dark (Fig 4.2 a), and bright (Fig 4.2 b) in two diffraction patterns. As a result, cross-correlation failed to find distinguishable reference points to reproduce the scan positions.

One solution to such a problem is to pre-define the step sizes. The known step sizes are inputted into the cross-correlation algorithm. When processing two adjacent diffraction patterns, the algorithm only looks for the same reference point that is approximately one step size away. This avoids the algorithm confuses irrelevant features as the same feature.

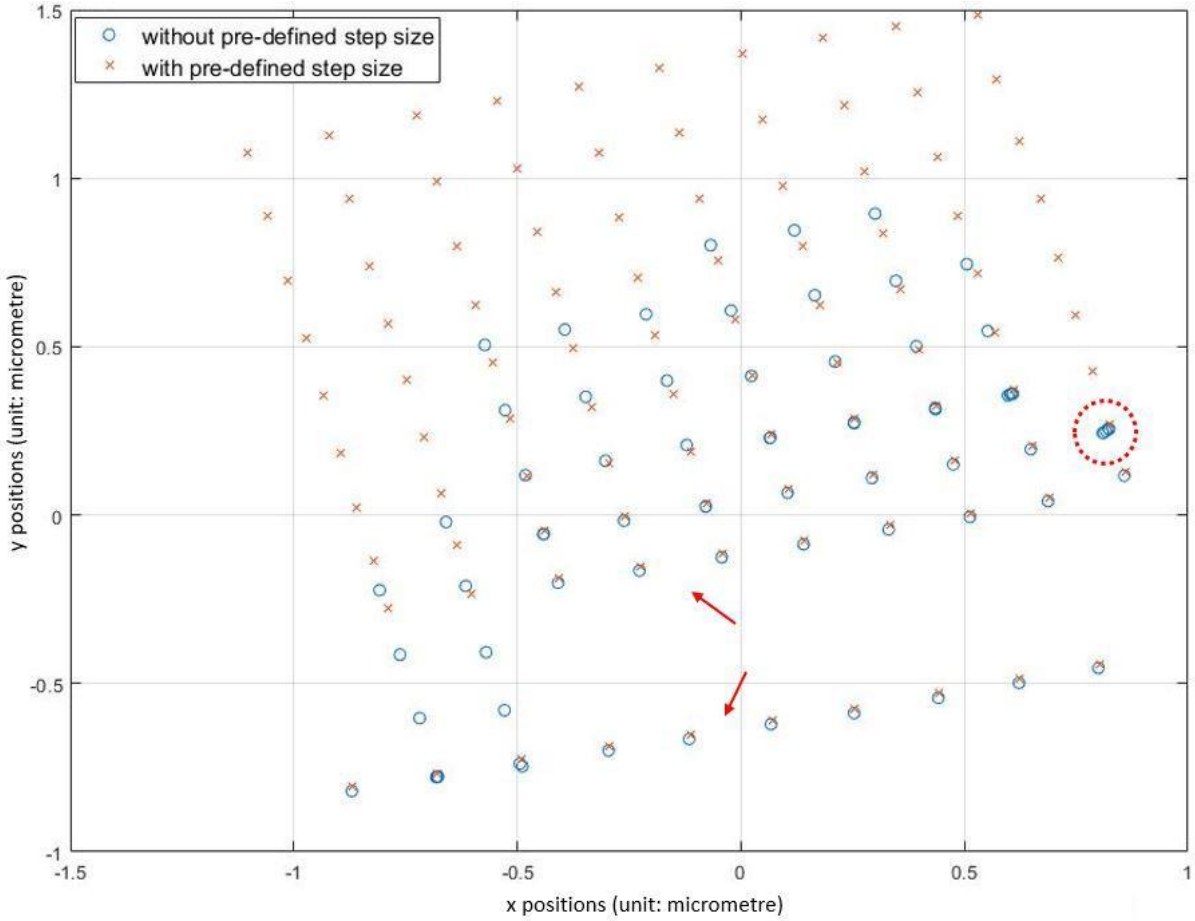

Fig 4.3 Reproduced scan positions with pre-defined step sizes (represented by x) and without pre-defined step sizes (represented by o). The datasets are the same as in Fig 4.2.

Without the pre-defined step sizes, the cross-correlation failed to reproduce scan positions, represented by o in Fig 4.3. When the permalloy does not completely occupy the bright field disk, such as in Fig 4.2 a, the cross-correlation can use the edge of the permalloy as the reference point. The reproduced scan positions are correct, as shown in the bottom two rows in Fig 4.3, highlighted by the red arrow. In these areas, the illumination probes scan the edge of the permalloy. However, when the bright field disk is completely occupied by the permalloy, such as in Fig 4.2 b, irrelevant features can be confused as the same thing, due to the rapidly

changing image contrast. This will result in wrong positions, such as the positions highlighted by the red circle.

Another problem is the sample drift and stage hysteresis. In far-field ptychography, the sample is translated by beam shifting. In other words, the beam is moving and scanning through the sample while the sample stage is stationary. The beam-shifting method is quick and precise, suitable for small step-size scans, typically a few nanometres. However, in near-field ptychography, the step sizes are much larger and can go beyond the maximum allowable range of reliable beam shifting. For example, with a 400 nm step size and 10 x 10 scans, it requires the spatial movement of 4 μm in both directions. Hence, our design moves the sample stage with the illumination probe being stationary to scan through the sample. Such a method is not as precise as the beam shifting method. As explained in Chapter 3.4.2, due to the sample drift and stage hysteresis, the first few scans in each scan column move at a shorter distance than the designed value. Moving the stage also requires a much longer collection time than the beam-shifting method. Under K2 linear mode, 100 diffraction patterns take 5 minutes to collect – due mainly to the movement and settling time of the stepper motor stage. During such a collection process, sample drift accumulates and reaches a state that causes degradation of reconstruction quality.

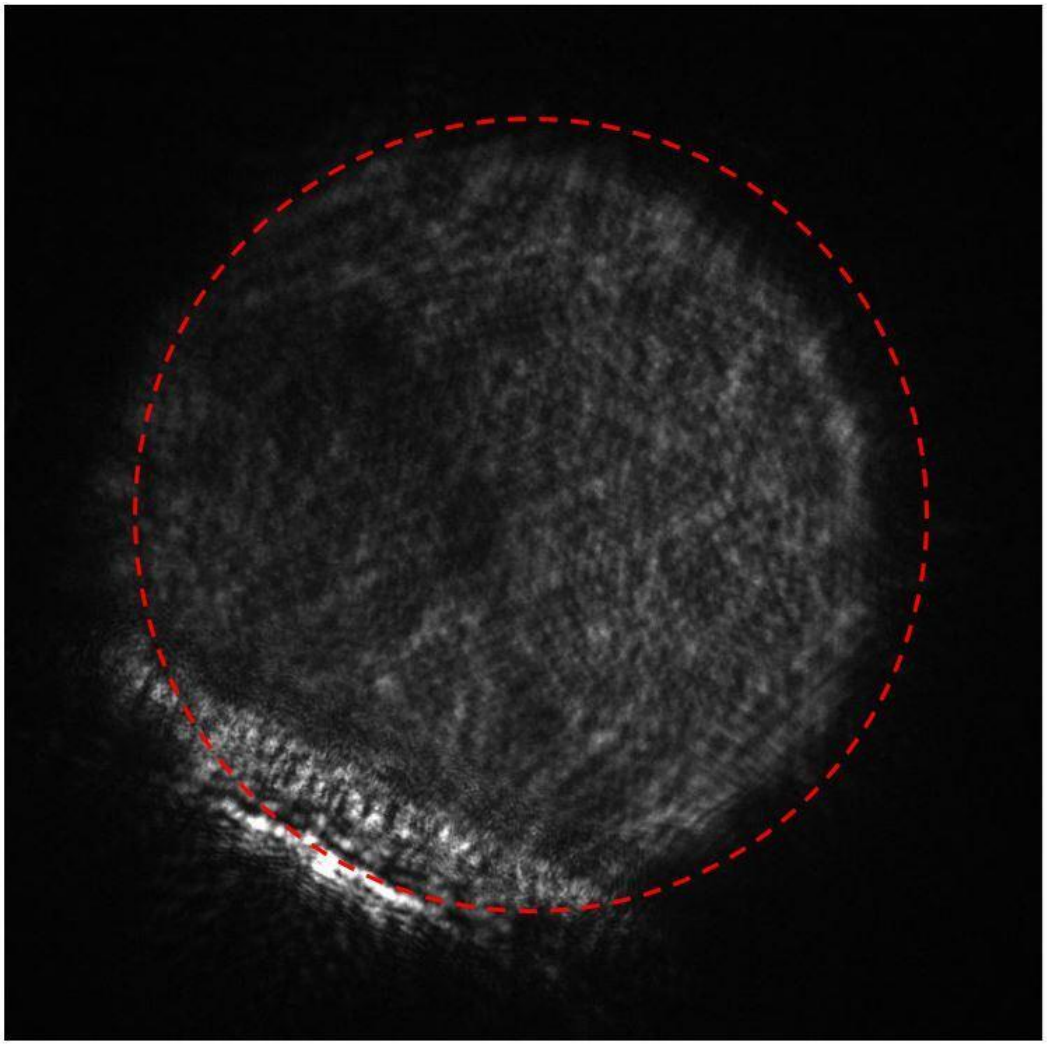

Fig 4.4. An example diffraction pattern that suffers from significant sample drifting

Fig 4.4 is an example diffraction pattern collected at the late stage of the collection process. The red dashed circle is centred at the centre point of the image. The bright field disk drifted towards the bottom left direction.

The first attempt at solving this problem is to centre the diffraction patterns automatically. The idea is to find a threshold value between the background area and the bright field disk area, similar to the process in section 3.4.4. Using this threshold value to map out the bright field disk and centre it. However, the bright field disk is usually not in a regular round shape, as shown in Fig 4.5.

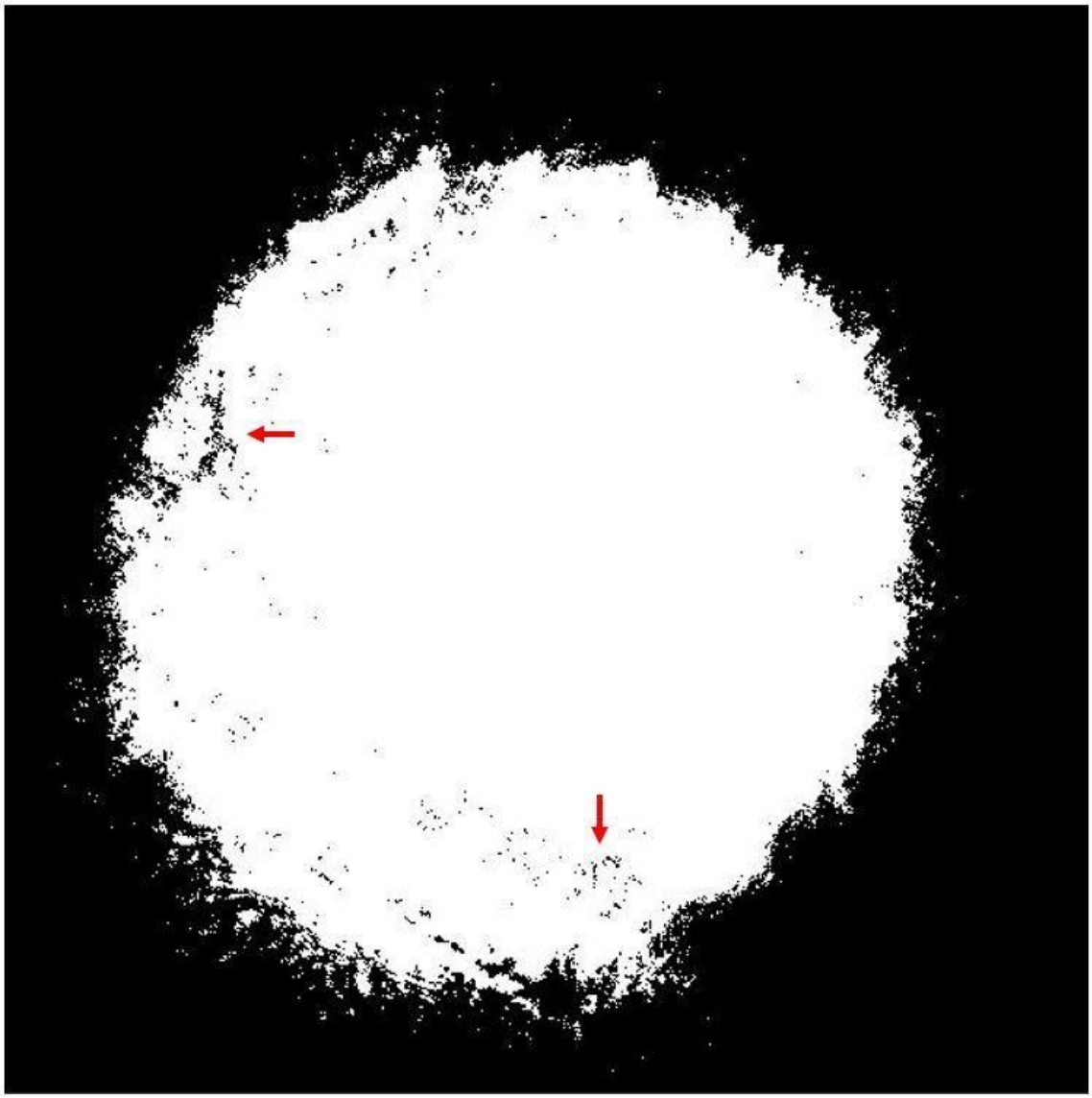

Fig 4.5. A diffraction pattern in which the bright field disk area (above the threshold value) is 1, and the background area (below the threshold value) is 0. The red arrow highlights the areas that are in the bright field disk but have a low value.

The bright field disk is often in irregular shape, and some areas in the bright field disk have an intensity lower than the threshold value, highlighted by the red arrows in Fig 4.5. This means it is difficult to find the geometric centre and the diffraction patterns cannot be accurately centred.

The second solution is to centre the diffraction patterns manually. The important part is to find a good reference diffraction pattern. This good reference should satisfy two points. First it should not be accurately centred, or not drifting itself already. The second is that the edge of such a diffraction pattern should be clearly identifiable. For the magnetic sample data, the

vacuum area has brighter contrast than the permalloy area, such as Fig 4.2 a. However, no diffraction pattern in our datasets is purely occupied by the vacuum. As a solution, the reference diffraction pattern is stitched using part of other diffraction patterns, shown in Fig 4.6

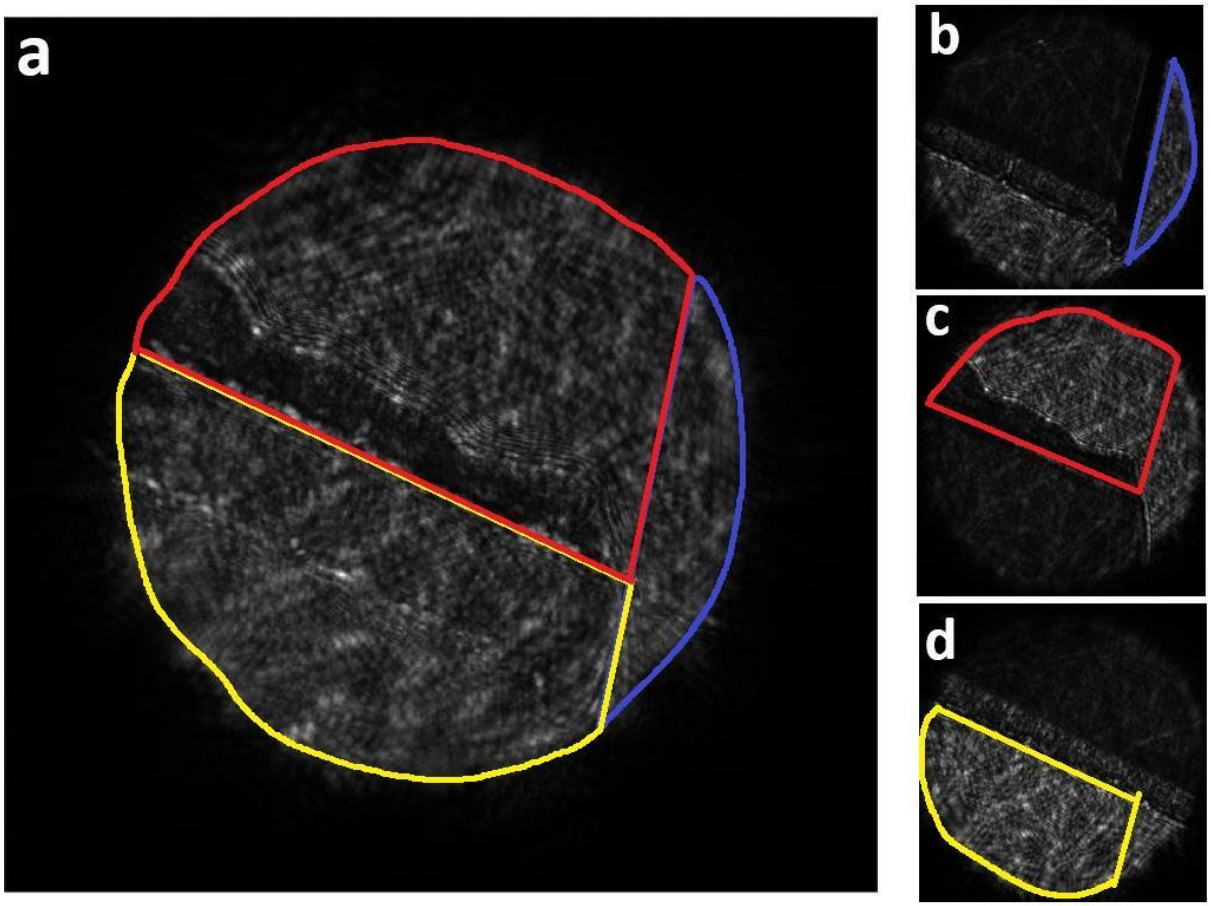

Fig 4.6. (a) is the reference diffraction pattern. The top half comes from the vacuum area in (c), highlighted by the red lines. The bottom half comes from the vacuum area in (d), highlighted by the yellow lines. The right part comes from the vacuum area in (b), highlighted by the blue lines.

To ensure the reference diffraction pattern had a clear edge, different parts of 3 diffraction patterns (number 9, 10 and 99) are cut out and stitched up. The diffraction pattern number 9 (Fig 4.6 b) and number 10 (Fig 4.6, c) and number 99 (Fig 4.6 d) are manually centred before cutting out the vacuum area from the bright field disk.

After finding a good reference, all the diffraction patterns are shifted to make sure the bright field disk is placed at the centre point. Two examples are shown in Fig 4.7.

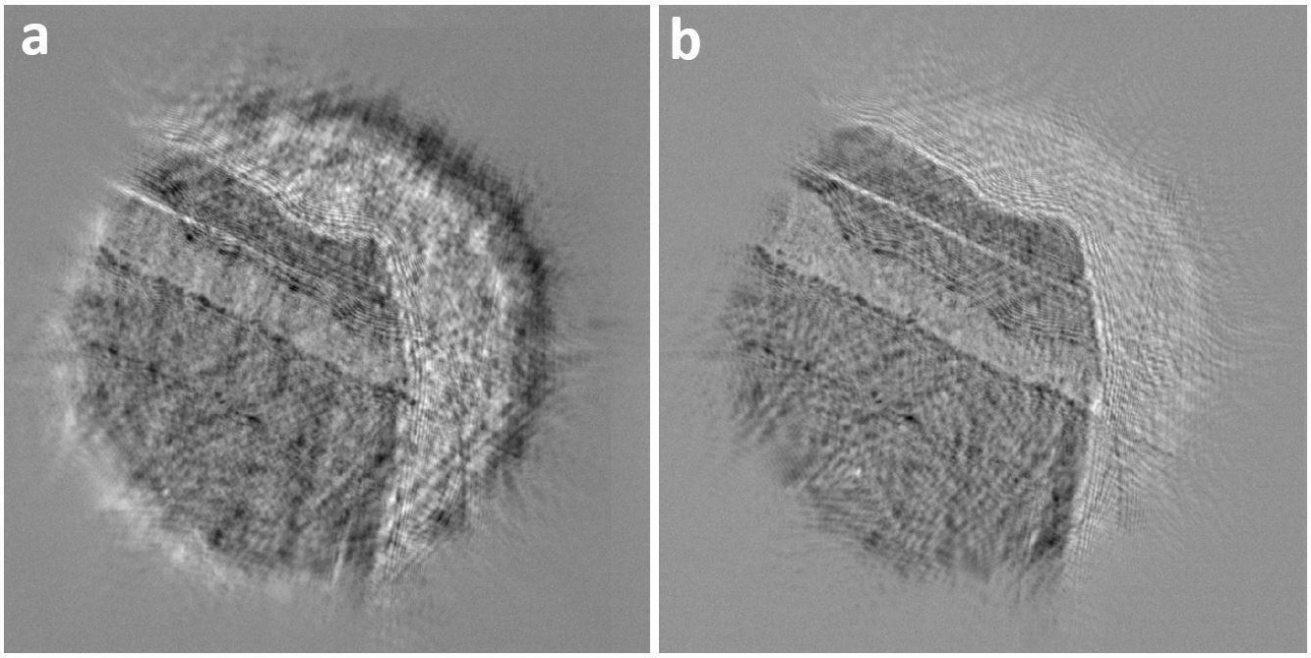

Fig 4.7. Two examples of manually aligning the bright field disks with the reference image. Both (a) and (b) are aligning the same diffraction pattern. (a) is an example of bad alignment, the bright field disk drifted towards the bottom left direction. The black area shown on the back is the reference bright field disk placed at the centre. (b) is an example of good alignment, two bright field disks are nicely aligned.

With all the diffraction patterns centred, the cross-correlation reproduces a more accurate scan position grid, shown in Fig 4.8 – any remaining centering and scan position errors are small enough to be handled by the reconstruction algorithm.

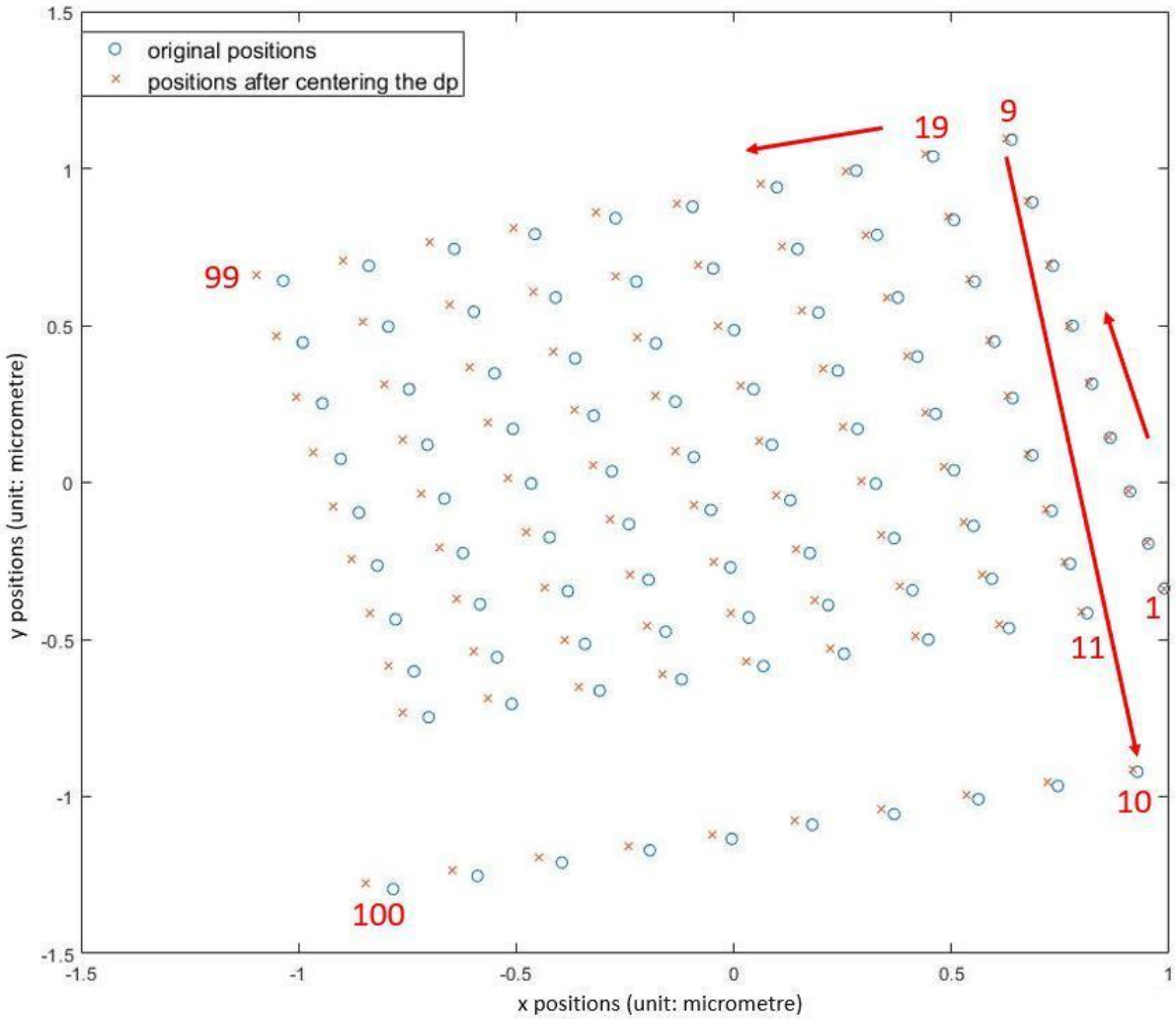

Fig 4.8. Scan position comparison between those using the original diffraction patterns (represented by o) and those using the centred diffraction patterns (represented by x). The number represents the order of the scan positions, starting with 1 at the bottom right, and moving in the direction indicated by the red arrow, ending at the bottom left (100).

Fig 4.8 shows the significant impact of sample stage drifting. With such a drifting effect, the measured distance between two adjacent patterns is the actual step size plus the bright field disk drifting distance. This results in incorrect step sizes and incorrect scan positions. The reconstructed images using such scan positions appear stretched. The accumulation of such a drifting effect can be clearly seen in Fig 4.8. At the start of the collection process, at the bottom right area (number 1), the scan positions reproduced from two datasets are aligned. As the scan proceeded in the direction indicated by the red arrows, such drifting effects accumulated, and the scan positions became less inaccurate.

Another attempt to reproduce the scan positions is called position training. The idea is to collect a set of diffraction patterns with the sample being the latex sphere. And use the same experimental parameters, including illumination sizes, scan step sizes, lens strength, etc, to collect the magnetic sample datasets. From previous experience, if the latex sphere is used as the sample, the cross-correlation can easily reproduce the scan positions. Such scan positions can be used to reconstruct the magnetic sample datasets, if the cross-correlation fails . These latex sphere datasets with the same experimental parameters as magnetic sample datasets, are considered as a backup plan.

With closer examination, we found that the first scan after setting up the microscope was not stable. The step sizes in the first dataset had more variation. The sample stage settled down and moved in a more accurate fashion at the third dataset, examples are shown in Fig 4.9.

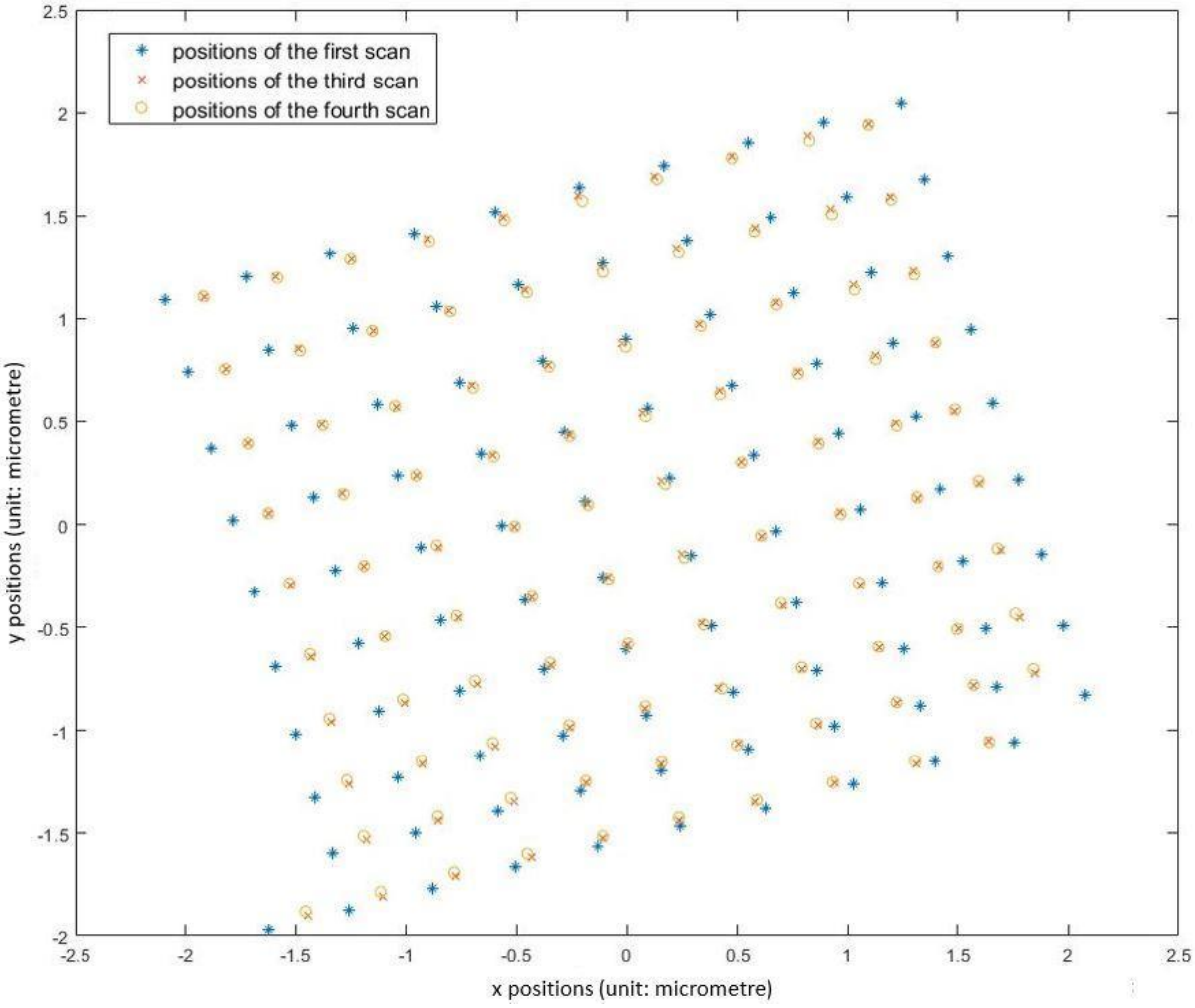

Figure 4.9. Reproduced scan positions from three datasets. Note that all the diffraction patterns are centred before the cross-correlation.

The first dataset, represented by *, has a different step size than the designed value. As the sample stage becomes more stable, the scan positions are more repeatable. The position from dataset 3, represented by x, and dataset 4, represented by o, are well aligned. Hence, the latex sphere sample was scanned four times. The magnetic sample was scanned with the same experimental condition four times as well.

4.2.2 Magnetic sample datasets reconstruction.

The first problem of reconstructing the magnetic sample datasets is to find the defocus value. The magnification can be easily found by measuring the physical size of the bright field disk, but the defocus value is more difficult to determine, hence the defocus value from the latex sphere sample was used as an initial estimate for the magnetic sample datasets. This value is further tuned by manually checking the edge of the reconstructed phase images, as shown in Fig 4.10.

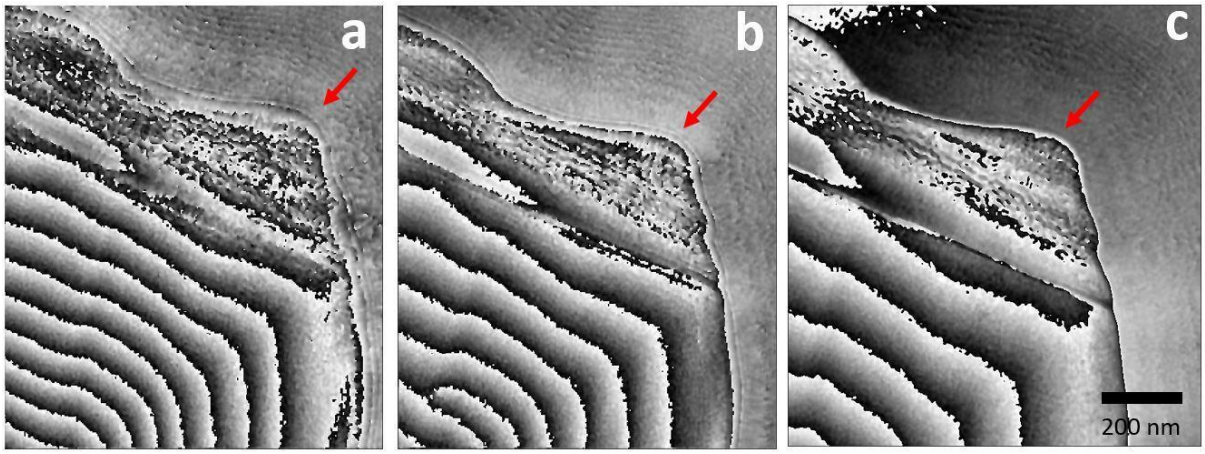

Fig 4.10. Reconstructed phase images of the Mo-doped permalloy sample under different defocus values. Both (a) and (b) used incorrect defocus values. (c) used the correct value.

Just like the latex sphere sample, the edge of the magnetic sample has Fresnel fringes under inaccurate defocus values, such as Fig 4.10 (a) and (b). Under the correct defocus value, the edge should appear sharp, such as Fig 4.10 (c).

After the correct defocus and magnification values are found, the next step is to remove the phase vortices. Those phase vortices are determined as artefacts based on two facts. First, those vortices do not appear on the Holography reconstruction. Second, those vortices

appear at different locations for different reconstructions. An example of the phase image with vortices is shown in Fig 4.11.

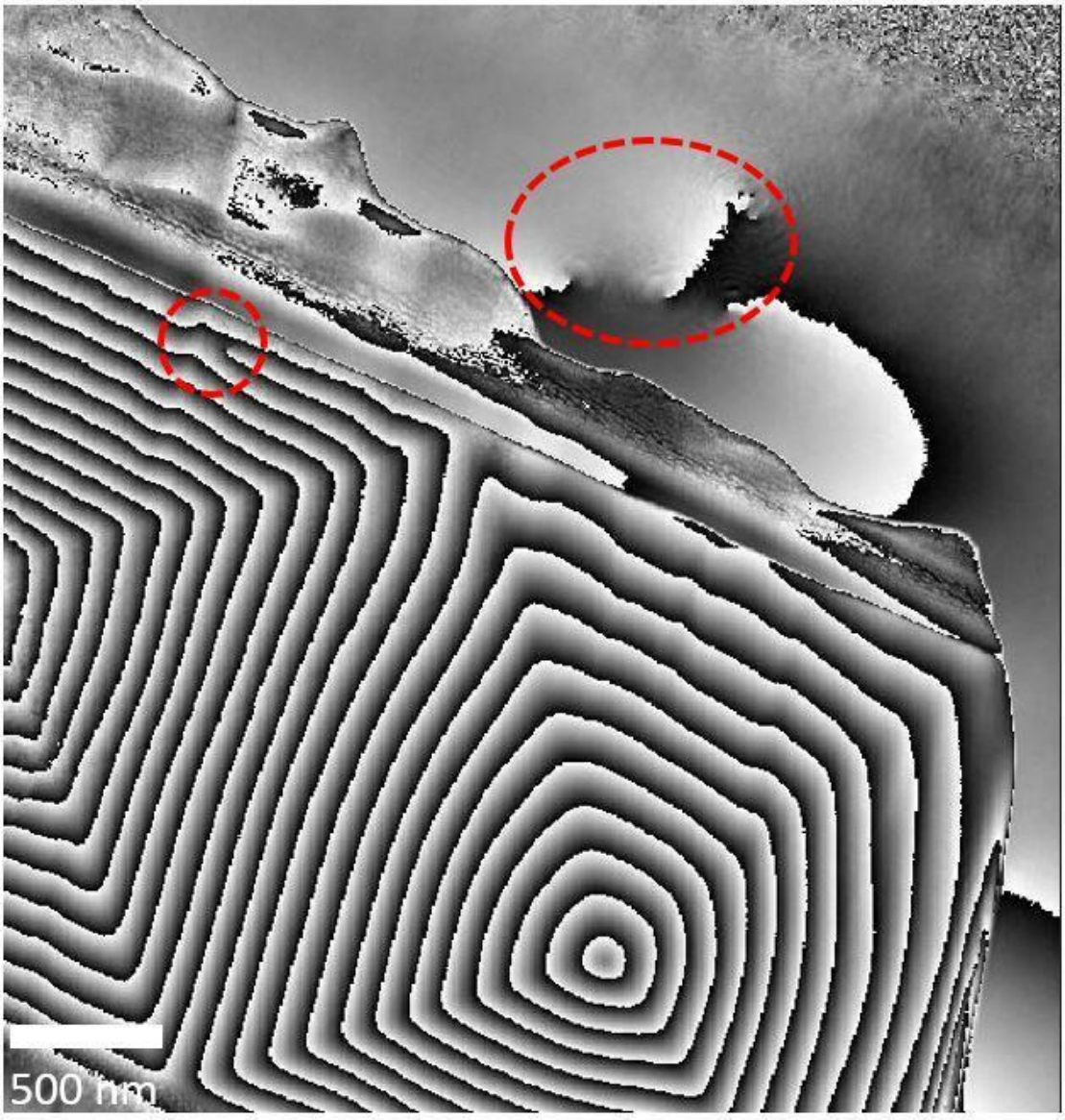

Fig 4.11. A phase reconstruction of the Mo-doped permalloy sample with vortices, indicated by the red ovals.

Phase Vortices are singularities in the phase part of complex results. Most of them appear near the sharp edge of the phase images, such as the red circled area in Fig 4.11, due to the rapid phase change in these regions. Vortices always appear in pairs, such as in the red oval area in Fig 4. 11. The possible reason for such an effect is the scan position and diffraction pattern drift. Even with all the measures mentioned in the last section, the diffraction patterns are not perfectly centred. The first reason is that when the centring process is carried

out by humans, and prone to error. There is no function that can determine whether the bright field disks are shifted precisely to the middle point. The second reason is the difference between the actual step size and the cross-correlated step size may be smaller than one pixel, which is 2.8nm in our case. This means the reproduced scan position can have an error in a few nanometres.

Phase vortices problems have been discussed in the near-field ptychography community, especially when dealing with thick samples (Stockmar, Cloetens et al. 2013, Zanette, Clare et al. 2020). In our reconstruction, we used the method proposed in (Zanette, Clare et al. 2020). When a vortex is detected, a synthetic vortex of the opposite charge multiplies with the vortex and cancels it. However, this function only removes the vortices in the phase images, the modulus images are not corrected: an example is shown in Fig 4.12. The modulus images can only be corrected by running further iterations of the ptychography reconstruction. Hence, the vortices removal function is applied during the reconstruction.

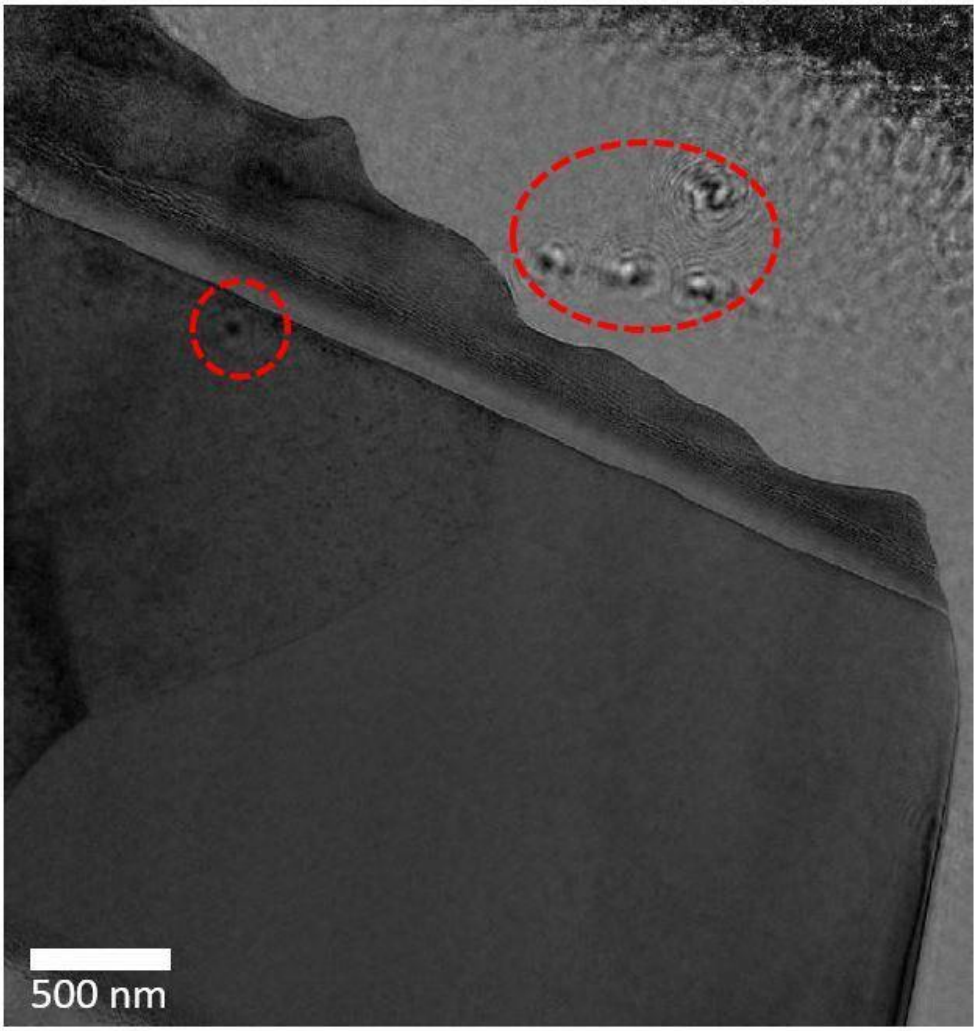

Fig 4.12. The modulus image of Fig 4.11. The same vortices also affect the modulus images. This can only be corrected by the ptychography reconstruction algorithm.

Another problem with this vortex removal function is that it causes spurious phase gradients and offsets in the phase image. In our case, the background of the permalloy, which is a vacuum, has phase ramps. The solution is to add a mask, that only applies the vortex removal function at the permalloy area and does not affect the vacuum area. The key is to find the threshold value that distinguishes the permalloy and the vacuum, as the examples show in Fig 4.13.

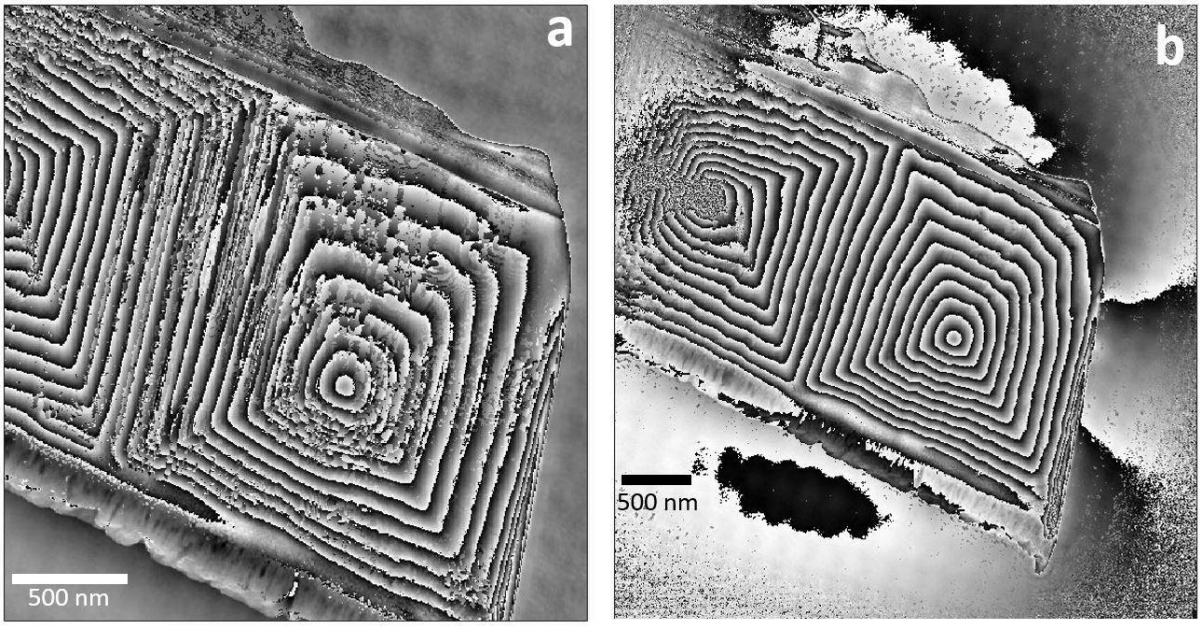

Fig 4.13. The corrected phase images (before continuing further reconstruction) using the vortex removal function. (a) used a low threshold value, the background is flat in phase, but the vortices are not properly removed. (b) used a high threshold value, the vortices are removed, but the background is affected.

4.3 Results and analysis.

This section presents the reconstruction results in Lorentz mode experiments, including the latex sphere sample and magnetic sample.

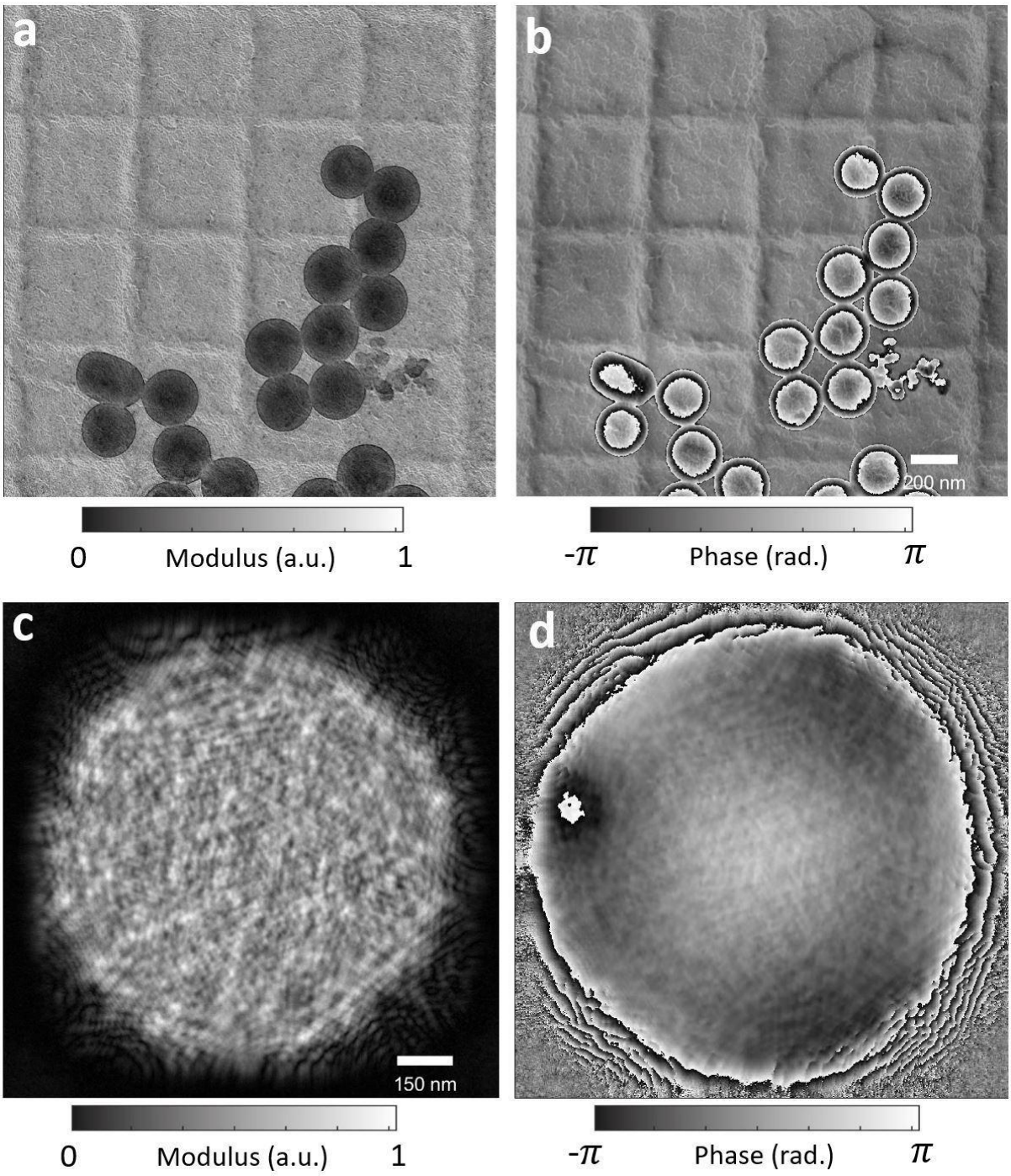

Fig 4.14. The modulus (a) and phase (b) reconstruction of the latex sphere sample in Lorentz mode. The corresponding illumination probe is shown in modulus (c) and phase (d). The illumination size is 1 µm, and the step size is 200 nm.

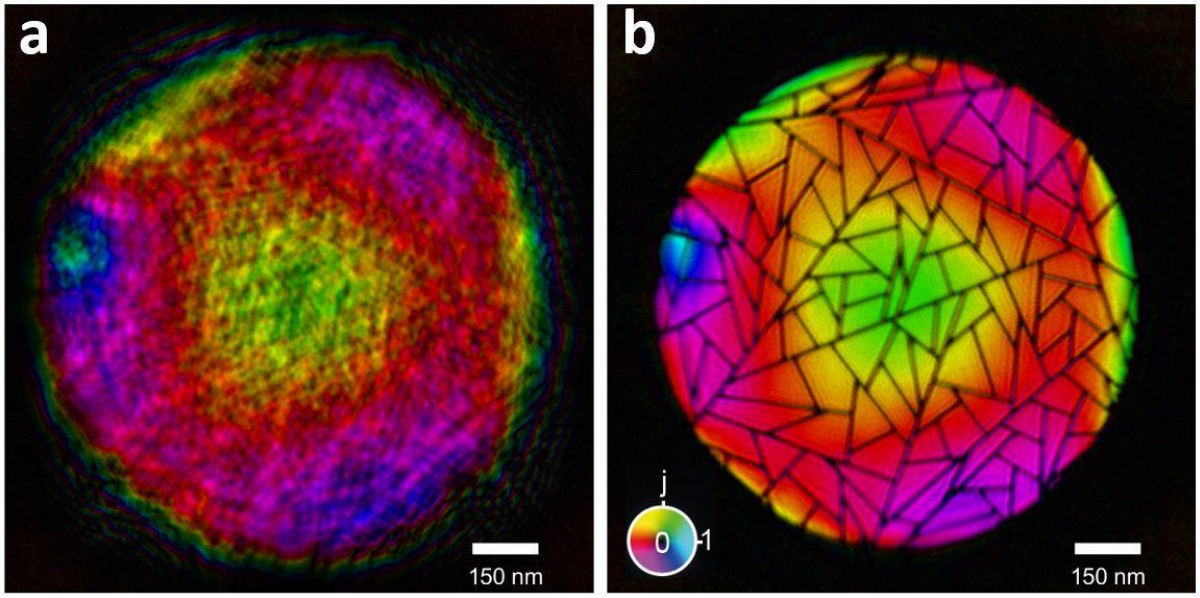

Fig 4.15. (a) is the complex colour map of the probe shown in Fig 4.14 (c) and (d). (b) is the same probe back-propagated to the focus plane. Note the features from the amplitude diffuser with the straight-line design are projected onto the probe.

The reconstructed sample images with the 1 µm-diameter illumination size are shown in Fig 4.14 (a) and (b). The illumination wavefronts are reconstructed by our algorithm along with the sample images and are shown in Fig 4.14 (c) and (d).

A Fourier Ring Correlation (FRC) is used to assess the resolution of our results. To do this, the diffraction patterns from each experiment are split into two subsets (the odd and even patterns) and two independent reconstructions are generated. The FRC is calculated from the 600 × 600 pixels central area of the two resulting phase images. The half-bit threshold, which is used as a resolution measure, intersects the FRC curve at a frequency of 0.1879 nm^{-1}, corresponding to resolutions of 5.32 nm.

The out-of-focused complex valued illumination probe, shown in Fig 4.15 (a), is back-propagated to the focus plane, shown in Fig 4.15 (b). At the focus plane, the design of the amplitude diffuser can be seen. However, the line features are not in focus at the same plane along the z-axis. For example, the lines in the horizontal direction are better in focus than the lines in the vertical direction. The reasons include uncorrected lens aberration, astigmatism and error in reproduced scan positions. The lens aberration and astigmatism can be compensated in the algorithm by an opposite synthetic aberration to cancel it. An interesting topic for further work.

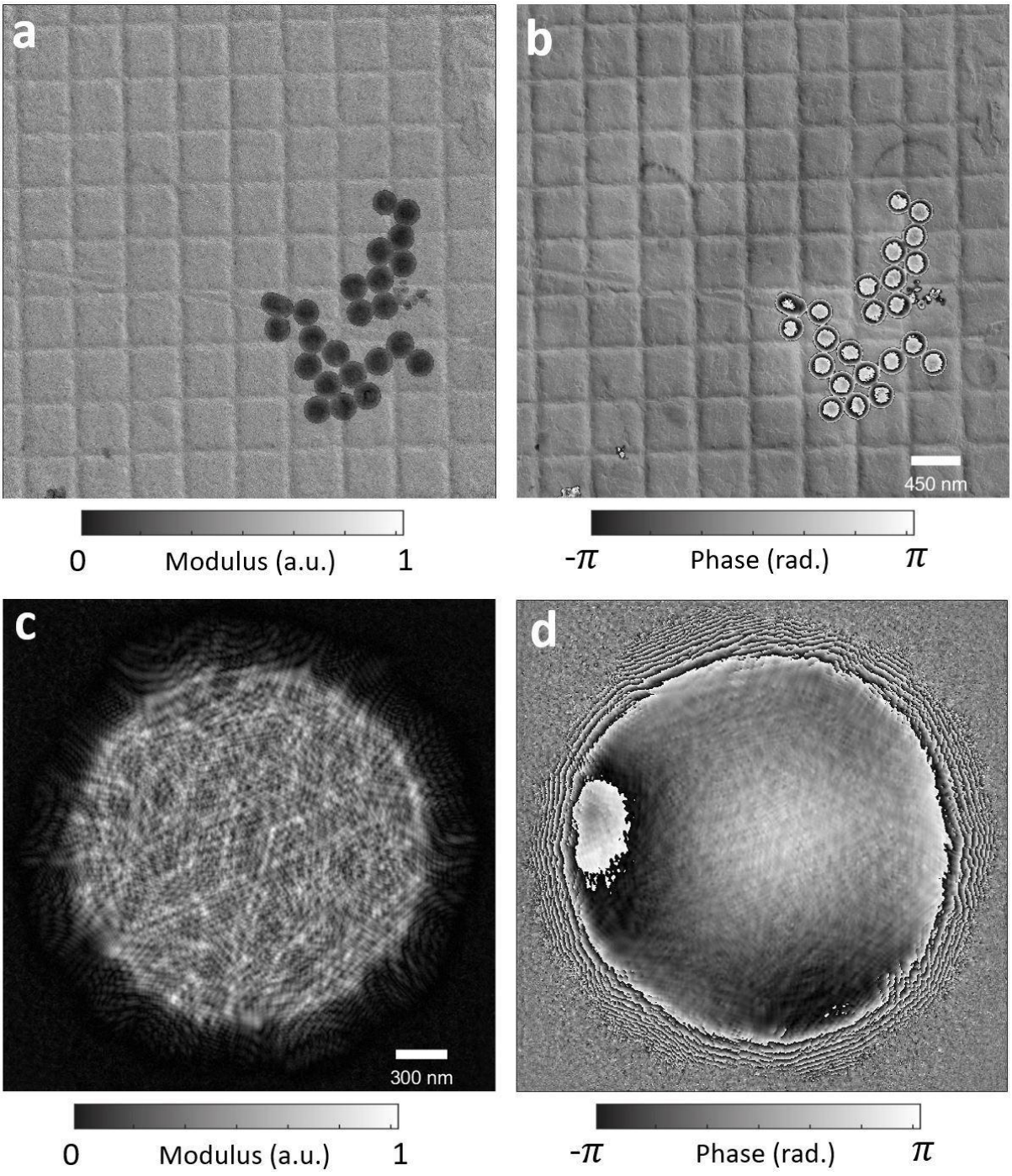

Fig 4.16. The modulus (a) and phase (b) reconstruction of the latex sphere sample in Lorentz mode. The corresponding illumination probe is shown in modulus (c) and phase (d). The illumination size is 2 μm, and the step size is 400 nm.

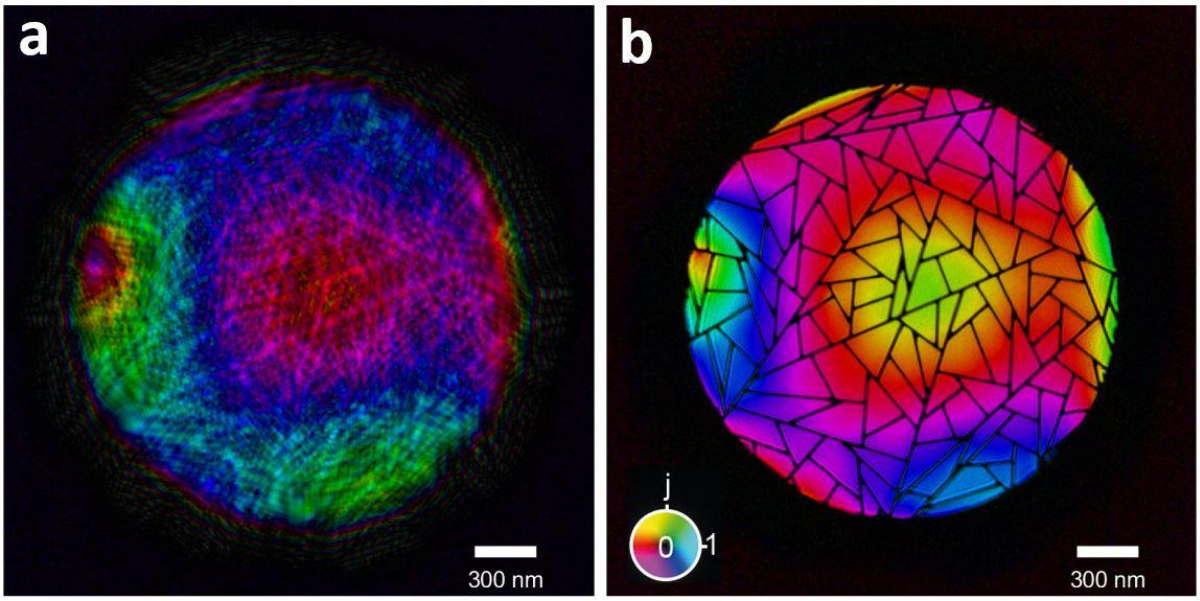

Fig 4.17. (a) is the complex colour map of the probe shown in Fig 4.16 (c) and (d). (b) is the same probe back-propagated to the focus plane. Note the features from the amplitude diffuser with the straight-line design are projected onto the probe.

The reconstructed sample images with the 2 µm-diameter illumination sizes are shown in Fig .4.16 (a) and (b). The illumination wavefronts are reconstructed by our algorithm along with the sample images and are shown in Fig 4.16 (c) and (d). Similarly to the results with 1 µm-diameter illumination sizes, an FRC is used to assess the resolution of our results. The half-bit threshold intersected the FRC curve at a frequency of 0.0982 nm^{-1}, corresponding to resolutions of 10.18 nm.

As for the Mo-doped permalloy experiment, besides the ptychography datasets, an off-axis holography dataset with the same sample is collected. The ptychography reconstruction produces a full-view image of the permalloy. Holography reconstruction only shows part of the permalloy. To quantitatively compare these two results, the ptychography result is rotated and cut out, shown in Fig 4.18.

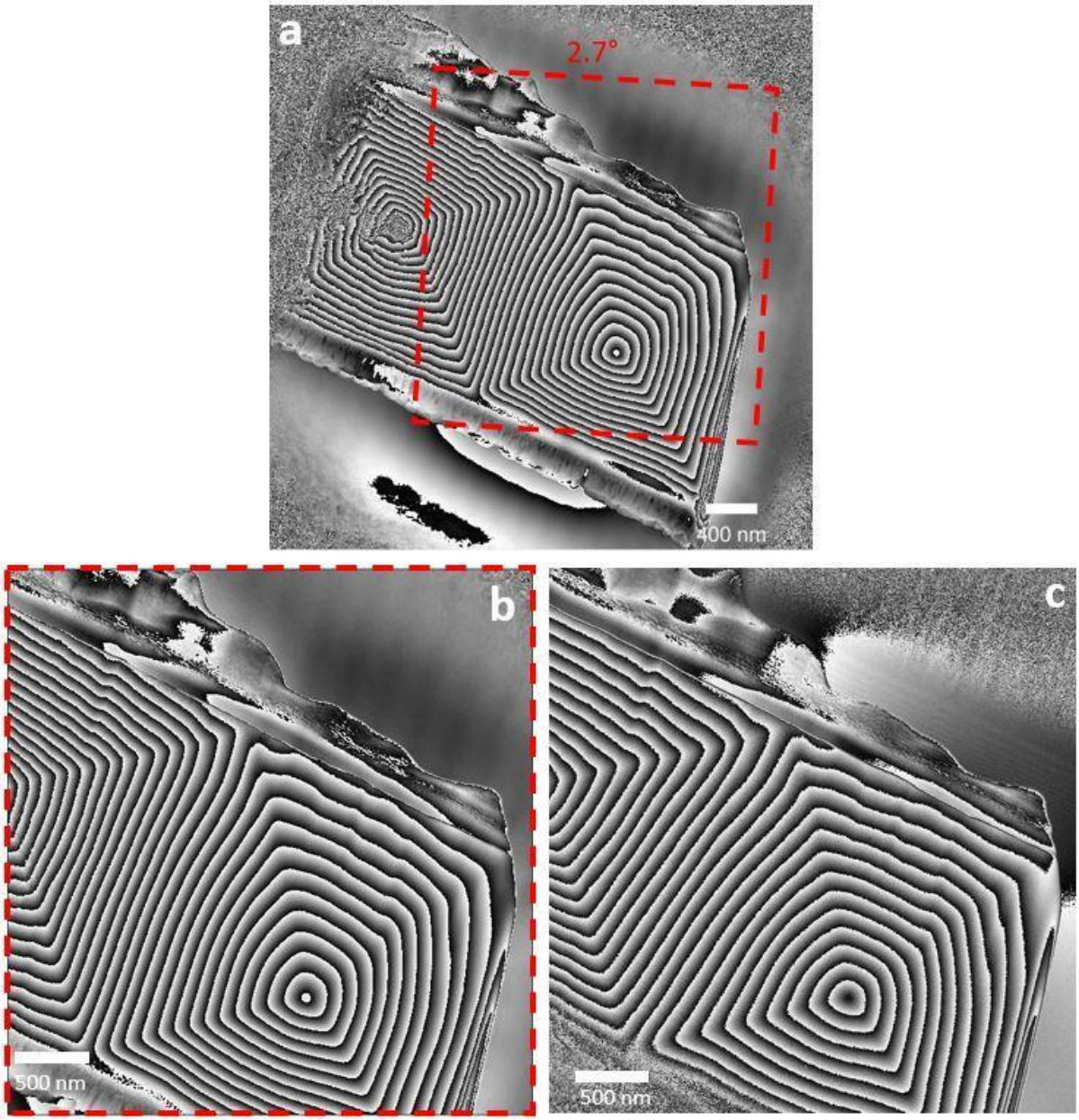

Fig 4.18. Phase reconstructions using ptychography (a) and (b), and holography (c). (b) is cut out and rotated from the red dashed line area in (a).

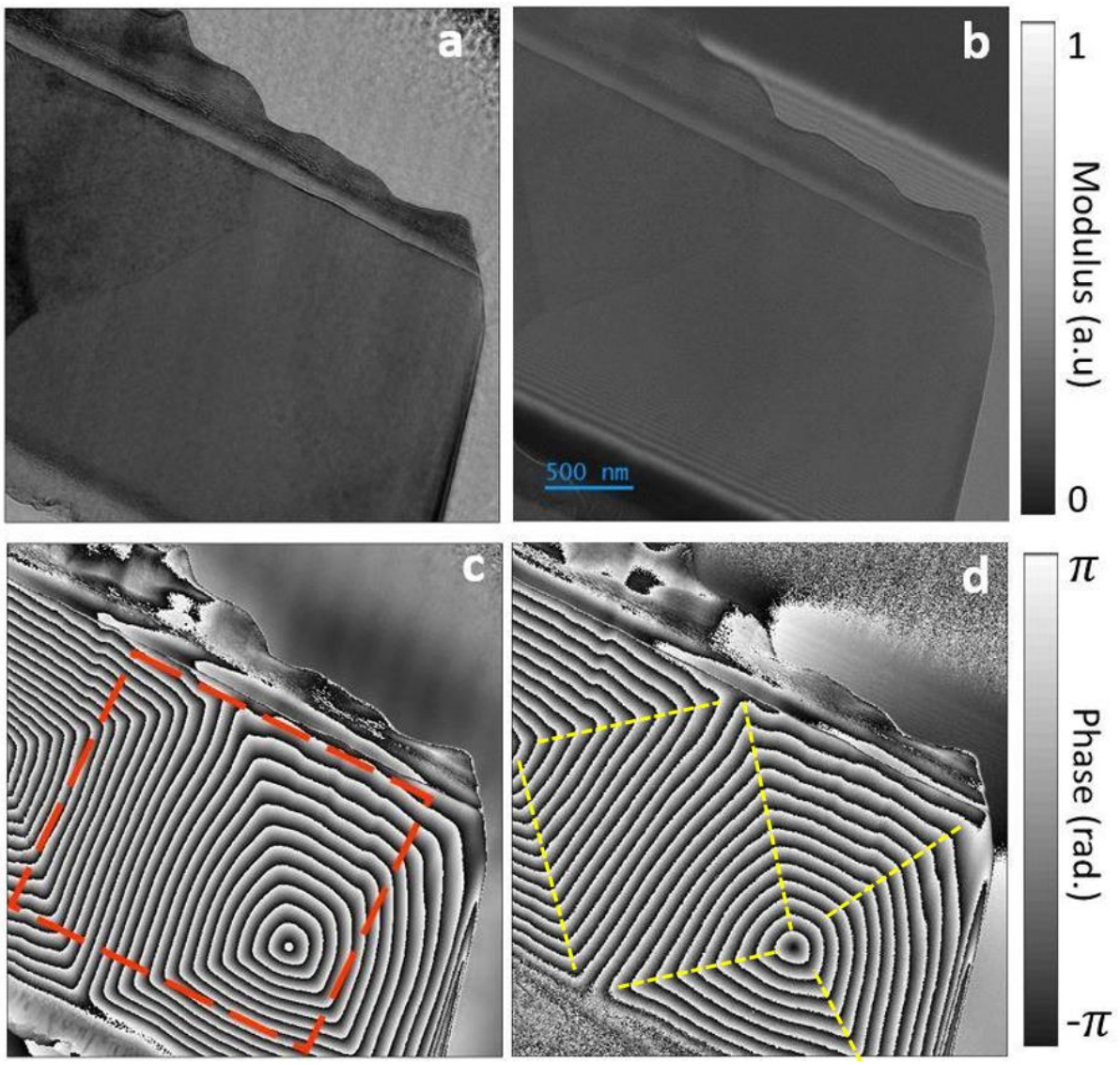

Fig 4.19. Reconstructed Mo-dope Permalloy using ptychography (a) modulus and (c) phase, and holography (b) modulus and (d) phase. The ptychography result is cut out from a full-view sample image to compare with the holography result. The region indicated by the red square is used to further analyse the accuracy of the phase reconstruction, as shown in Fig.4.21.

Ptychography and holography reconstruction results are shown in Fig 4.19. As discussed in equation (2.18), the magnetic features of the sample only relate to the phase image of the results and does not appear on the amplitude image. We can initially confirm that the pyramid-shape structure, which only appears on the phase image are caused by the magnetic field of the specimen. Since the objective lens is turned off and the sample is of uniform thickness, the phase signal in Fig 4.19 is predominantly governed by variations in the magnetic field. Six domain walls can be identified in the figure, indicated by the yellow dashed lines.

The results from ptychography and holography were carefully registered to account for differences in rotation, magnification and sample positioning within the field of view, plus a small degree of relative astigmatism between the two results. The comparison in Fig 4.19 shows a good match in both modulus and phase.

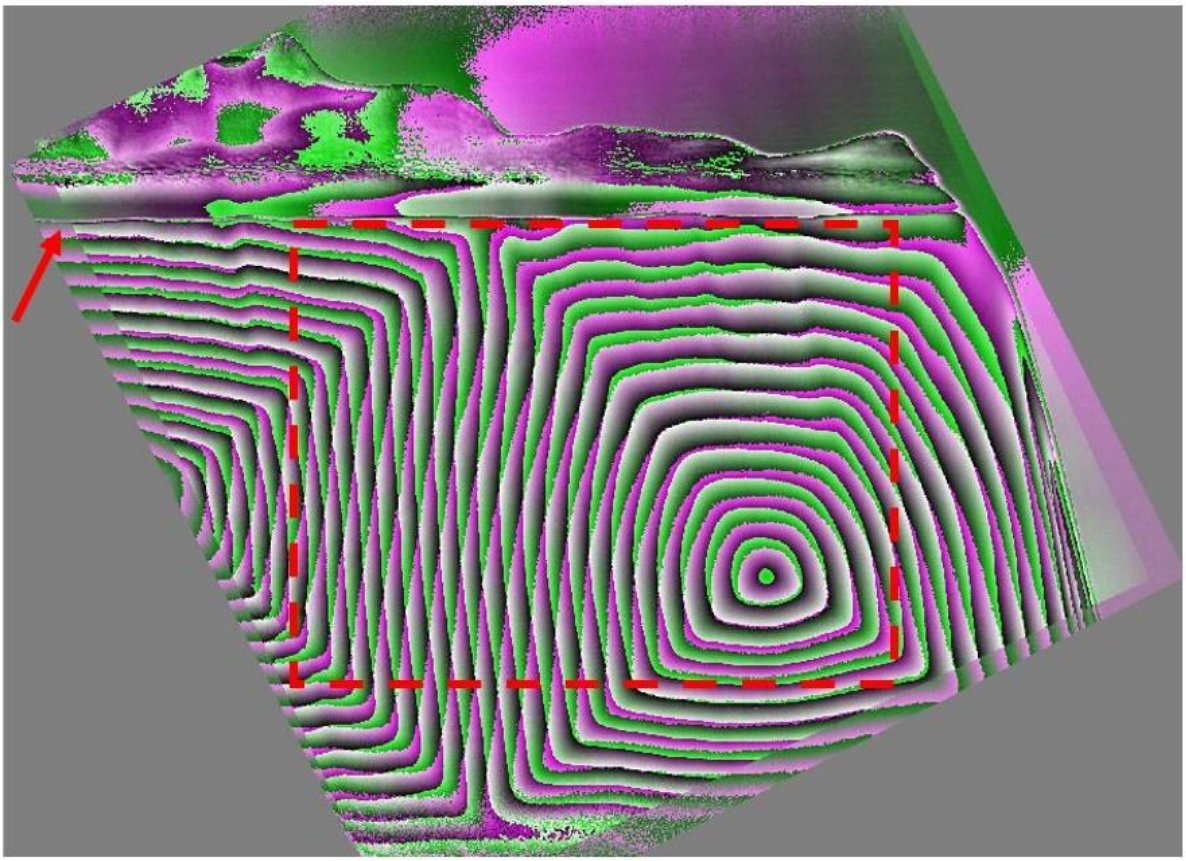

Fig 4.20. Two phase images from ptychography and holography are overlapped and aligned.

To further analyse the differences arising in the phase images, two phase results, Fig 4.19(c) and Fig 4.19 (d), are aligned, as shown in Fig 4.20. Due to the small degree of orientation differences between two phase images, the alignment process is using the edge of the permalloy as a standard, indicated by the red arrow. The same areas from the two results, indicated by the red square in Fig 4.19 (c) and 4.20 are cutout and unwrapped. The difference between the unwrapped phases is shown in Fig 4.21.

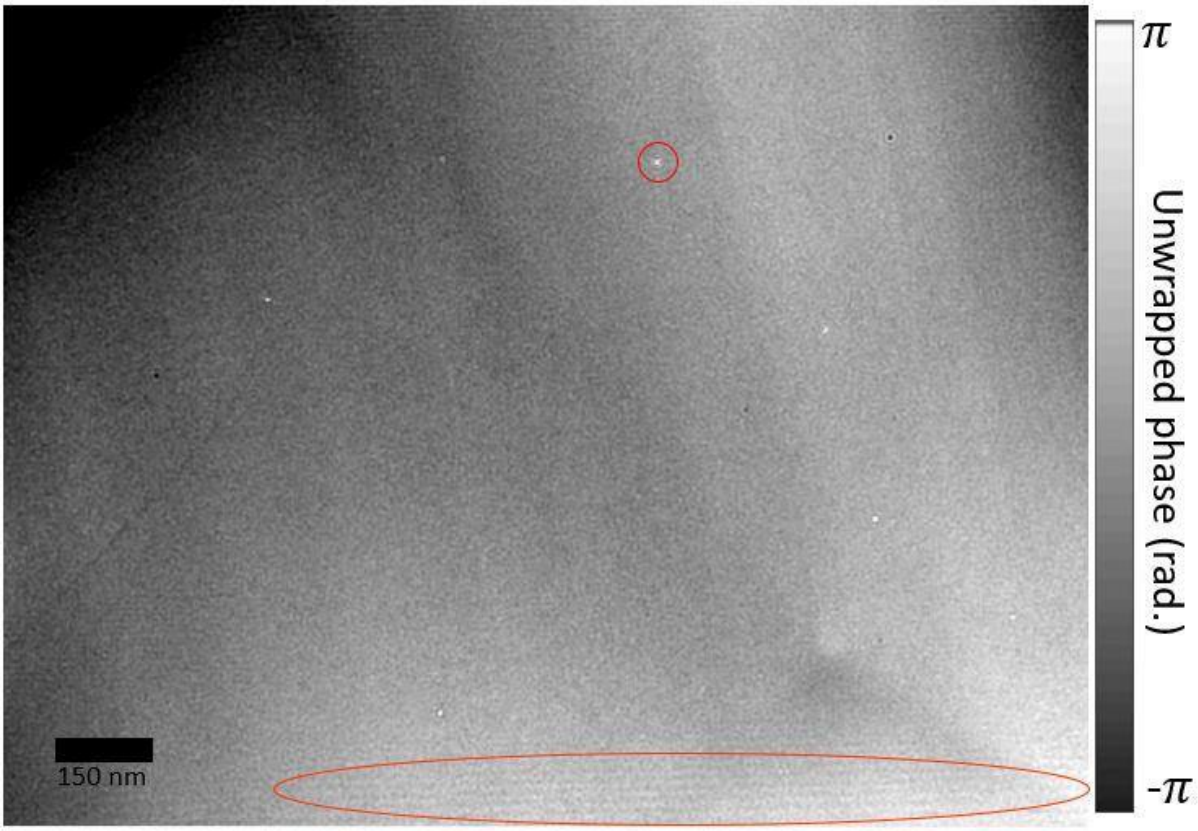

Fig 4.21. Comparison between unwrapped ptychography and holography phase images, the area indicated by the red square in Fig 4.19 (c) and Fig 4.20. The red circle identifies one of several artefacts , together with the fringes indicated by the red oval, are from the holography result.

The phase results recovered from the two techniques are unwrapped and compared. The difference between the unwrapped phases is shown in Fig 4.20. Several dots, such as that indicated by the red circle, appear in the hologram but not the ptychographic image and may be dead or occluded detector pixels. Fringes at the bottom, indicated by the red oval, correspond to biprism fringes at the edge of the hologram field of view. Apart from these artefacts, the central area shows close agreement between the two techniques.

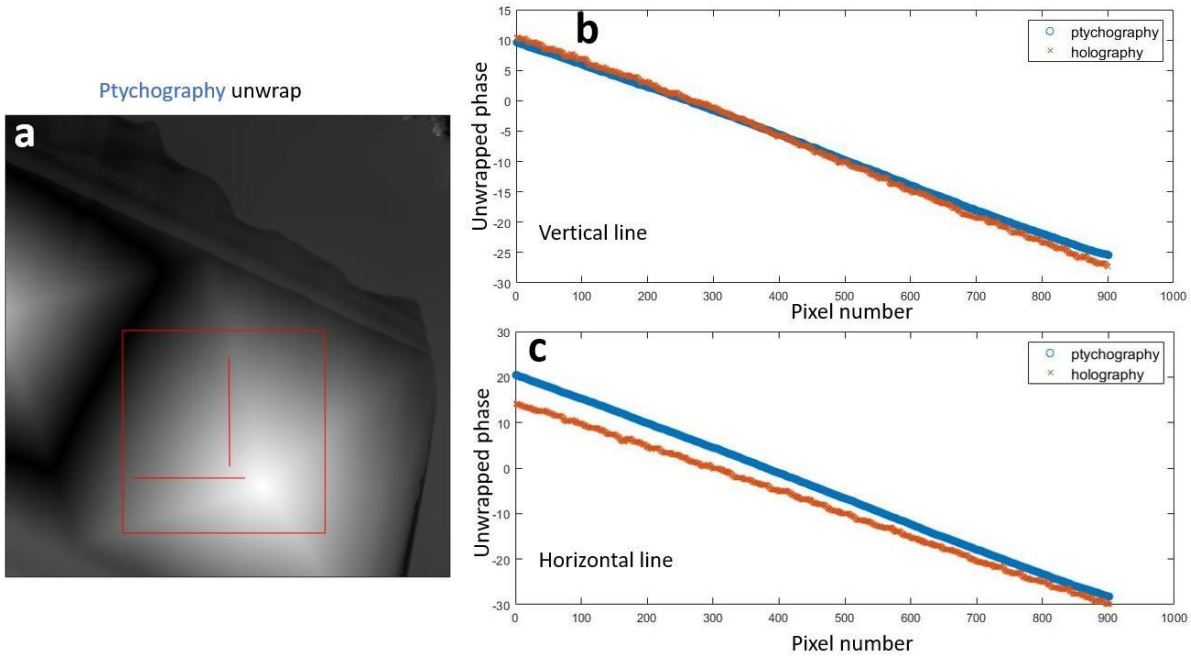

Fig 4.22. The line profiles comparison from the two unwrapped phase images. (a) is the unwrapped ptychography phase image. (b) is the comparison of the vertical line indicated by in (a). (c) is the comparison of the horizontal line indicated by in (a).

Another way to compare the similarities between the two recovered phase images is using the line profiles. Two lines at the same positions from two recovered phase images are compared. Note that the line profiles are normalised using average phase value inside the red circle indicated in Fig 4.22 (a). The phase gradient showed slight difference in both horizontal and vertical lines.

4.4 Conclusion

In this chapter, we have demonstrated a new implementation of near-field electron ptychography using an amplitude diffuser positioned in the condenser aperture strip. Unlike previous implementations, variable magnifications are possible in this geometry, via appropriate adjustment of condenser and projection lens settings; more efficient use of dose is ensured because there are no post-specimen apertures; and the amplitude diffuser reduces inelastic scatter in the recorded data compared to previous phase diffusers. Our results show

good agreement with off-axis holography. The ptychographic method benefits from a comparatively simple experimental setup and a readily extended field of view, and does not require a vacuum reference adjacent to the sample. Holography is quicker in terms of data collection and processing and is unaffected by inelastic scatter. One major objective of further development is to investigate the spatial resolution limit of the new method. To reach atomic resolution would require an illumination size much smaller than the 1um used here and would therefore require a step size smaller than the minimum movement possible with the stepper motor stage. Hence, to investigate the spatial resolution limit, a more efficient scanning approach is required, perhaps using the beam shift coils or a piezo-driven sample stage. Both alternatives would also deliver a quicker collection process, which would compensate for stage drift. Since the dose efficiency is improved, this setup holds promise as well for low-dose phase imaging, so another objective is to investigate the capability of imaging beam sensitive samples.

Chapter 5. Explore the limitation of near-field electron ptychography.

Chapters 3 and 4 discussed the implementation of near-field electron ptychography in the conventional mode and the Lorentz mode respectively. As a new methodology, the capability of near-field electron ptychography remains unexplored in many aspects, such as performance under low-dose conditions, the capability of imaging bio-material samples, and the ability to achieve atomic resolution.

In this chapter, two experiments that attempt to explore these limitations are presented. The first experiment attempts to achieve atomic resolution, discussed in section 5.1. The second experiment attempts to explore the performance under low-voltage conditions with the latex sphere sample and a bio-material sample, presented in section 5.2.

5.1 Attempt to achieve atomic resolution.

This section is arranged as follows: The design process is discussed in section 5.1.1. The collection process is discussed in section 5.1.2. The results are presented in section 5.1.3.

5.1.1 The design process

In the electron community, the combination of aberration-corrected optics and high-angle annular dark-field imaging has made far-field ptychography a powerful tool for achieving

atomic resolution in 2D (Yang, Ercius et al. 2016, Jiang, Chen et al. 2018, Chen, Turgut et al. 2022) and in 3D (Chen, Jiang et al. 2021). With far-field ptychography, the resolution is directly related to the collection angle of the detector, as explained in equation 2.15 in Chapter 2. In near-field ptychography, the illumination profile is a near-parallel beam. Hence, the conventional method of calculating the diffraction-limited resolution is not applicable.

Although there are no mathematically described experimental conditions that can guarantee atomic resolution, some minimum requirements can be easily calculated. The resolution is defined as the minimum distance between two features that can be distinguished. And the smallest distance between features is one pixel. Hence, to achieve atomic resolution, the pixel size should be at least smaller than the atomic resolution, usually defined as 1.2Å. Otherwise, even if two distinguishable features are merely one pixel apart, the distance between them, or the resolution, is larger than the atomic resolution.

While designing our experiments, however, limitations from the hardware condition did not allow us to go beyond such extreme requirements. The image pixel size can be calculated using equation 3.1. The detector pixel size is 5 µm, to get an image pixel size of 1.2 Å, the magnification should be $\frac{5\ \mu m}{1.2\ \text{Å}} = 41666$. The number of pixels in our diffraction pattern is 2048 by 2048. The bright field disks normally do not occupy the entire diffraction pattern, as shown in Fig 5.1.

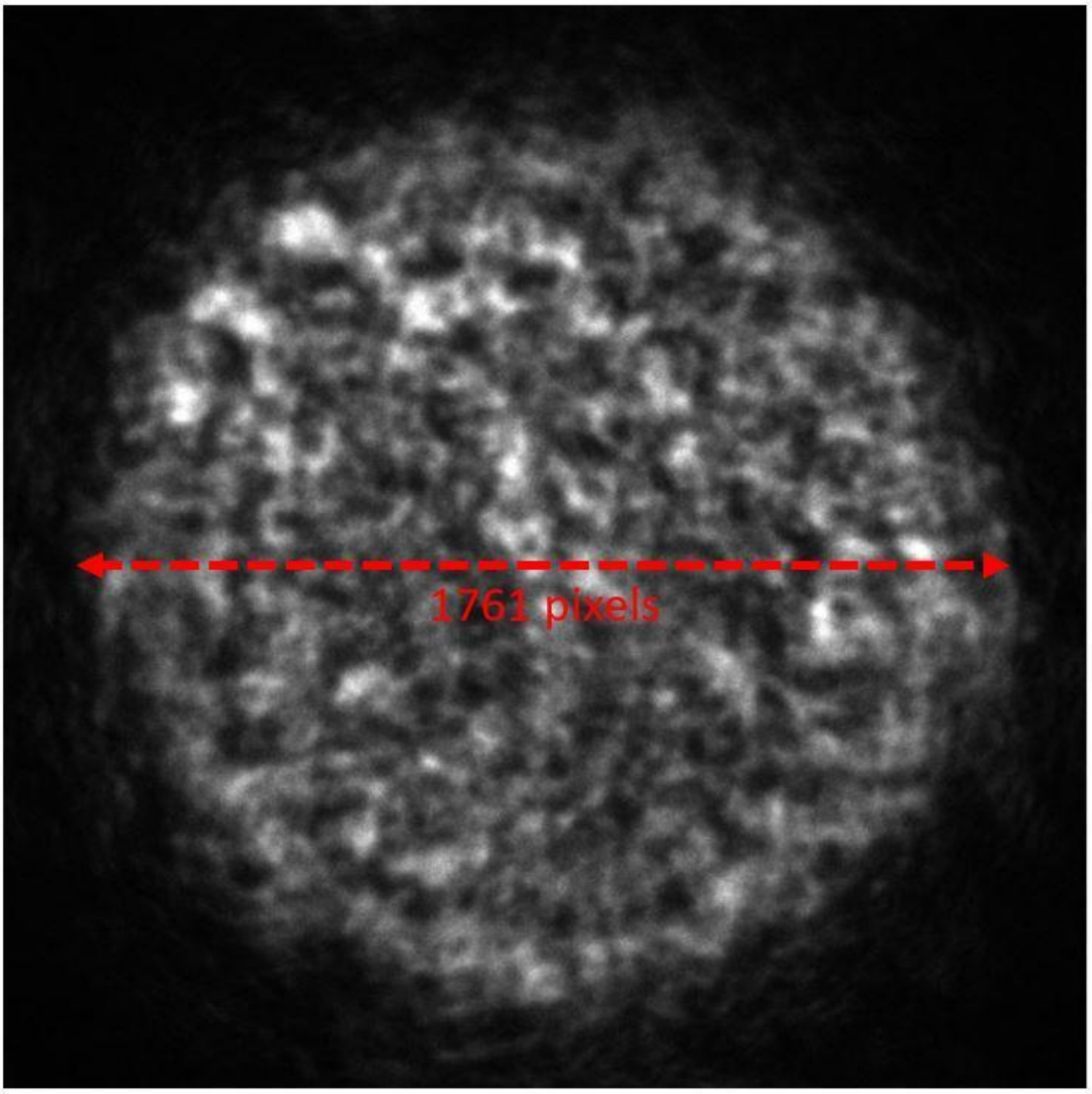

Fig 5.1. An example diffraction pattern. The pixel size of the diffraction pattern is 2048 pixels. The diameter of the bright field disk in this example is 1761 pixels.

A typical bright field disk has a diameter of around 1750 pixels. With the magnification calculated above, the diameter of the illumination profile needs to be shrunk down to $\frac{1750 \times 5\ \mu m}{41666} = 210\ nm$. In other words, a 200 nm-diameter illumination probe should be magnified 41666 times, and occupy 1750 pixels on the detector, with detector size being 5µm. This leads to two problems. The first problem is that the sample is highly magnified under such conditions. The cross-correlation algorithm may not be able to find distinguishable reference features to reproduce the scan position grid. The easiest sample, in terms of reproducing scan positions, is the latex sphere sample in our experiments. The latex spheres have a diameter of 263 nm. If using a 200 nm-diameter illumination probe to scan these

latex spheres, there will be some positions where the bright field disks are completely occupied by the latex spheres, similar to the situation when dealing with permalloy samples. Our solution is to scan a region where no latex spheres are present. The background of the latex sphere is a carbon substrate populated with gold particles. Although the gold particles in different shapes can be easily identified and used as a reference while in focus, the concern is whether these particles are still distinguishable under such high magnification.

The next problem is the scan step sizes. The step sizes in Chapters 3 and 4 are either 10% or 20% of the illumination size. Experiments with both step sizes produce clear results. In this experiment, the illumination probe size is calculated to be 200 nm-diameter. The step sizes are chosen from either 20 nm or 40 nm. However, these values are close to the minimum step distance of the sample stage.

To address this, the sample is translated using a more precise piezo stage, with a minimum movement distance of 5 nm. After some initial testing and tuning, the step size for this experiment was chosen to be 40 nm. The total field of view using 20 nm and 40 nm step size with 10 scan positions in each direction is 400 nm^2 and 600 nm^2 respectively. Since the gold particles are of different sizes and randomly distributed, a larger field of view is more likely to include the tiny gold particles that reach the limit of the resolution.

Experiments were carried out identically to those reported in Chapter 3. The design is implemented on the Cs-corrected Titan HOLO electron microscope at Ernst-Ruska Centre, Forschungszentrum Juelich GmbH, Germany. The detector is a Gatan K2 detector (model number 1000) with 3840×3712 pixels on a 5 µm pitch, but the diffraction pattern is cut out to be 2048 x 2048 pixels. The sample is a 463 nm gold-shadowed carbon diffraction grating replica populated with polystyrene spheres 263 nm in diameter. The region of interest is chosen to be an area where no latex spheres are present.

5.1.2 The data collection process

Two datasets were collected in conventional TEM mode. The lenses were adjusted to a defocus of 70 µm and a magnification of 43925. The illumination probe under such magnification was 200 nm. The sample was translated using the piezo stage with a step size

of 40 nm. The first dataset was a test run, and two problems were found during this test run. The first problem was the significant diffraction pattern drift. The diffraction pattern drifting problem can be manually corrected using the method described in section 4.2.1. However, while collecting the first datasets, the diffraction pattern drifts accumulated and reached a state where the bright field disk is out of the frame, as shown in Fig 5.2 (a).

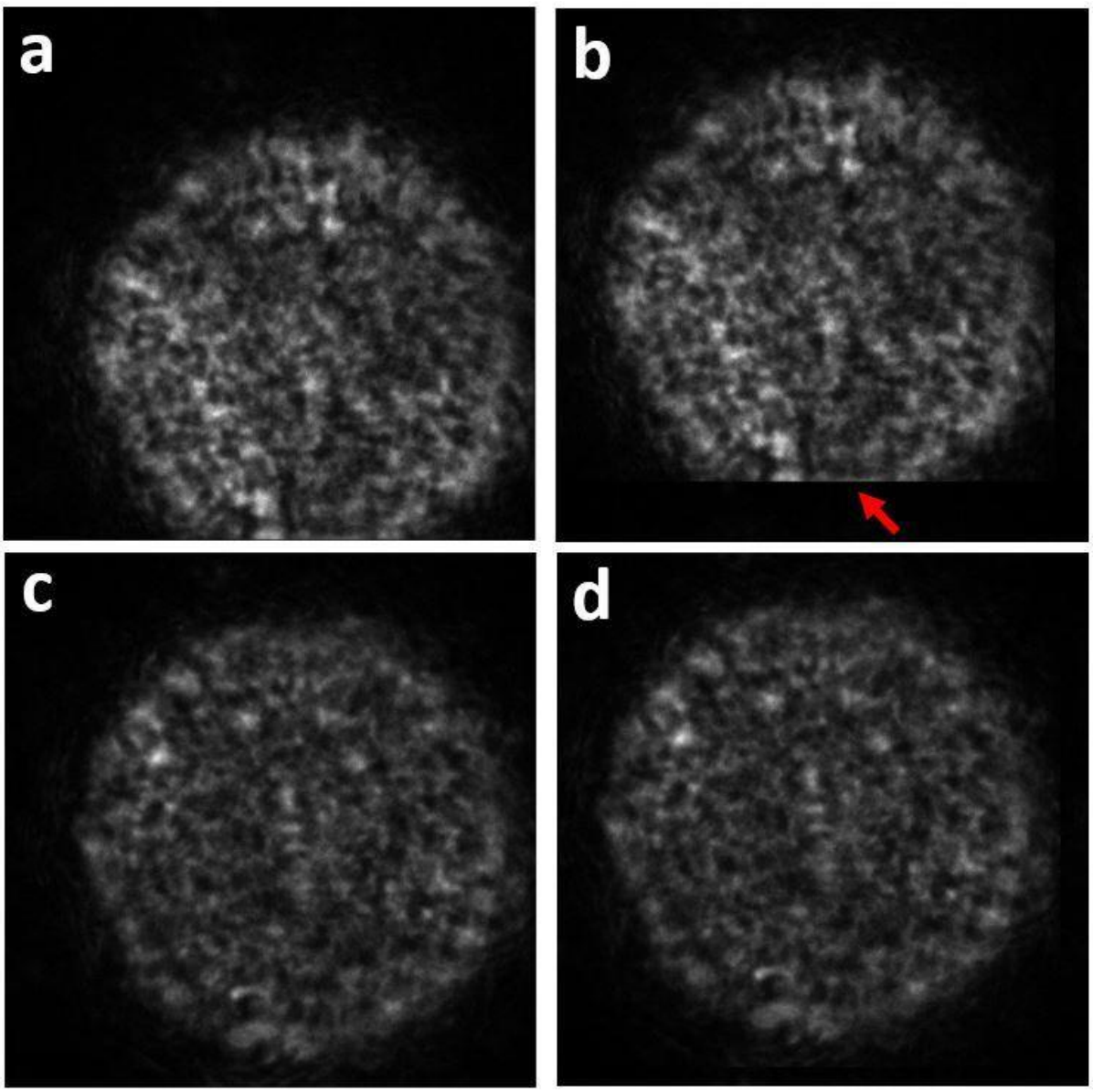

Fig 5.2. (a) is the 99th diffraction pattern from the first dataset. The bright field disk drifted out of the frame. (b) is the same diffraction pattern as (a) but centred. (c) is the 99th diffraction pattern from the second dataset. (d) is the same diffraction pattern as (c) but centred.

With this degree of drifting, even though the bright field disks are centred, as shown in Fig 5.2 (b), certain diffraction data is lost, indicated by the red arrow. This significant drifting problem is due to the long collection process using the piezo stage. After the collection algorithm was optimized, the drifting effect in the second dataset was improved, as shown in Fig 5.2 (c). At the end of the collection process, the accumulated drift did not push the bright field disks out of the frame. And after centering the bright field disks, all the data are preserved.

The second problem was that before the collection of the first dataset, the piezo stage was not excellently calibrated, as shown in Fig 5.3.

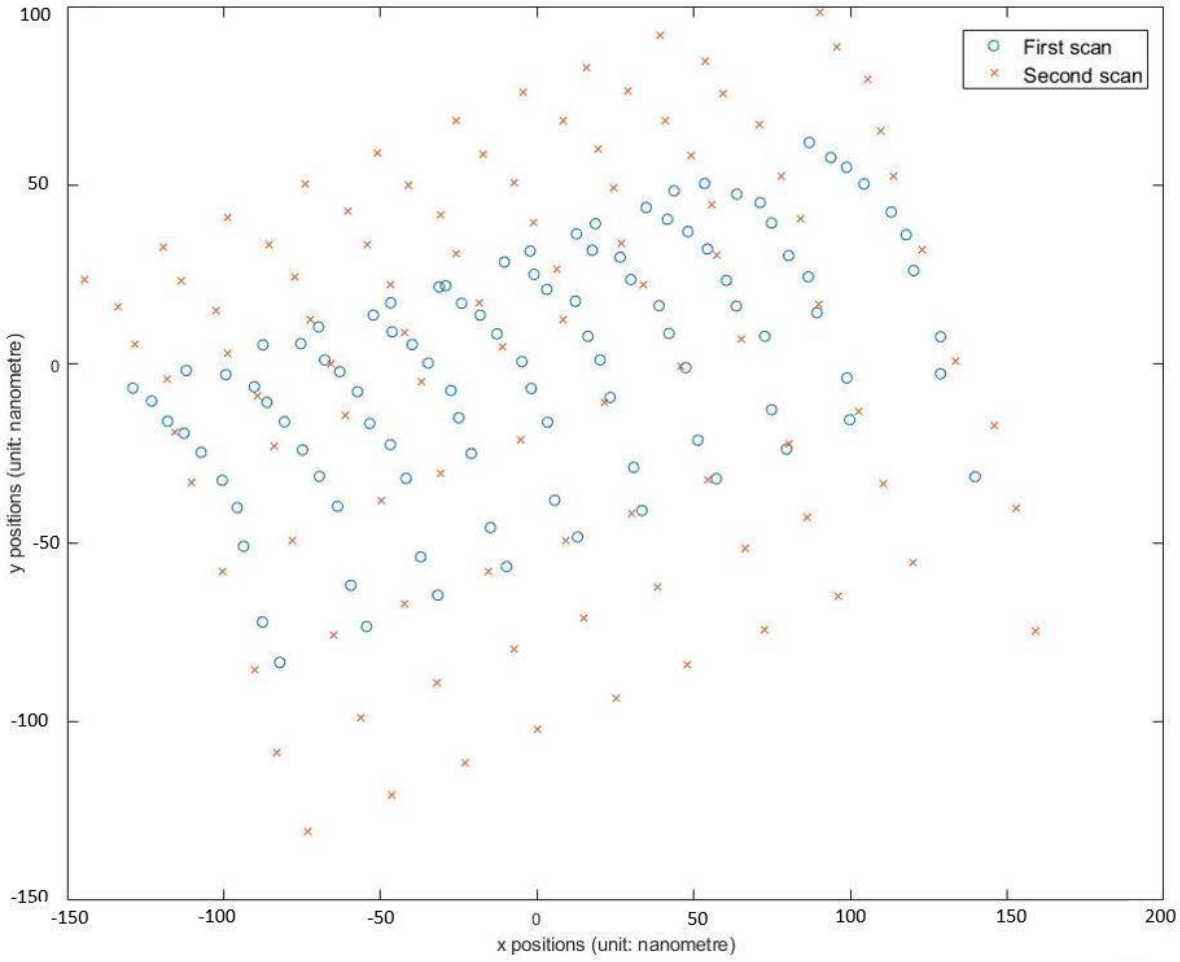

Fig 5.3 The reproduced scan positions from two datasets using the piezo stage under the same experimental conditions. Note that all the diffraction patterns are centred before the cross-correlation.

The assigned step sizes for both datasets are 40 nm. The positions are plotted in the unit of nanometres. The step sizes in the y-direction in the first scan, represented by 'o', are

significantly shorter than the assigned value. The first 8 rows have step sizes in the y-direction around 7 nm. The bottom 2 rows have step sizes in the y-direction around 12 nm, still much lower than the assigned value. The step sizes in the x-direction are more regular, with an average value of 26 nm. The positions from the second scan are more reliable than the first scan. However, stage hysteresis is observed in the y-direction, especially in the top 5 rows, with an average value of 13 nm. This effect is gradually reduced as the scan proceeds. The bottom 5 rows have an average step size in y-direction of 25 nm.

5.1.3 The results and analysis.

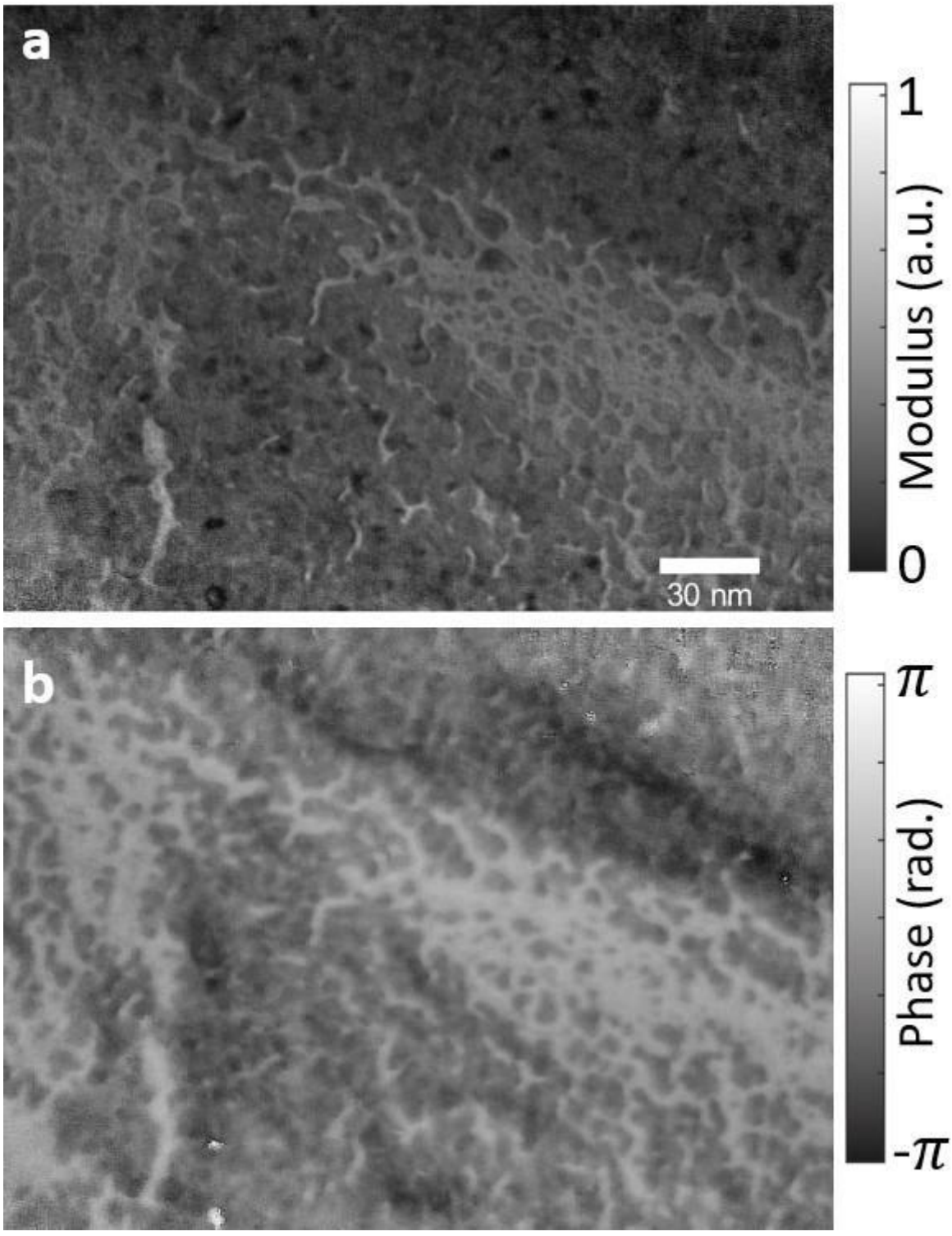

Fig 5.4. The reconstructed object modulus (a) and phase (b) images from the first dataset (bad scan).

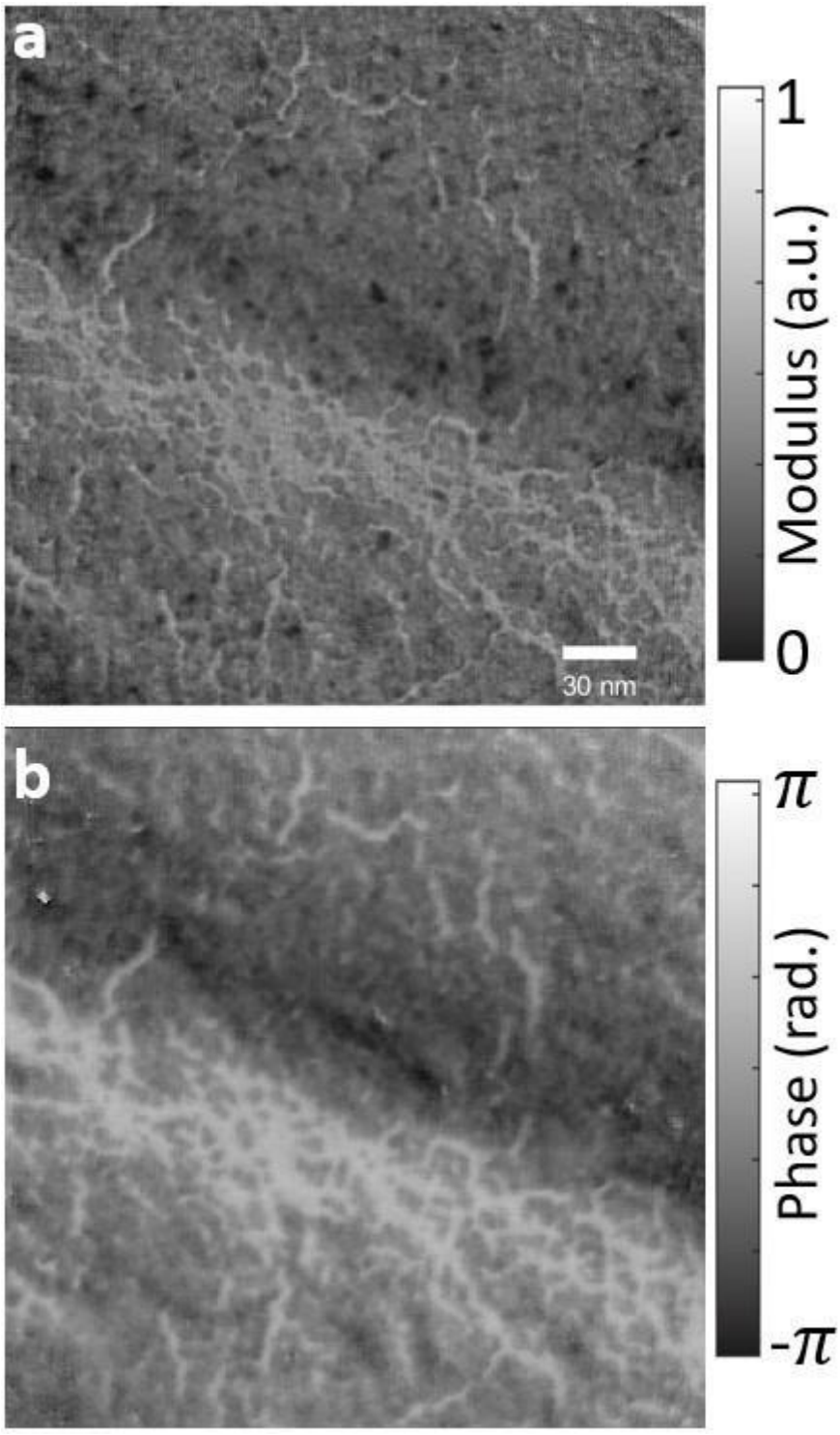

Fig 5.5. The reconstructed object modulus (a) and phase (b) images from the second dataset (good scan).

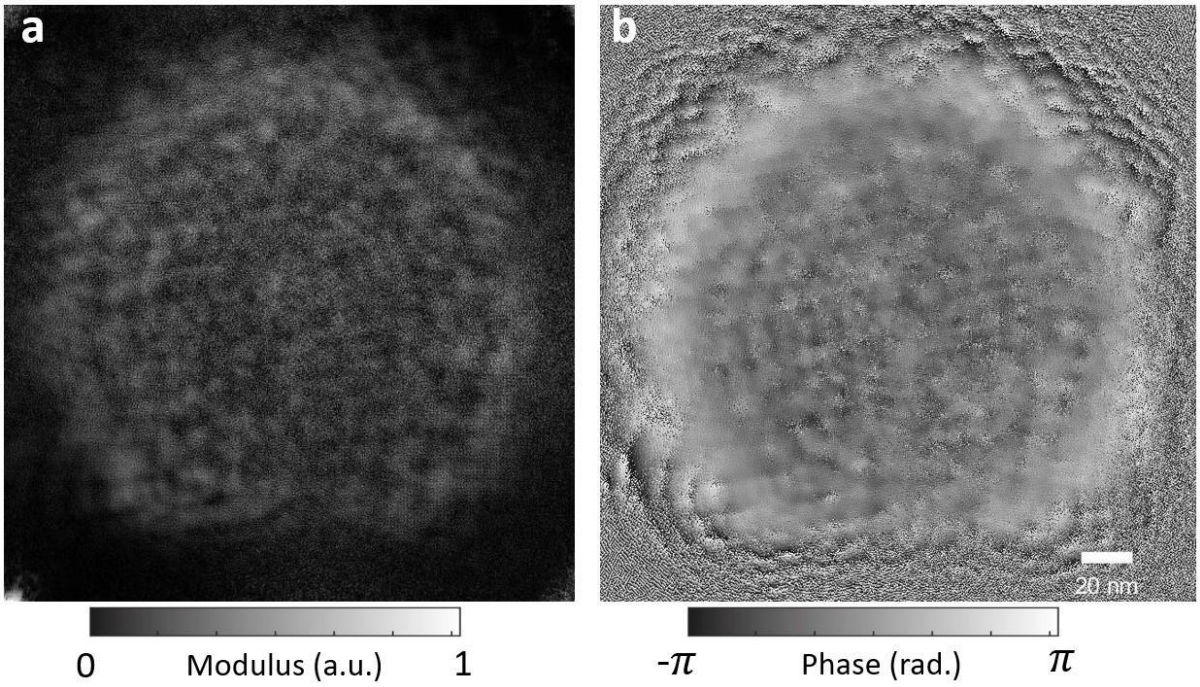

Fig 5.6. The reconstructed probe modulus (a) and phase (b) images from the first dataset (bad scan).

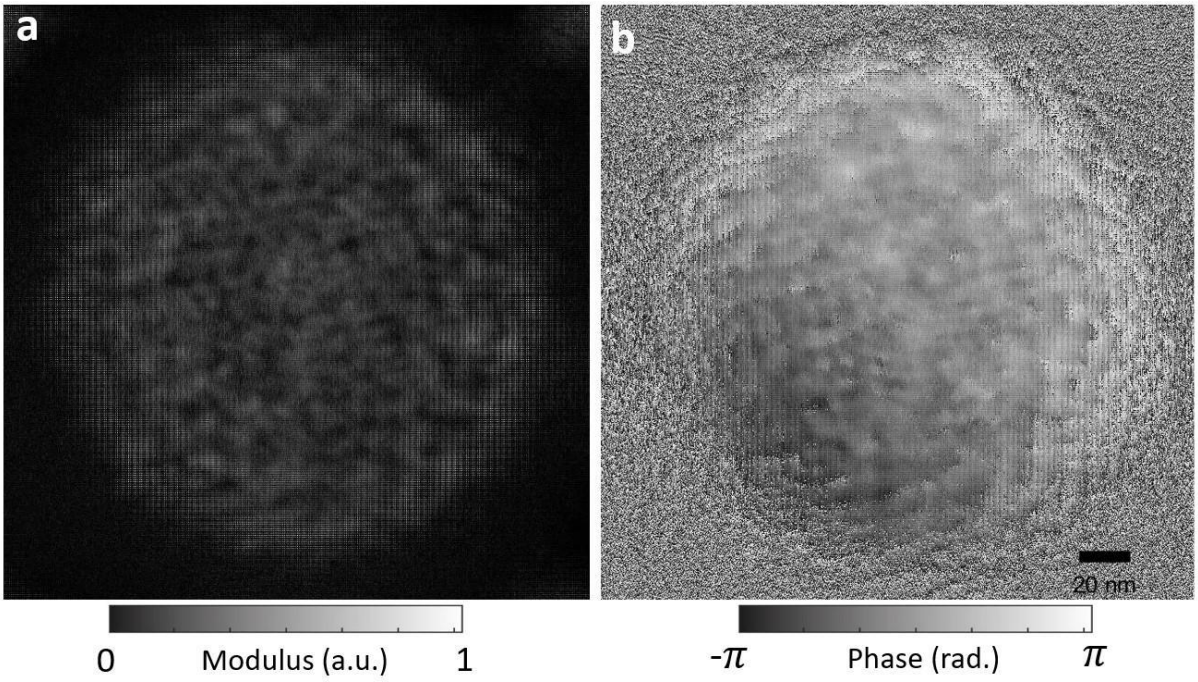

Fig 5.7. The reconstructed probe modulus (a) and phase (b) images from the second dataset (good scan).

Due to the imperfect step sizes, the scan area in the first dataset is rectangular, as shown in Fig 5.4. Fortunately, the cross-correlation successfully reproduces the scan positions under

such high magnification. However, the resolution of our reconstruction results, determined using FRC, is around 2 nm, as shown in Fig 5.8.

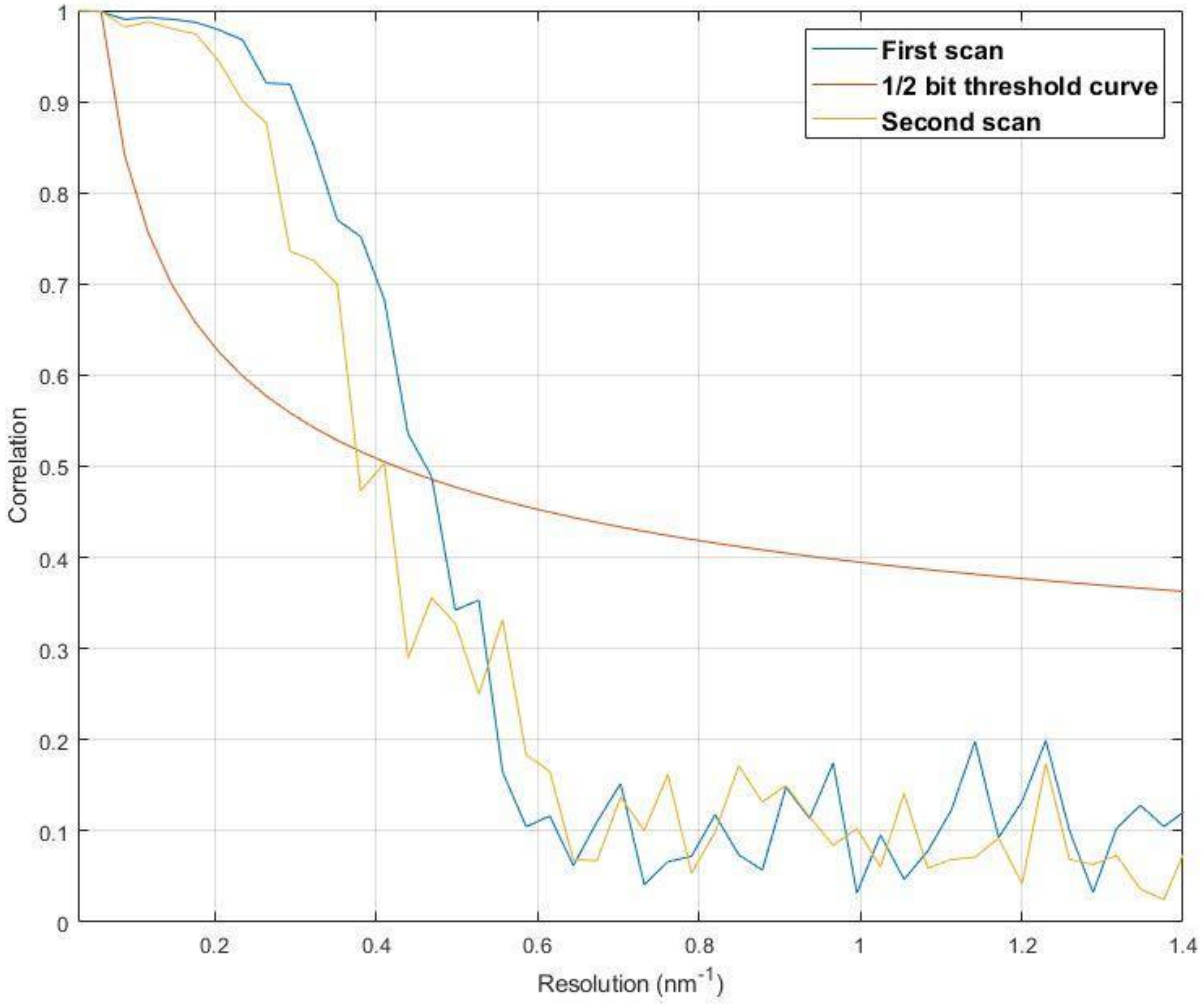

Fig 5.8. The Fourier Ring Correlation analysis of two datasets. The first dataset intersects the half-bit curve at a frequency of 0.4685 nm^{-1}, corresponding to a resolution of 2.13 nm. The first dataset intersects the half-bit curve at a frequency of 0.3806 nm^{-1}, corresponding to a resolution of 2.62 nm.

The resultant resolution is approximately 20 times larger than the image pixel sizes (1.13Å). Although the results are far from reaching the atomic resolution, these experiments provide valuable feedback for further work. The first is that under such high magnification, the cross-correlation can still reproduce the scan positions. The tiny gold features in our sample are blurred, but the scanned region is uniform. In other words, the image contrast of the diffraction patterns is constant, unlike the permalloy datasets. This constant image contrast helped the cross-correlation to trace the trajectory of those highly magnified features and

reproduce the scan positions. This means the physical size of the illumination profile can be even smaller, producing a smaller image pixel size.

The second is the method of translating the sample. In our setup, the piezo stage movement distance is set to be 400 nm in both directions, and the actual movement distance is even smaller. This means the beam-shifting method could be considered for future experiments. Previously in Chapters 3 and 4, the relative shifting distance between the sample and the illumination probe was as large as 4 μm, a value much larger than the maximum reliable range of the beam shifting method. In the experiments that pursue the atomic resolution, the requirement for the physical size of the illumination probe is much smaller, meaning the corresponding total scan distance is much smaller, a value possibly within the maximum reliable range of the beam shifting.

Another method to improve the spatial resolution is to increase the pixel sizes of the diffraction patterns. The Gatan K2 detector (model number 1000) used in our experiment has a pixel number of 3840 x 3712. And our diffraction patterns are cut out to be 2048 x 2048 pixels. The diffraction patterns are cut for less storage space and quicker reconstruction. In future experiments, the whole detector can be used without cutting it out. The bright field disk can be magnified more and occupy a larger area. With the same bright field disk occupying more pixels, each pixel will represent a smaller physical area, meaning a smaller image pixel size.

5.2 Near-field electron ptychography under low voltage.

The performance of conventional far-field electron ptychography at low-dose conditions has been well-explored (Pelz, Qiu et al. 2017, Zhou, Song et al. 2020). The combination of cryo-electron microscopy and far-field ptychography is able to reproduce a complex image of the HIV virus at a nanometre scale at a dose of 5.7e/Å² (Zhou, Song et al. 2020). In near-field electron ptychography, due to the required long exposure time, ranging from 0.1s to 0.5s, the performance at low dose conditions has not been discussed. In this section, we make the first step toward exploring this limitation by tuning down the acceleration voltage from 300 kev to 80 kev . Two experiments are conducted: the first one examines the familiar latex sphere

sample, and the second one examines a bio-material sample, a rat brain. This section is arranged as follows: the experimental condition is described in section 5.2.1, and the results and analysis are presented in section 5.2.2.

5.2.1 The experimental condition

The experiments are conducted on probe-corrected FEI Titan G2 80-200 ChemiSTEM at Ernst-Ruska Centre, Forschungszentrum Juelich GmbH, Germany. The microscope was operated at 80 keV with spot size 3 in conventional TEM mode. The microscope is equipped with a Model 994 UltraScan 1000XP detector with 2048 x 2048 pixels on a 14 µm pixel pitch. The sample was translated using the stepper motor stages on the sample holder, programmed via Digital Micrograph scripts. Each dataset is full-frame 2048 x 2048 pixels and binned 2. This means the diffraction patterns are 1024 x 1024 pixels with a pixel size of 28 µm. The exposure times were 0.1s with the latex sphere sample and bio-material sample.

Two datasets were collected using the latex sphere as the sample. The size of the illumination probe was 1 µm in the first dataset, and 2 µm in the second dataset. The microscope lenses were adjusted to a defocus of 180 µm and a magnification of 25974 for the 1 µm experiment, and a defocus of 380 µm and a magnification of 12627 for the 2 µm experiment. The sample was scanned in a raster fashion through a grid of 10 × 10 positions with a step size of 20% of the corresponding illumination diameter.

The second experiment used a slice of a rat brain as the sample. For a more accurate initial guess of the defocus and magnification value, the experimental conditions are the same as the 2 µm illumination latex sphere experiment. However, during the collection process of this dataset, due to some technique issues, the beam was blanked at the 90^{th} diffraction pattern. Hence, only the first 90 diffraction patterns are used in the reconstruction.

Similar to experiments reported in previous chapters, the diffraction patterns drifted during the collection process. Fortunately, all of the bright field disks are fully inside the frame. The diffraction patterns are centred before the reconstruction, as shown in Fig 5.9.

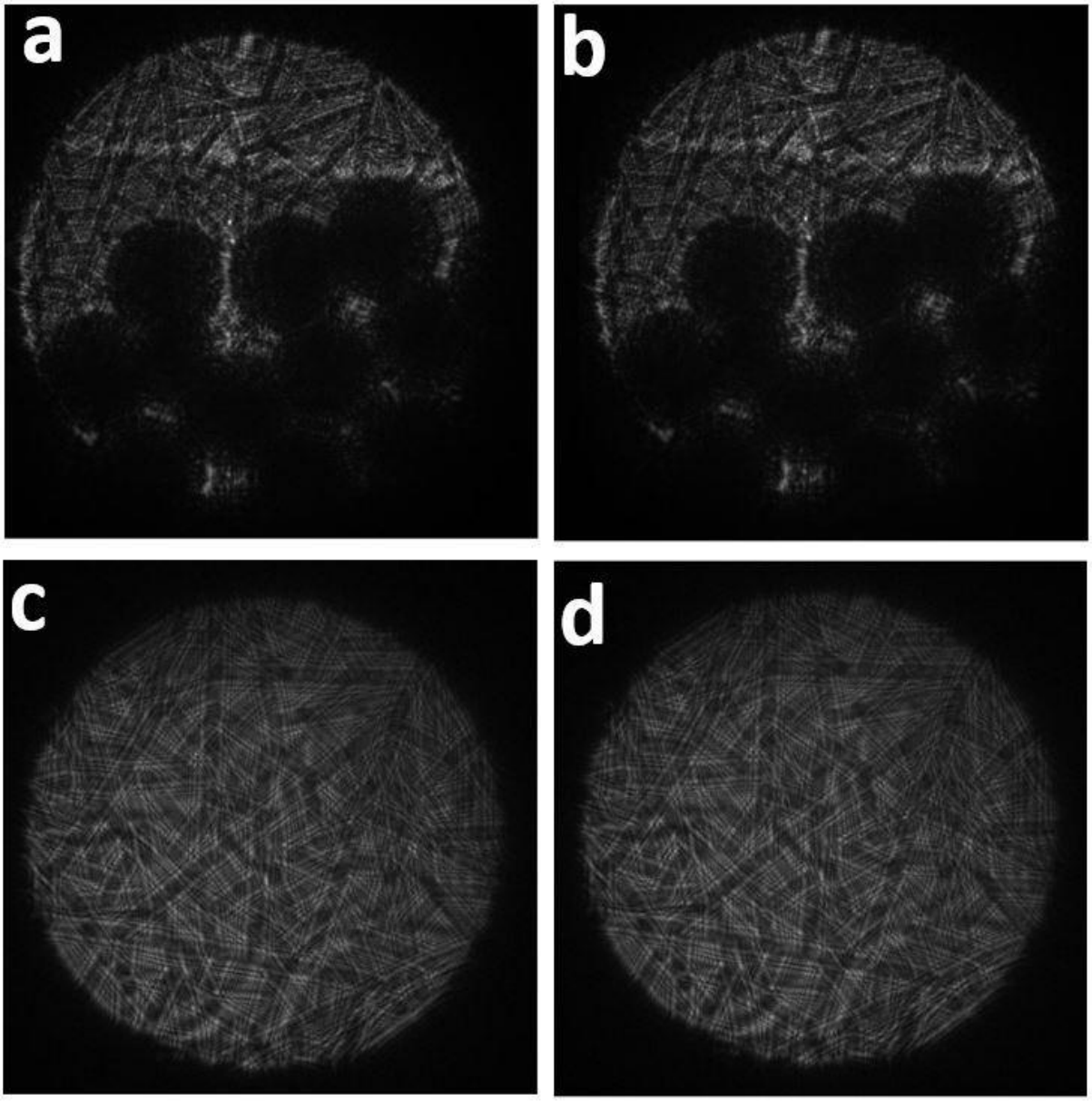

Fig 5.9. The raw diffraction patterns (a) and (c), and the corresponding drift-corrected diffraction patterns (b) and (d). (a) is from the 1 µm illumination diameter latex sphere dataset. (c) is from the second experiment with the bio-material sample.

5.2.2 The results and analysis

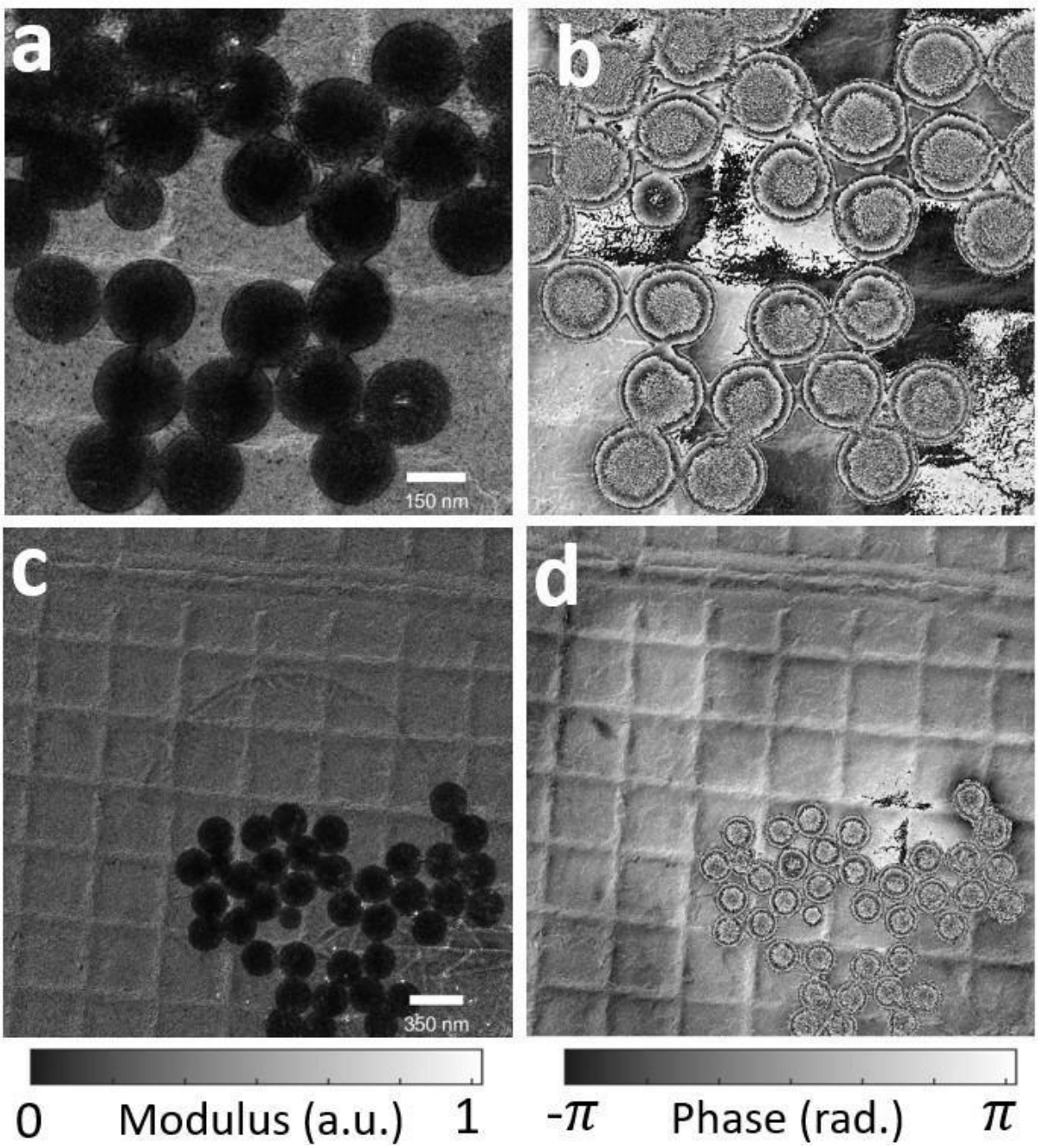

Fig 5.10. The reconstructed object. (a) and (b) are the modulus and phase reconstruction with a 1 μm-diameter illumination probe. (c) and (d) are the modulus and phase reconstruction with a 2 μm-diameter illumination probe.

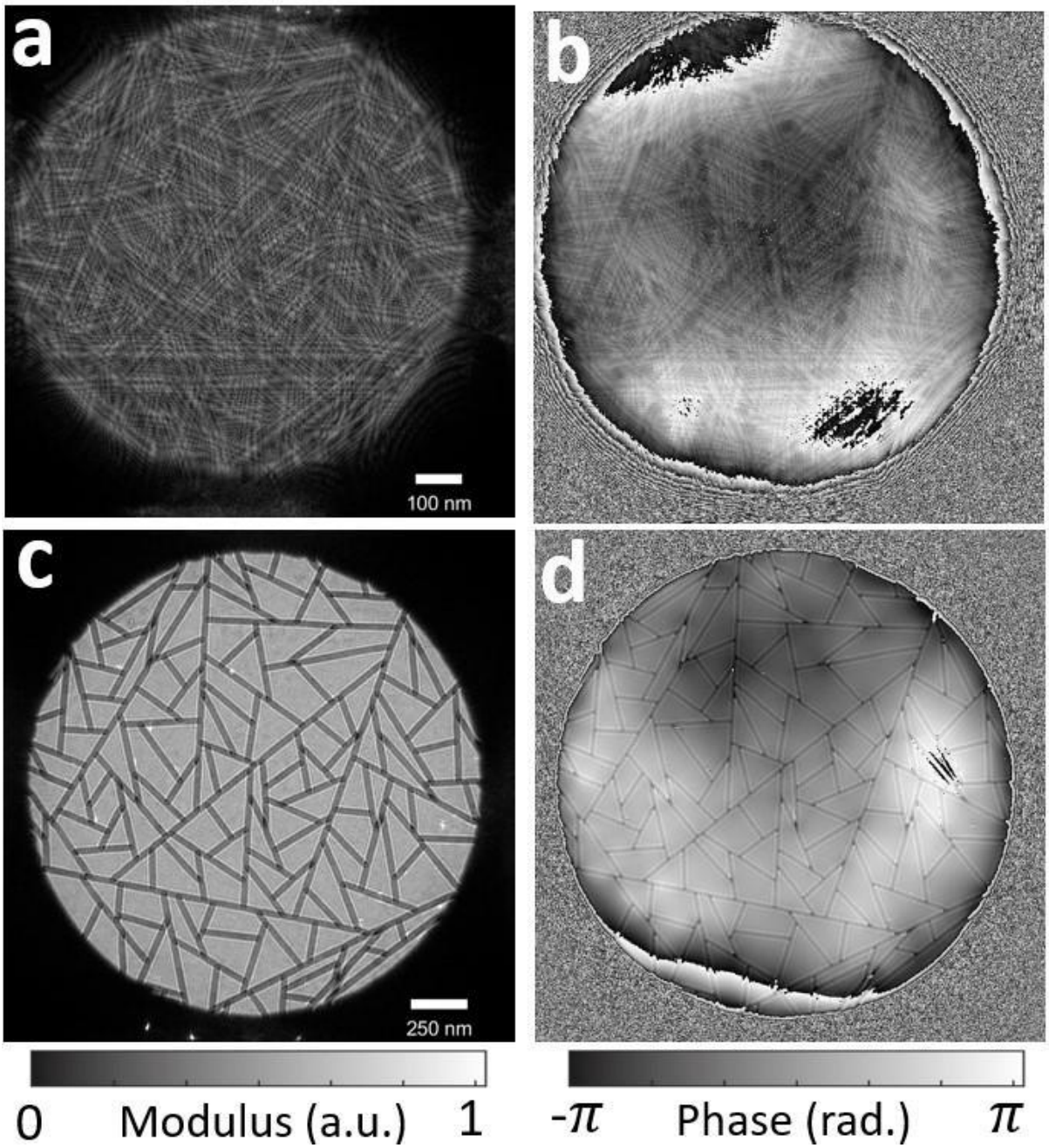

Fig 5.11. The reconstructed probe. (a) and (b) are the modulus and phase reconstruction with a diameter of 1 µm. (c) and (d) are the modulus and phase reconstruction with a diameter of 2 µm.

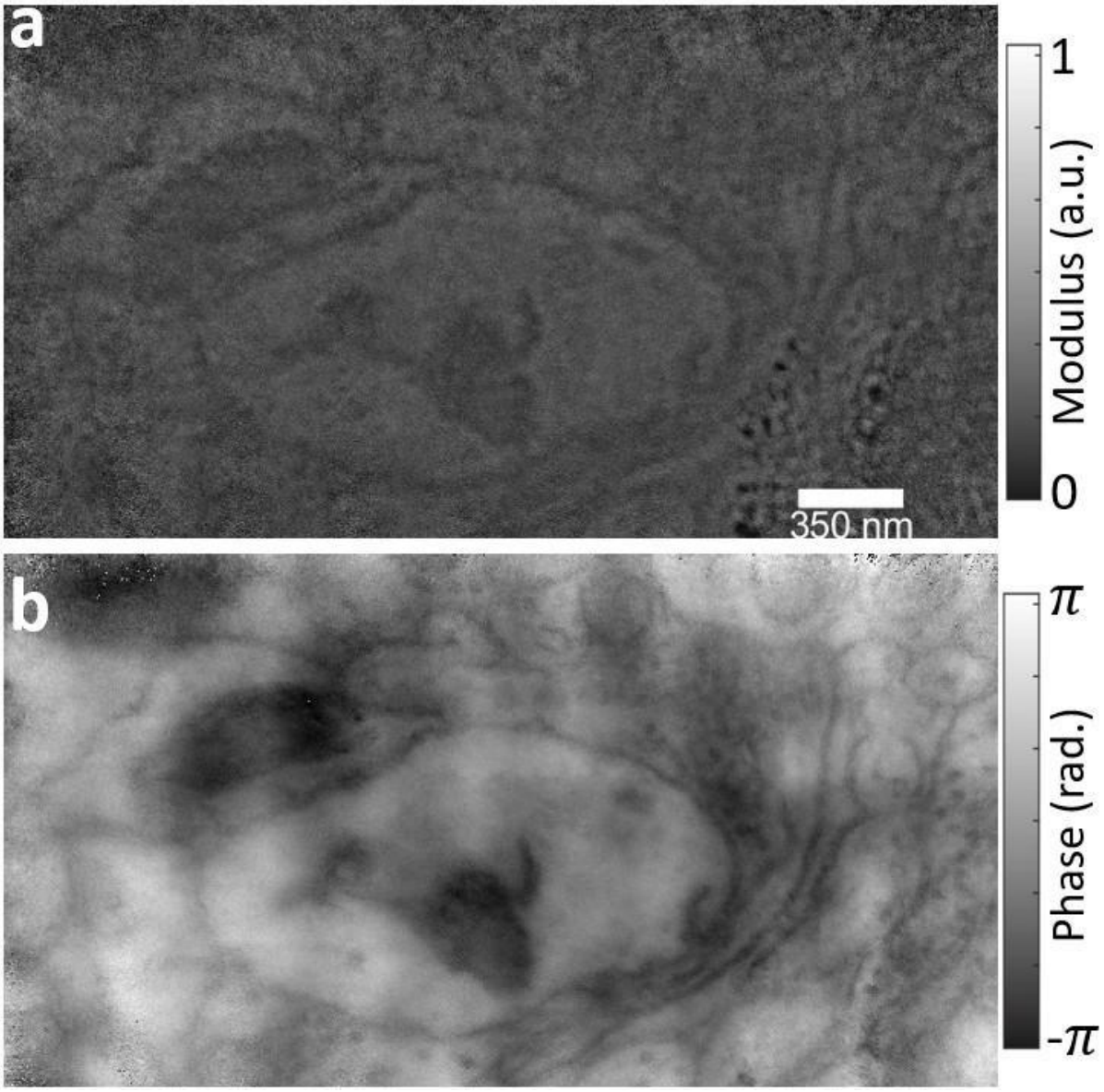

Fig 5.12. The object reconstruction with a slice of rat brain as the sample. (a) is the modulus reconstruction, and (b) is the phase reconstruction.

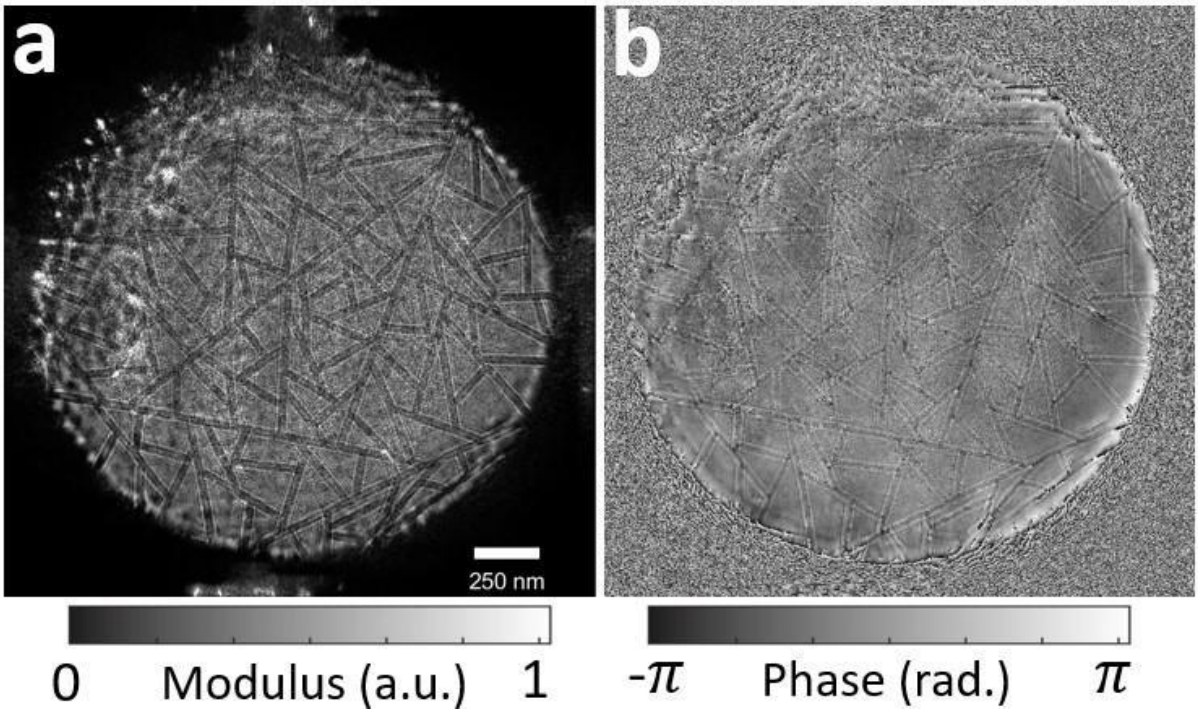

Fig 5.13. The reconstructed probe was used in the rat brain experiment. (a) is the modulus reconstruction, and (b) is the phase reconstruction.

The results shown in Fig 5.9-13 are preliminary results. Due to the limited time, the diffraction patterns are centred using the algorithm. As explained in Chapter 4, the manual centring process is much more time-consuming than the program-centring process. All the diffraction patterns in each dataset need to be centred one by one. This process is usually required to be repeated more than once. The program-centring process, although sacrificing accuracy, can finish the entire dataset in a few seconds. As a result, the object phase reconstruction of the 1 µm illumination, shown in Fig 5.10 (b), has unwanted phase wraps. The corresponding probe, shown in Fig 5.11 (a) and (b), is drifting towards the top left direction, compensating the error from the diffraction patterns. The diffraction pattern drifting problem is less severe, leading to a more uniform object phase reconstruction. Although some phase ramps are present in the middle, as shown in Fig 5.10 (d).

From the object reconstruction, the latex sphere, with a thickness of 264 nm, is too thick for an electron beam with an acceleration voltage of 80 kev. In experiments with 300 kev, the latex sphere is more transparent, such as the results in Fig 4.14. With the lower acceleration voltage, the electron beam is absorbed, and the reconstructed latex spheres appear darker.

The slice of the rat brain sample, with a thickness of 40 nm, is successfully reconstructed. The cells and organs can be identified from the phase reconstruction. The diffraction patterns in this dataset are not well centred. This can be proved by the fringes in the object phase reconstruction.

The first problem with our reconstruction results is the low image contrast, in both the latex sphere sample and the biological sample. For experiments under low voltage or low dose conditions, the number of electrons exposed onto the specimen should be carefully controlled, especially for the fragile specimen. Hence, to improve the image contrast, the best way is to control the noise level. From the experiment point of view, an electron source with better coherence, and more optimal combination of the exposure time and the beam current can be considered. From the reconstruction point of view, a more efficient way to decouple the inelastic scattering from the reconstructed results can be used to further improve the image contrast. Our current experimental condition is capable of imaging specimens with thickness of 40nm. For the latex sphere sample with thickness over 260nm, the detail of the latex sphere is lost. Hence, in the future experiment, the sample thickness should also be carefully selected.

Chapter 6. Conclusion and future work

This chapter summarises the three experiments in section 6.1 and discusses two possible future applications of near-field electron ptychography in section 6.2. This thesis is concluded in section 6.2.

6.1 Conclusion

This thesis demonstrated proof of the principle of the technique, by inserting an amplitude diffuser at the condenser lens aperture, near-field electron ptychography can recover the complex transfer functions of both the sample and illumination probe using variable illumination sizes. In Chapter 3, we demonstrated by tuning the strength of the lenses, variable illumination sizes can be created with the same amplitude diffuser. With the electron beam only passing through the region of interest, the use of electrons was more efficient, and the sample suffered from less beam damage than the previous near-field electron ptychography implementation (Allars, Lu et al. 2021). The sample was translated by shifting the sample stage, and such scan position was reproduced by the cross-correlation. Using a modified version of the 'ePIE' algorithm (Maiden, Sarahan et al. 2015), the complex values of both the sample and illumination probe were accurately recovered from three individual experiments with different illumination probe sizes. With a 10 by 10 raster scan, the field of view in our experiment was as large as 6 μm^2.

In Chapter 4, we expanded our design to fit into the Lorentz mode. The objective lens was turned off to preserve the intrinsic magnetic feature of the sample. To demonstrate that the variable illumination size could be achieved in this new configuration, two experiments with different illumination probe sizes were conducted, with the non-magnetic sample. The magnetic sample was examined under the largest illumination size, 2 μm. The challenge in these experiments was to reproduce the scan positions. Due to rapid image contrast changes, the cross-correlation could not find a reference point to correctly calculate the scan step sizes. Two measures were taken to improve the situation. The first method was to pre-define the step sizes and prevent the cross-correlation from confusing other features that were in the wrong areas as the reference point. The second was the stage training method. The sample stage moves in a more regular pattern after the first two data collections. Hence, the latex sphere sample, whose scan positions could be easily reproduced, was scanned four times. Then, the magnetic sample was scanned four times under the same experimental conditions. The reproduced scan positions from the fourth scan of the latex sphere dataset could be used as the scan positions of the magnetic dataset at the fourth scan. To ensure the accuracy of our reconstruction, the same magnetic sample was also reconstructed using off-axis holography. The results from ptychography and holography showed high similarity.

In Chapter 5, we explored the performance of near-field electron ptychography under limiting conditions in conventional TEM mode. The first attempt was to achieve the atomic resolution. With a small illumination probe size and piezo stage to translate the sample, the best resolution we achieved was 2 nm. In the second experiment, we successfully recovered a biological sample, a slice of rat brain, under 80 keV.

6.2 Future work

Some datasets were not nicely reconstructed due to the limited time. One example is the NdFeB hard magnetic sample under Lorentz mode. This dataset was collected with the same condition of Mo-doped permalloy described in Chapter 4. The preliminary reconstructed sample results are shown in Fig 6.1.

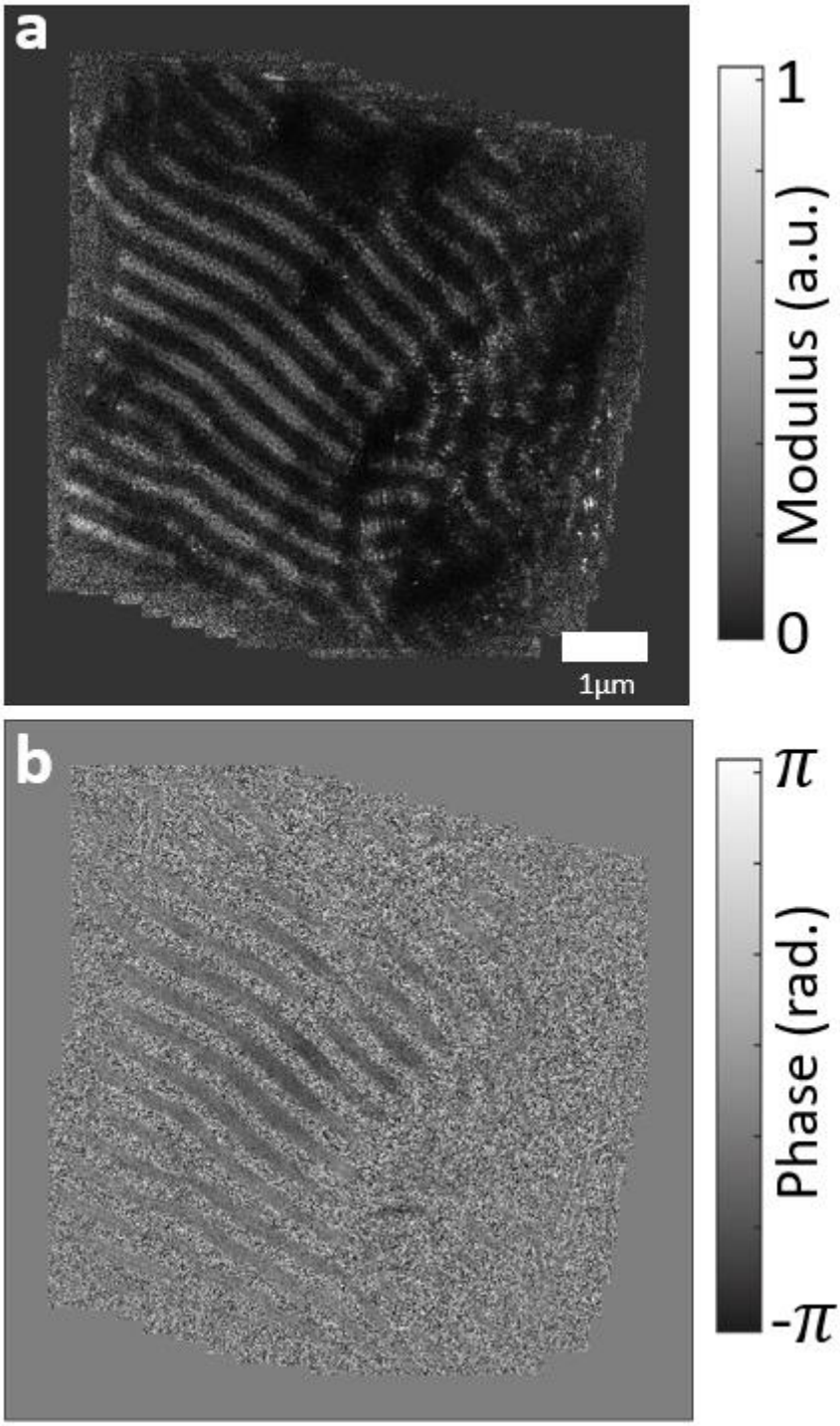

Fig 6.1. The preliminary reconstruction of NdFeB hard magnetic sample in Lorentz mode. (a) is the modulus image, and (b) is the phase image.

The main challenge with this dataset is to correct the drifting problem of the diffraction patterns. The edge of the diffraction pattens were difficult to determine due to the irregular shape of the sample, one example is shown in Fig 6.2.

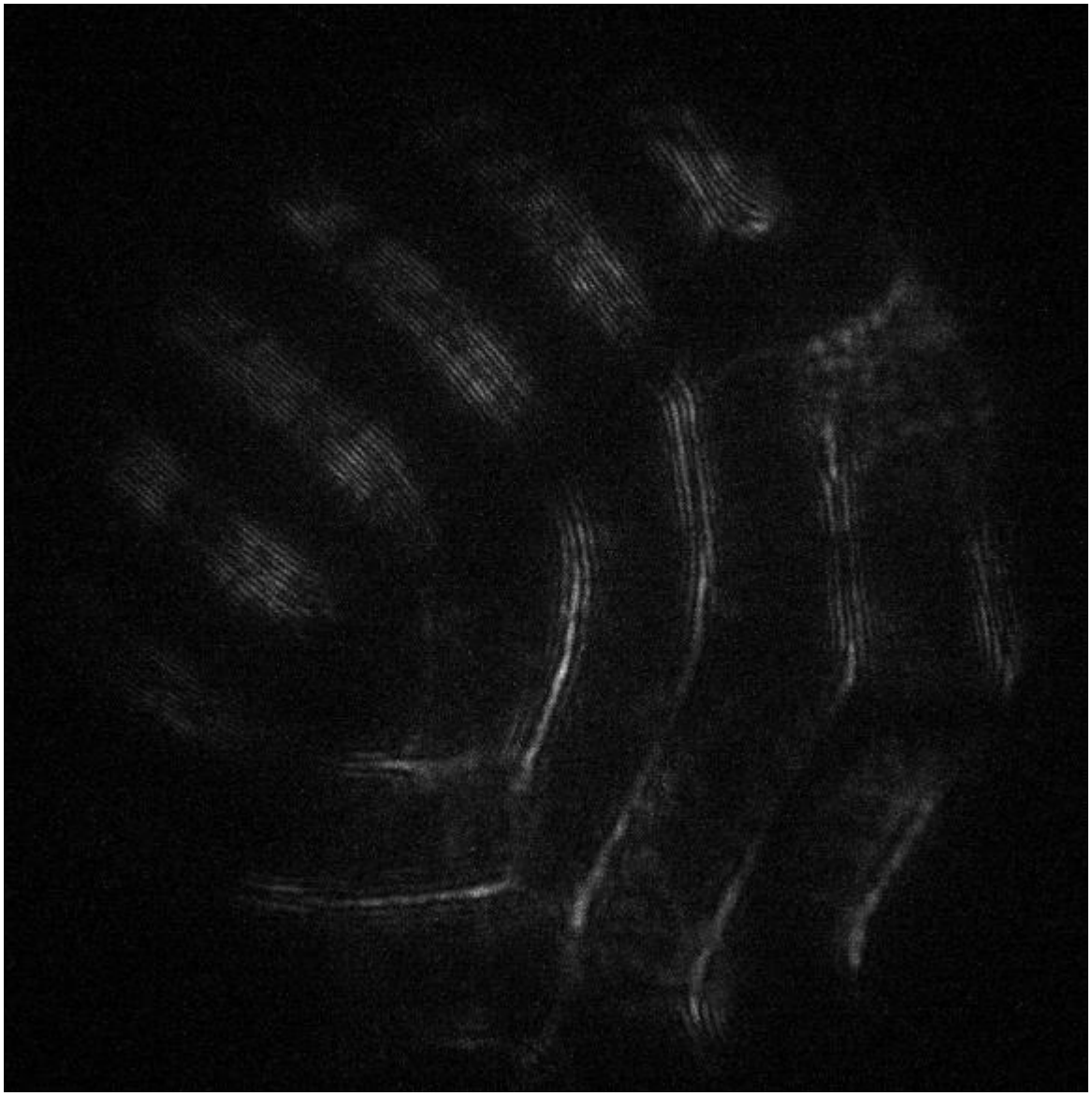

Fig 6.2. One typical diffraction pattern of NdFeB sample. The bright field disk drifted towards the bottom right direction. The gap between the magnet had the same image contrast with the background. Hence, the edge of the bright field disk was difficult to determine.

Without completely correcting the drifting problem, the reproduced scan position grid has unavoidable error. To solve this problem, one possible solution is to seek topological approach. For example, find three points that is most likely to be the edge of the bright field disk, and determine the centre of the bright field disk using these three points. And this process can be repeated using three different points and determine the centre again and check whether the two determined centres are close enough. However, this approach requires to manually analysis each diffraction pattern. Such process is very time-consuming.

Besides near-field electron ptychography, some far-field electron ptychography experiments were conducted during the early period of my PhD. The experiments were to explore the low-dose atomic-resolution STEM ptychography. The sample was monolayer and twisted bilayer Molybdenum Disulfide (MoS_2). The acceleration voltage was 80 kev, meaning the electron wavelength was 4.18pm. The convergence semi-angle was 17.7mrad. The diffraction limited resolution in this condition, using the equation 2.15 in Chapter 2, is 1.4Å. The defocus is 35nm with a probe size of 1.2nm. The detector was Electron Microscope Pixel Array Detector (EMPAD), a high dynamic range direct electron detector from Thermo Fisher. The sample was translated using a raster fashion scan with 128 x 128 points, with each diffraction pattern of 256 x 256 pixels. Six datasets were collected with different scanning step size and electron dose, as shown in Table 6.1.

Data	Probe current	Scanning step size	Ratio of step size over probe size	Dose
GL3_5.1MX_95p	99pA	1Å	8%	$62 \times 10^3 \ \frac{e}{Å^2}$
GL3_2.55MX_95p	99pA	2Å	17%	$15 \times 10^3 \ \frac{e}{Å^2}$
GL3_1.8MX_90p	99pA	3Å	25%	$6.9 \times 10^3 \ \frac{e}{Å^2}$
GL8_5.1MX_95p	9pA	1Å	8%	$5.6 \times 10^3 \ \frac{e}{Å^2}$
GL8_2.55MX_95p	9pA	2Å	17%	$1.4 \times 10^3 \ \frac{e}{Å^2}$
GL8_1.8MX_90p	9pA	3Å	25%	$0.6 \times 10^3 \ \frac{e}{Å^2}$

Table 6.1. Six datasets of low-dose atomic-resolution STEM ptychography. 'GL3' means gun lens 3, determining probe current. '5.1MX_95p' means the magnification and scanning pixel numbers, determining scanning step size.

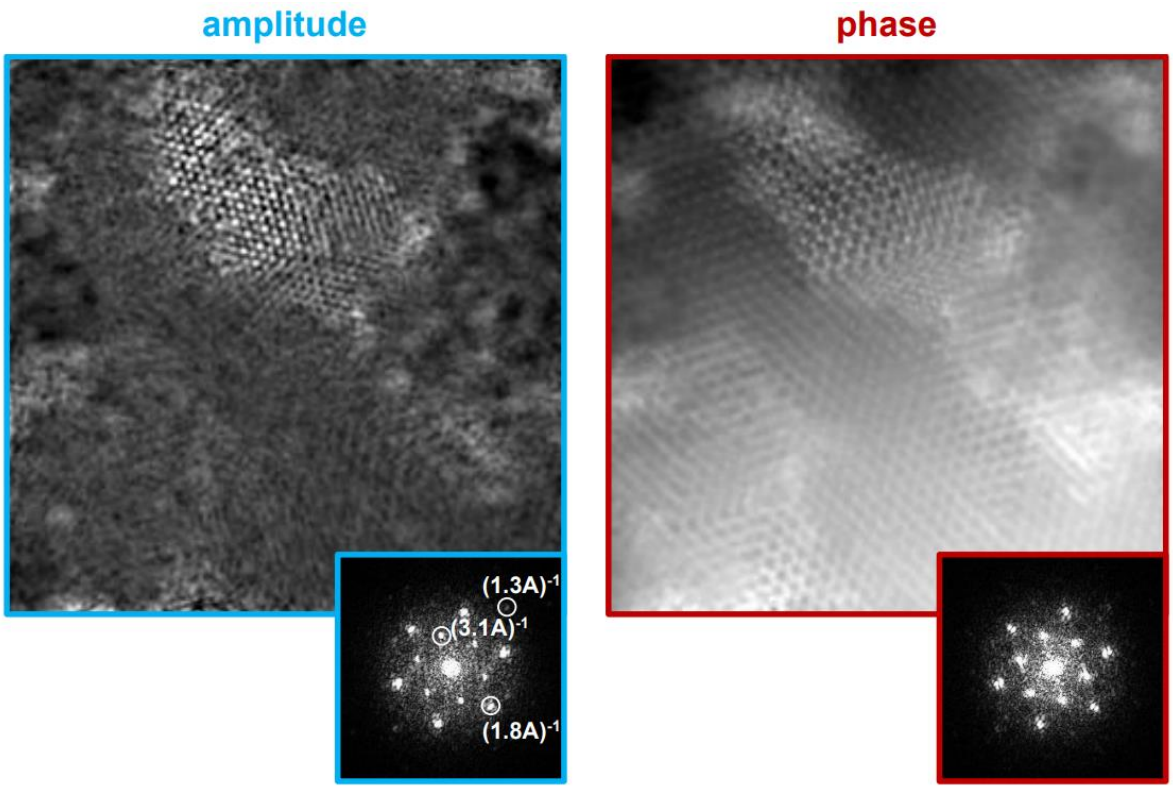

*Fig 6.3. Dataset 'GL3_5.1MX_95p', step size is **1 Å** (**8%** of the probe size), and dose **62x10³ e/ Å²**. The bottom right blue and red circled images are the diffractogram of the modulus and phase reconstruction respectively, the circulated diffraction spot corresponds to a **1.3 Å** (best case) distance in real space.*

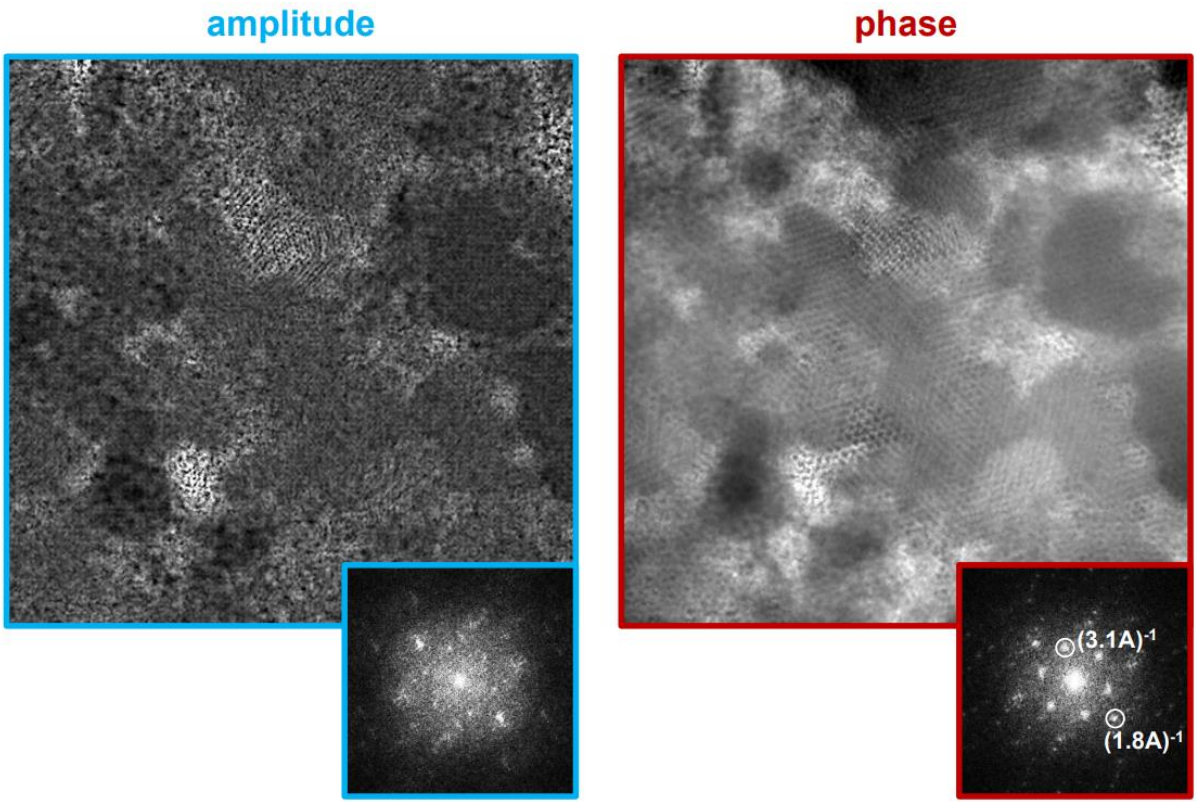

*Fig 6.4. Dataset 'GL3_2.55MX_95p', step size is **2 Å** (**17%** of the probe size), and dose **15x10³ e/ Å²**. The bottom right blue and red circled images are the diffractogram of the modulus and phase reconstruction respectively, the circulated diffraction spot corresponds to a **1.8 Å** (best case) distance in real space.*

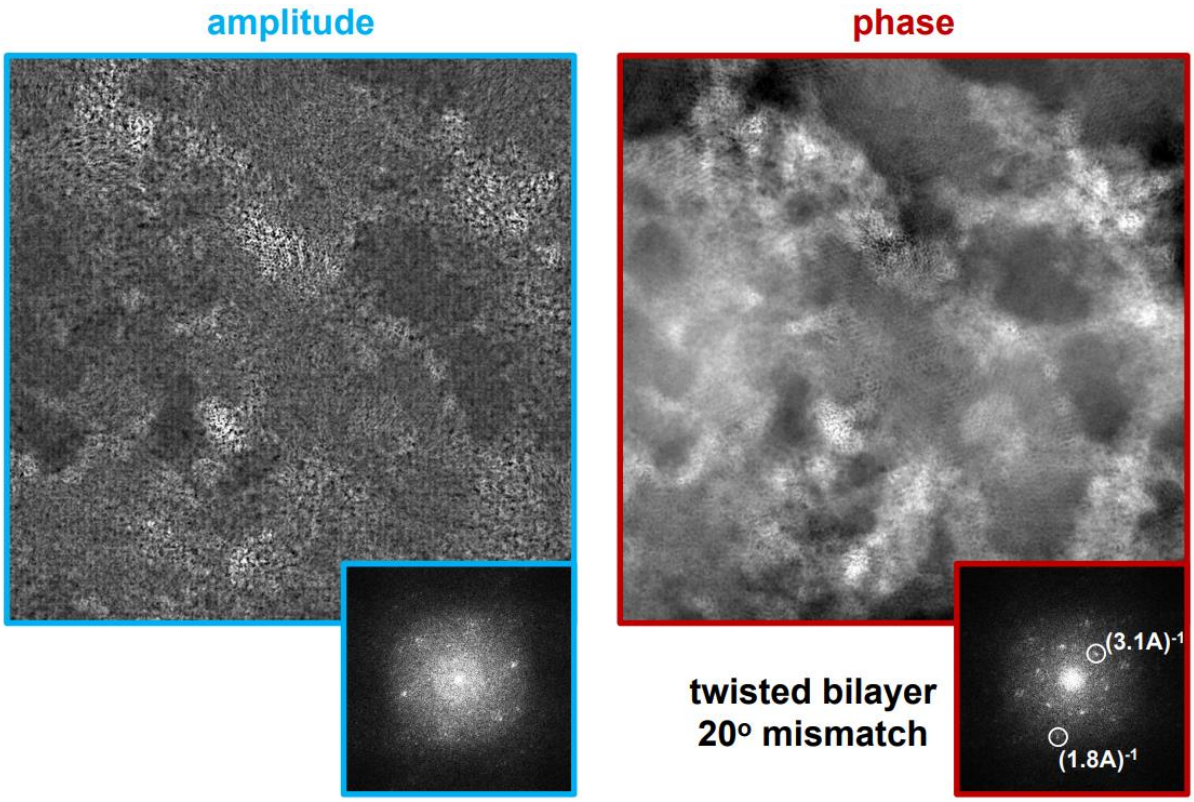

*Fig 6.5. Dataset 'GL3_1.8MX_90p', step size is **3 Å** (**25%** of the probe size), and dose **6.9x10³ e/ Å²**. The bottom right blue and red circled images are the diffractogram of the modulus and phase reconstruction respectively, the circulated diffraction spot corresponds to a **1.8 Å** (best case) distance in real space.*

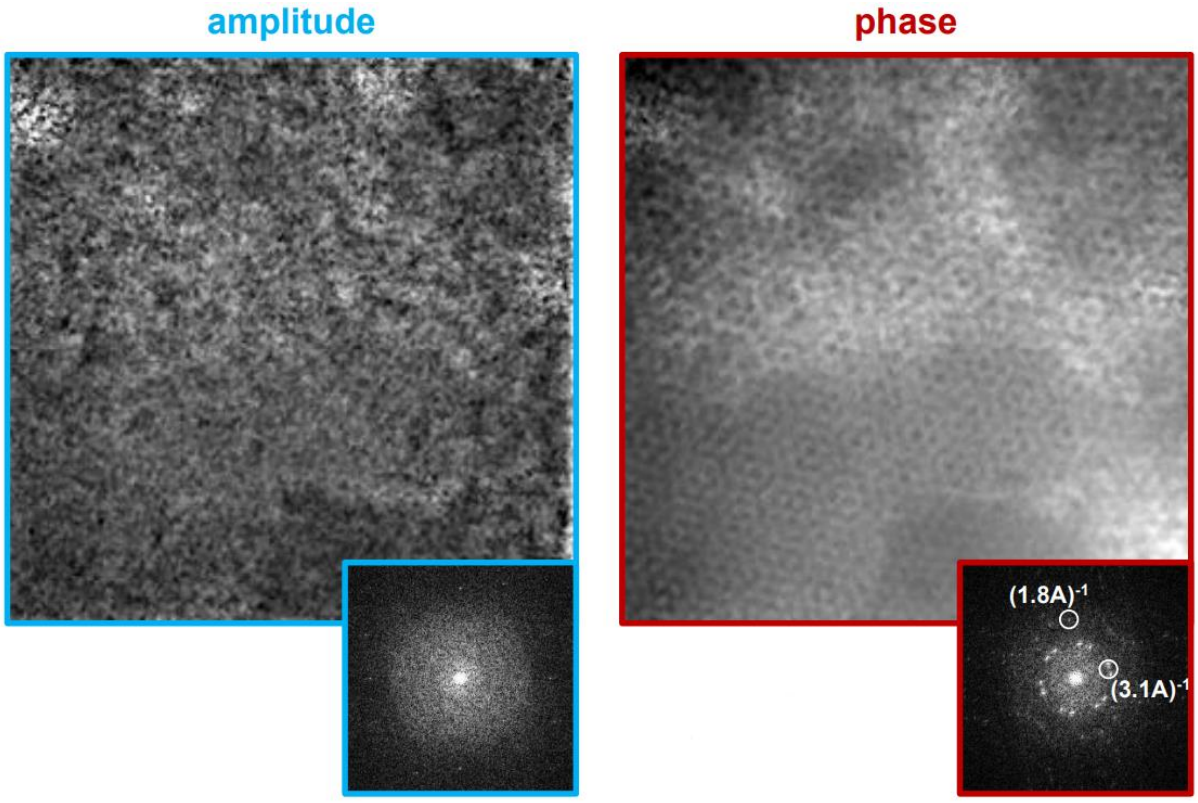

*Fig 6.6. Dataset 'GL8_5.1MX_95p', step size is **1 Å** (**8%** of the probe size), and dose **5.6x10³ e/ Å²**. The bottom right blue and red circled images are the diffractogram of the modulus and phase reconstruction respectively, the circulated diffraction spot corresponds to a **1.8 Å** (best case) distance in real space.*

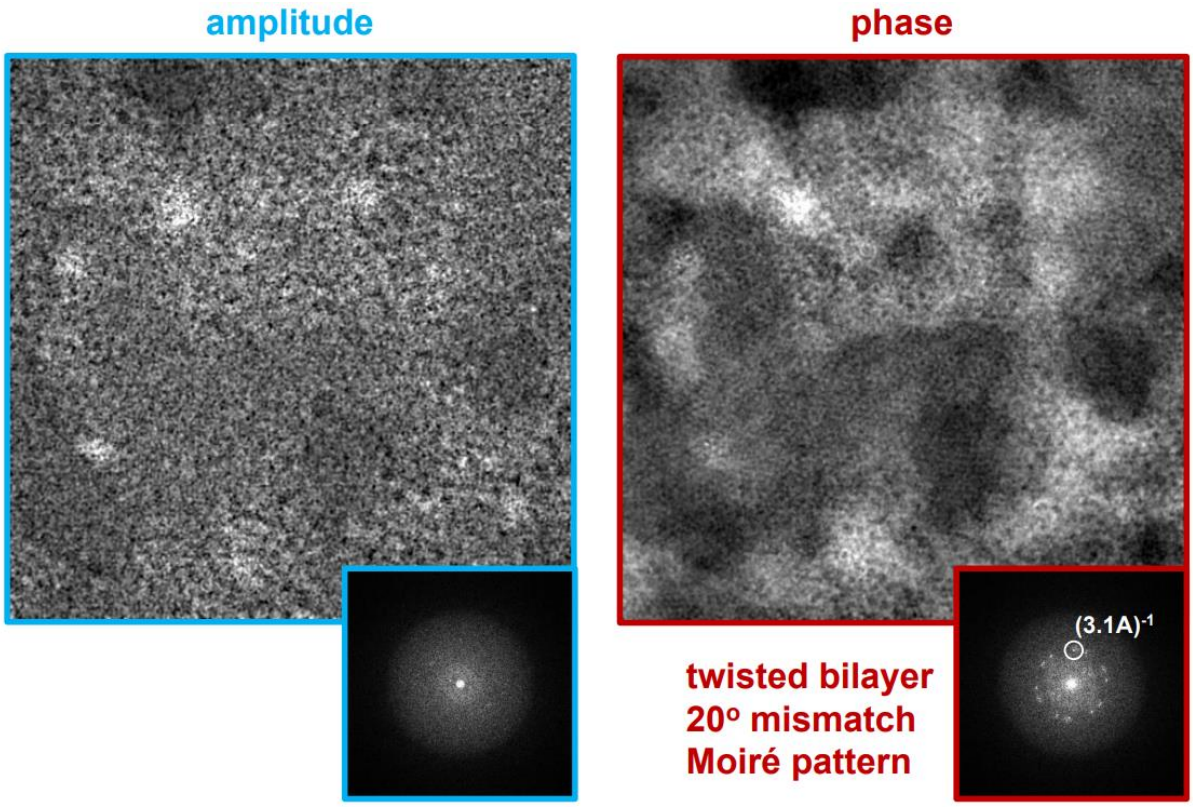

*Fig 6.7. Dataset 'GL8_2.55MX_95p', step size is **2 Å** (**17%** of the probe size), and dose **1.4x10³ e/ Å²**. The bottom right blue and red circled images are the diffractogram of the modulus and phase reconstruction respectively, the circulated diffraction spot corresponds to a **3.1 Å** (best case) distance in real space.*

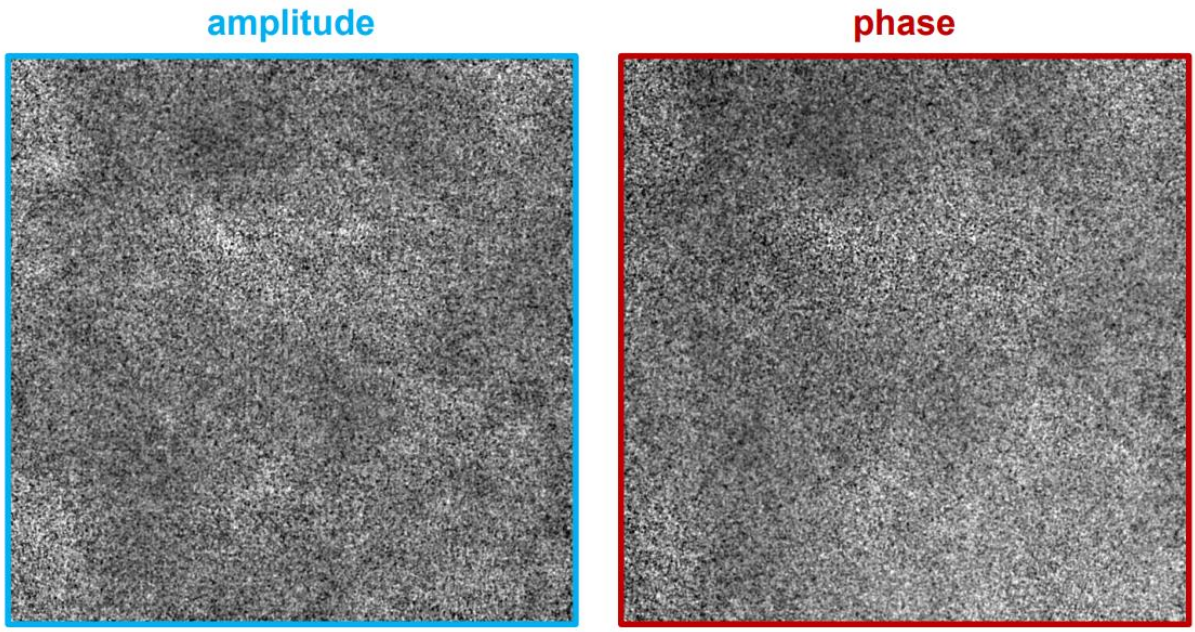

*Fig 6.8. Dataset 'GL8_1.8MX_90p', step size is **3 Å** (**25%** of the probe size), and dose **0.6x10³ e/ Å²**. The reconstruction failed at such an extreme low-dose and large step size condition.*

With the dose as low as $5.6x10^3$ e/ Å², we were able to achieve 1.8 Å resolution. And even with dose of $1.4x10^3$ e/ Å², we still obtain a resolution of 3.1 Å. Clearly in the future we should try to limit the scanning step size smaller than 20% of the probe size, ideally 10% of the probe size, for the low dose datasets, which requires a very small probe current (~1 pA). It is still promising that we will get something useful with a dose budget below $1x10^3$e/ Å², which was demonstrated in (Song, Allen et al. 2019, Chen, Odstrcil et al. 2020).

As for the future of near-field electron ptychography, as a new technique in the electron community, there are many interesting fields that await to be explored. Two main directions are: achieving atomic resolution, and imaging three-dimensional structure.

To achieve atomic resolution, the first challenge is to project a smaller region of interest on the sample onto a larger area on the detector. In Chapter 5, we projected a 200 nm-diameter area on the sample onto an 1800 pixel-diameter bright field disk, with a 5 µm pixel pitch. A smaller region of interest projected onto a larger pixel number means each pixel can represent a smaller physical area. The minimum distance between two distinguishable features is one pixel. Hence, the atomic resolution is possible when each pixel represents a physical area smaller than the atomic resolution dimension, 2 Å. With the illumination size reduced, the step sizes need to be reduced accordingly to guarantee sufficient overlap. Hence, the second challenge is to find a more accurate method to translate the sample. The Piezo stage was used in our attempt to achieve atomic resolution. It has been proved that after careful calibration, the piezo stage can produce reliable and reproducible scan patterns. However, the collection process is still time-consuming, and the diffraction patterns tend to drift during this process. With the total lateral shifting distance reduced, a more common method to translate the sample in far-field ptychography, beam-shifting, can be considered. The beam-shifting is quick and reliable. During this quick collection process, the diffraction patterns drifting problem can be less severe. Another possible method to improve the resultant resolution is to implement the modal decomposition. Modal decomposition separates the electron wave into a set of mutually orthogonal wave-function components that are incoherent with each other. It can compensate for the unavoidable partial coherence from the electron source and improve the image quality. This has been proved to be the case in the far-field electron ptychography (Cao, Li et al. 2016). And it has been combined with

near-field ptychography in the X-ray community (Clare, Stockmar et al. 2015). This combination successfully accounted for the nonuniform response and added additional degrees of freedom to the reconstruction. The effect on the near-field electron ptychography, however, is yet to be explored.

The second promising direction is to image the three-dimensional structures. In the X-ray community, near-field ptychography has been combined with both tomography (Stockmar, Hubert et al. 2015) and multi-slice (Hu, Zhang et al. 2023). Benefiting from the large field of view in each diffraction pattern, near-field ptychography can recover a much larger volume than far-field ptychography with fewer diffraction patterns. Learning from the experiments combining far-field electron ptychography and multi-slice (Gao, Wang et al. 2017, Chen, Shao et al. 2021), the separation distance between slices is related to the convergence of the electron beam. With near-field electron ptychography, however, the electron beam is near-parallel. Hence, the separation distance and number of slices need to be thoroughly simulated.

Shengbo You, September 2023.

Bibliography

Allars, F., et al. (2021). "Efficient large field of view electron phase imaging using near-field electron ptychography with a diffuser." Ultramicroscopy **231**: 113257.

Bates, R. and J. Rodenburg (1989). "Sub-Ångström transmission microscopy: a Fourier transform algorithm for microdiffraction plane intensity information." Ultramicroscopy **31**(3): 303-307.

Bromwich, T., et al. (2006). "Remanent magnetic states and interactions in nano-pillars." Nanotechnology **17**(17): 4367.

Brüche, E. and H. Johannson (1932). "Elektronenoptik und Elektronenmikroskop." Naturwissenschaften **20**(21): 353-358.

Cao, S., et al. (2016). Defocus and probe-position coupling in electron ptychography. European Microscopy Congress 2016: Proceedings, Wiley Online Library: 475-476

Carter, D. B. W. C. B. (2009). Transmission Electron Microscopy A Textbook for Materials Science, springer publication.

Cassidy, C., et al. (2017). "Determination of the mean inner potential of cadmium telluride via electron holography." Applied physics letters **110**(16).163503

Chen, Z., et al. (2021). "Electron ptychography achieves atomic-resolution limits set by lattice vibrations." Science **372**(6544): 826-831.

Chen, Z., et al. (2020). "Mixed-state electron ptychography enables sub-angstrom resolution imaging with picometer precision at low dose." Nature communications **11**(1): 2994.

Chen, Z., et al. (2021). "Three-dimensional imaging of single dopants inside crystals using multislice electron ptychography." Microscopy and Microanalysis **27**(S1): 2146-2148.

Chen, Z., et al. (2022). "Lorentz electron ptychography for imaging magnetic textures beyond the diffraction limit." Nature Nanotechnology **17**(11): 1165-1170.

Clare, R. M., et al. (2015). "Characterization of near-field ptychography." Optics express **23**(15): 19728-19742.

Cloetens, Peter, et al. "Holotomography: Quantitative phase tomography with micrometer resolution using hard synchrotron radiation x rays." Applied physics letters 75.19 (1999): 2912-2914.

D'alfonso, A., et al. (2014). "Deterministic electron ptychography at atomic resolution." Physical Review B **89**(6): 064101.

de Broglie, L. (1925). Research on the theory of quanta. Annales de Physique. (Minkowski Institute Press)

Dominguez, M. S., et al. (2003). "Histological and scanning electron microscopy assessment of various vital pulp-therapy materials." Journal of endodontics **29**(5): 324-333.

Erni, R., et al. (2009). "Atomic-resolution imaging with a sub-50-pm electron probe." Physical review letters **102**(9): 096101.

Gabor, D. (1949). "Microscopy by reconstructed wave-fronts." Proceedings of the Royal Society of London. Series A. Mathematical and Physical Sciences **197**(1051): 454-487.

Gao, S., et al. (2017). "Electron ptychographic microscopy for three-dimensional imaging." Nature communications **8**(1): 163.

Goodman, J. W. (2005). Introduction to Fourier optics, Roberts and Company publishers.

Guizar-Sicairos, M., et al. (2008). "Efficient subpixel image registration algorithms." Optics letters **33**(2): 156-158.

Hegerl, R. and W. Hoppe (1972). "Phase evaluation in generalized diffraction (ptychography)." Proc. Fifth Eur. Cong. Electron Microscopy: 628-629.

Hesse, R., et al. (2015). "Proximal heterogeneous block implicit-explicit method and application to blind ptychographic diffraction imaging." SIAM Journal on Imaging Sciences **8**(1): 426-457.

Hoppe, W. (1969). "Beugung im inhomogenen Primärstrahlwellenfeld. III. Amplituden-und Phasenbestimmung bei unperiodischen Objekten." Acta Crystallographica Section A: Crystal Physics, Diffraction, Theoretical and General Crystallography **25**(4): 508-514.

Hoppe, W. (1982). "Trace structure analysis, ptychography, phase tomography." Ultramicroscopy **10**(3): 187-198.

Hou, L., et al. (2018). "Background-noise reduction for Fourier ptychographic microscopy based on an improved thresholding method." Current Optics and Photonics **2**(2): 165-171.

Hu, Z., et al. (2023). "Near-field multi-slice ptychography: quantitative phase imaging of optically thick samples with visible light and X-rays." Optics express **31**(10): 15791-15809.

Hüe, F., et al. (2011). "Extended ptychography in the transmission electron microscope: Possibilities and limitations." Ultramicroscopy **111**(8): 1117-1123.

Hüe, F., et al. (2010). "Wave-front phase retrieval in transmission electron microscopy via ptychography." Physical Review B **82**(12): 121415.

Jiang, Y., et al. (2018). "Electron ptychography of 2D materials to deep sub-ångström resolution." Nature **559**(7714): 343-349.

Jönsson, C. (1961). "Elektroneninterferenzen an mehreren künstlich hergestellten Feinspalten." Zeitschrift für Physik **161**(4): 454-474.

Junginger, F., et al. (2007). "Spin torque and heating effects in current-induced domain wall motion probed by transmission electron microscopy." Applied physics letters **90**(13): 132506.

Leith, E. N. and J. Upatnieks (1962). "Reconstructed wavefronts and communication theory." JOSA **52**(10): 1123-1130.

Lichte, H. and M. Lehmann (2007). "Electron holography—basics and applications." Reports on Progress in Physics **71**(1): 016102.

Maiden, A., et al. (2015). "Quantitative electron phase imaging with high sensitivity and an unlimited field of view." Scientific reports **5**(1): 14690.

Maiden, A. M. and J. M. Rodenburg (2009). "An improved ptychographical phase retrieval algorithm for diffractive imaging." Ultramicroscopy **109**(10): 1256-1262.

McCartney, M. R. and D. J. Smith (2007). "Electron holography: Phase imaging with nanometer resolution." Annu. Rev. Mater. Res. **37**: 729-767.

McDermott, S. and A. Maiden (2018). "Near-field ptychographic microscope for quantitative phase imaging." Optics express **26**(19): 25471-25480.

Merli, P. G., et al. (1976). "On the statistical aspect of electron interference phenomena." Am. J. Phys **44**(3): 306-307.

Midgley, P. (2001). "An introduction to off-axis electron holography." Micron **32**(2): 167-184.

Pelz, P. M., et al. (2017). "Low-dose cryo electron ptychography via non-convex Bayesian optimization." Scientific reports **7**(1): 9883.

Pennycook, T. J., et al. (2015). "Efficient phase contrast imaging in STEM using a pixelated detector. Part 1: Experimental demonstration at atomic resolution." Ultramicroscopy **151**: 160-167.

Putkunz, C. T., et al. (2012). "Atom-scale ptychographic electron diffractive imaging of boron nitride cones." Physical review letters **108**(7): 073901.

Rodenburg, J., et al. (2007). "Transmission microscopy without lenses for objects of unlimited size." Ultramicroscopy **107**(2-3): 227-231.

Rodenburg, J. M. and H. M. Faulkner (2004). "A phase retrieval algorithm for shifting illumination." Applied physics letters **85**(20): 4795-4797.

Rodenburg, J. M., et al. (2007). "Hard-x-ray lensless imaging of extended objects." Physical review letters **98**(3): 034801.

Sanchez, A. and M. Ochando (1985). "Calculation of the mean inner potential." Journal of Physics C: Solid State Physics **18**(1): 33.

Saxton, W. O., & Baumeister, W. (1982). The correlation averaging of a regularly arranged bacterial cell envelope protein. Journal of microscopy, 127(2), 127-138.

Song, J., et al. (2019). "Atomic resolution defocused electron ptychography at low dose with a fast, direct electron detector." Scientific reports **9**(1): 3919.

Stockmar, M., et al. (2013). "Near-field ptychography: phase retrieval for inline holography using a structured illumination." Scientific reports **3**(1): 1927.

Stockmar, M., et al. (2015). "X-ray nanotomography using near-field ptychography." Optics express **23**(10): 12720-12731.

Stockmar, M., et al. (2015). "X-ray near-field ptychography for optically thick specimens." Physical Review Applied **3**(1): 014005.

Sun, H., et al. (2018). "Chemically specific termination control of oxide interfaces via layer-by-layer mean inner potential engineering." Nature communications **9**(1): 2965.

Thibault, P., et al. (2008). "High-resolution scanning x-ray diffraction microscopy." Science **321**(5887): 379-382.

Tonomura, A., et al. (1989). "Demonstration of single-electron buildup of an interference pattern." American Journal of Physics **57**(2): 117-120.

van Benthem, K., et al. (2006). "Three-dimensional ADF imaging of individual atoms by through-focal series scanning transmission electron microscopy." Ultramicroscopy **106**(11-12): 1062-1068.

Van Heel, M., Keegstra, W., Schutter, W., & Van Bruggen, E. J. F. (1982). Arthropod hemocyanin structures studied by image analysis. Life Chem. Rep. Suppl, 1(69-73), 5.

Wen, Z., et al. (2012). "Alternating direction methods for classical and ptychographic phase retrieval." Inverse Problems **28**(11): 115010.

Yang, H., et al. (2016). "Enhanced phase contrast transfer using ptychography combined with a pre-specimen phase plate in a scanning transmission electron microscope." Ultramicroscopy **171**: 117-125.

Yang, H., et al. (2017). "Electron ptychographic phase imaging of light elements in crystalline materials using Wigner distribution deconvolution." Ultramicroscopy **180**: 173-179.

Yang, H., et al. (2016). "Simultaneous atomic-resolution electron ptychography and Z-contrast imaging of light and heavy elements in complex nanostructures." Nature communications **7**(1): 12532.

Zanette, I., et al. (2020). "Phase-Vortex Removal for Quantitative X-Ray Nanotomography with Near-Field Ptychography." Physical Review Applied **14**(6): 064078.

Zhang, H., et al. (2019). "Near-field Fourier ptychography: super-resolution phase retrieval via speckle illumination." Optics express **27**(5): 7498-7512.

Zhang, Y., et al. (2022). "Ptycho-cam: a ptychographic phase imaging add-on for optical microscopy." Applied Optics **61**(10): 2874-2880.

Zhou, L., et al. (2020). "Low-dose phase retrieval of biological specimens using cryo-electron ptychography." Nature communications **11**(1): 2773.